INFORMATION TO USERS

This manuscript has been reproduced from the microfilm master. UMI films the text directly from the original or copy submitted. Thus, some thesis and dissertation copies are in typewriter face, while others may be from any type of computer printer.

The quality of this reproduction is dependent upon the quality of the copy submitted. Broken or indistinct print, colored or poor quality illustrations and photographs, print bleedthrough, substandard margins, and improper alignment can adversely affect reproduction.

In the unlikely event that the author did not send UMI a complete manuscript and there are missing pages, these will be noted. Also, if unauthorized copyright material had to be removed, a note will indicate the deletion.

Oversize materials (e.g., maps, drawings, charts) are reproduced by sectioning the original, beginning at the upper left-hand corner and continuing from left to right in equal sections with small overlaps.

ProQuest Information and Learning
300 North Zeeb Road, Ann Arbor, MI 48106-1346 USA
800-521-0600

Correcting Radar Meteor Observations for the Initial Radius Effect

by

Margaret Diane Campbell
Department of Physics and Astronomy
Graduate Program in Physics

Submitted in partial fulfillment
of the requirements for the degree of
Doctor of Philosophy

Faculty of Graduate Studies
The University of Western Ontario
London, Ontario
June 7, 2002

ABSTRACT

Radar is a useful way to observe the sporadic meteor complex, but it suffers from some biases. The attenuation due to destructive interference within meteor trails of finite width, or initial trail radius effect, is a significant correction factor and is poorly defined. This effect reduces the height to which meteors can be observed with radar and affects observations with higher frequencies more than lower frequencies.

Observations of meteors at three frequencies, 17.45, 29.85 and 38.15 MHz, are used as the basis for a new model of initial trail radius. A model has been constructed which includes fragmentation, the effect of which is more important to the initial radius than the spreading of electrons. The model is shown to explain Geminid observations, and to fit sporadic observations well. The model is used to derive a correction factor for radar meteor fluxes at any wavelength, limiting magnitude and velocity of meteoroid. The correction factor is significantly different from any derived in previous studies. Fluxes of sporadic meteors from five major sporadic sources are calculated for 2000 and 2001 using the new correction factor; significant annual variations are seen in most of the sources indicating differences in the distribution of sporadic radiants around the Earth's orbit.

Keywords: Sporadic meteor flux, initial trail radius, radar observations, meteoroid fragmentation, height ceiling effect, observing biases.

Acknowledgments

My deepest thanks to my supervisor, Dr. J. Jones, for all his guidance and advice. His enthusiasm made it easy to keep working on the project, even when the problem seemed to be getting more and more intractable. I would also like to thank the members of my advisory committee, Dr. J. M. Moorhead and Dr. S. D. Rosner, for their helpful suggestions along the way.

Thanks is due to Dr. Kerry Ellis, for untiring efforts to keep the radar collecting data through storms and equipment failures. Thanks also to Dr. P. Brown, Dr. W. Hocking, Dr. A. Webster, Simona Nikolova, Chris Theijsmeijer and Rob Weryk, for assistance in many ways.

The financial support of the Natural Science and Engineering Research Council and the University of Western Ontario is gratefully acknowledged.

Finally, I would like to thank my family and friends for their support and encouragement. Special thanks to my parents, Catherine and Peter for being there for me through the last four years.

Contents

List of Figures

List of Tables

Chapter 1

Introduction

1.1 Fluxes of Sporadic Meteors

It is important to determine accurately the flux of sporadic meteoroids that strike the Earth. Sporadic meteoroids make up the largest part, in numbers and in mass, of solid particles which strike the Earth every day. Roughly three billion of these meteoroids 10^{-8} kg or larger collide with the Earth each day, approximately one over any square kilometer per hour. Observing the meteors, or ionized and luminous trails of these meteoroids in the atmosphere, is a good way to study actual physical components of our solar system on a daily basis without costly space missions. Determination of the spatial density of these particles is vital for spacecraft and satellite design, where the risks of being hit by a particle must be calculated. Even more fundamentally, knowing the flux of these particles at the Earth can provide both a check and a calibration for a model of meteoroids throughout the solar system. Once the model can successfully reproduce the observed distribution, it can be used with confidence to predict spatial densities of meteoroids throughout the solar system. This will provide information on the formation and evolution of our solar system, and help in the planning of interplanetary missions.

1.2 Sporadic Sources

Determination of the flux, direction and velocity of sporadic meteors has always been much more difficult than for shower meteors. Meteor showers are concentrated over a few days or weeks, come from a well-defined radiant, or direction from which the meteors originate. They have a small range of velocities, so that relatively few observations are needed to characterize flux, radiant and velocity of the stream members. Sporadic meteor radiants are much more diffuse, with a broad spectrum of velocities and relatively low numbers from any given radiant on a day to day basis, so it has historically been much more difficult to define sporadic sources.

The positions of the sporadic sources are usually given in heliocentric ecliptic coordinates. This coordinate system uses two angles: the angle in the plane of the ecliptic between a given azimuth and the sun, and the elevation of the point above the ecliptic plane. The helion point is the sunward direction; the antihelion point is the direction opposite the sun. The apex of the Earth's way is in the plane of the ecliptic, at 90 degrees from the helion point, and the antapex is opposite to the apex direction. The apex crosses the meridian at 0600 local time, the antapex at 1800. The right ascensions and declinations of the sporadic sources are therefore not constant through the year, but change both because of the Earth's motion around the sun and the inclination of the Earth's axis with respect to the ecliptic.

There are six diffuse sporadic sources: the helion and antihelion sources are approximately 20° from the helion and antihelion points, slightly toward the apex point, in the ecliptic plane (Figure 1.1). The north and south apex sources are in the apex direction, roughly 15° above and below the ecliptic. The north and south toroidal sources are also at the longitude of the apex, 60° above and below the ecliptic plane.

1.2.1 Historical observations of the sporadic complex

Initial studies of meteor rates indicated that rates were higher in the latter half of the year compared to the first half in the Northern Hemisphere (Olivier, 1925; Denning, 1886). Since the apex source is higher during the fall and lower during the

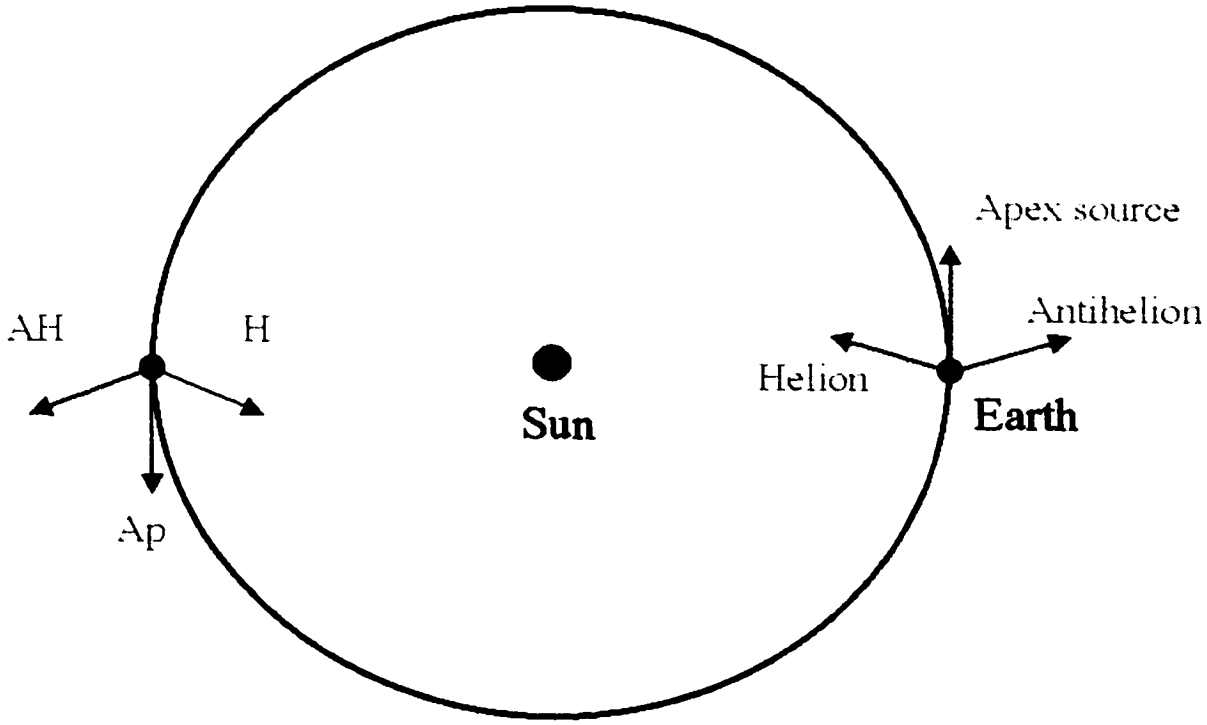

Figure 1.1: Directions of the major sporadic sources

spring for observers in the Northern Hemisphere, this indicated that more meteors came from the apex direction than the antapex. Variation over the course of a night also showed an increase in numbers when the apex source is high in the sky, and a minimum when it is below the horizon. Hoffmeister (1929) used the daily variation of meteor rates to calculate meteoric velocity, and found that a uniform distribution of radiants could not explain the observed rates if all meteors have parabolic or elliptical orbits. One had either to give up the random distribution of radiants, or to allow meteors to have hyperbolic velocities; in other words, to allow a significant fraction of interstellar meteors. Hoffmeister determined that of order seventy percent of meteors should be interstellar. Velocity measurements, however, failed to detect significant numbers of hyperbolic meteors. The work of Hawkins & Prentice (1957) who collected two-station visual data to determine radiants, showed that there is a peak in the antihelion direction, in the plane of the ecliptic, which is stronger than the apex peak. These observations demonstrated that meteor radiants were not uniformly distributed (Lovell, 1954). No increase in meteor radiants was noticed in the direction of the motion of the solar apex through the galaxy, which was also taken as evidence by some (Olivier, 1925) that meteoroids are not interstellar.

The first extensive radiant survey, done with the Jodrell Bank radar, showed that meteor radiants are concentrated in the plane of the ecliptic, meaning that they are part of the solar system (Hawkins, 1956a). While there is a concentration of radiants in the apex direction, the largest concentrations are 60 to 70 degrees from the apex, close to helion and antihelion points. The equipment used had two receiving antennas with long, narrow beams oriented roughly 50 degrees apart: from the rates recorded on each receiver the position of a source could be approximately calculated.

A similar survey in the Southern Hemisphere by Weiss & Smith (1960) found the same concentration of radiants in the ecliptic, and they proposed that there are two distinct populations of sporadic meteors. One is composed of a random distribution of radiants, and therefore is observed to come from the apex direction because of the relative motion of the Earth; the other forms the helion and antihelion sources.

Elford & Hawkins (1964) first identified a source 60 degrees north of the apex,

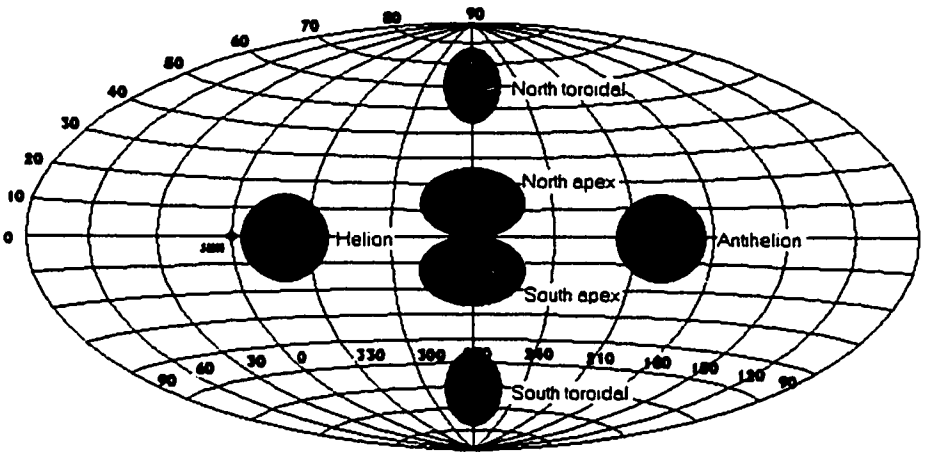

Figure 1.2: Six source sporadic model, in heliocentric ecliptic coordinates

using data from the Harvard Meteor Radar. Sekanina (1976) examined the radiants of radar meteors in heliocentric coordinates. Plotting these radiants showed that the apex source could be resolved into a northern and southern component, with an additional concentration of radiants 60 degrees above the apex. This is the north toroidal source, so named because the orbits apparently form a toroid about the sun. Jones & Brown (1993) showed from an extensive survey of radar and photographic data from both hemispheres that the apex source is split into a northern and southern component, placed roughly 20 degrees above and below the ecliptic. They also demonstrated the existence of the south toroidal source, the counterpart of the north toroidal, placed 60 degrees below the ecliptic (Figure 1.2).

1.2.2 Strengths of the sporadic sources

Of these six sporadic sources, the helion and antihelion are the strongest by a significant margin (Keay, 1963; Brown & Jones, 1995). The apex sources tend to show up strongly because of the higher average velocity of the meteoroids, which produces greater luminosity and ionization, but have about 25% of the strength. The north and south toroidal sources are the weakest.

Another issue of interest for sporadic meteors is the change in flux of each source over the course of a year, corresponding to different radiant densities around the

Earth's orbit. Hawkins (1956b) found a higher total flux of meteors in the summer months, but did not correct extensively for observational selection effects and used only Northern Hemisphere data. Štohl (1967) studied the change in flux of the helion, antihelion and apex sources over the course of a year, and found that the apex source has significant variation at the same time in the Northern and Southern Hemispheres. The toroidal source was found to be the weakest and to have a slight maximum in the first part of the year. The helion and antihelion sources show a significant difference between the northern and southern profiles, indicating that the elevation of the sources is more significant than azimuthal asymmetries in orbital distribution. Keay (1963) found a significant change in total rates through the year, even when observing effects had been accounted for. The change in rates through the year is not large, however; Jones *et al* (1994) found from forward scatter radar data that observations could be fit assuming constant source strengths. Poole (1997) studied the change in source strength of the helion and antihelion sources over a total of 10 years using radar observations, correcting for observing geometry. He found that the helion source peaks in April and May, while the antihelion source peaks in the middle of the year (Figure 1.3).

1.3 Radar Observations

Radar is a convenient way to study the sporadic background. A radar system can detect meteors day and night regardless of cloud conditions. It is also well suited to automated data collection and analysis, necessary if the tens of thousands of sporadic meteors needed to define sources are to be efficiently recorded. The main difficulty is the observational biases of the radar, which must be removed from the data before meaningful fluxes can be calculated.

To find a flux, both a corrected rate of detection and a collecting area must be known. The collecting area of a radar system is a fairly straightforward calculation, and measures the physical area of sky over which meteoroids can be detected. Underdense meteors only produce an echo if they are perpendicular to the radar beam.

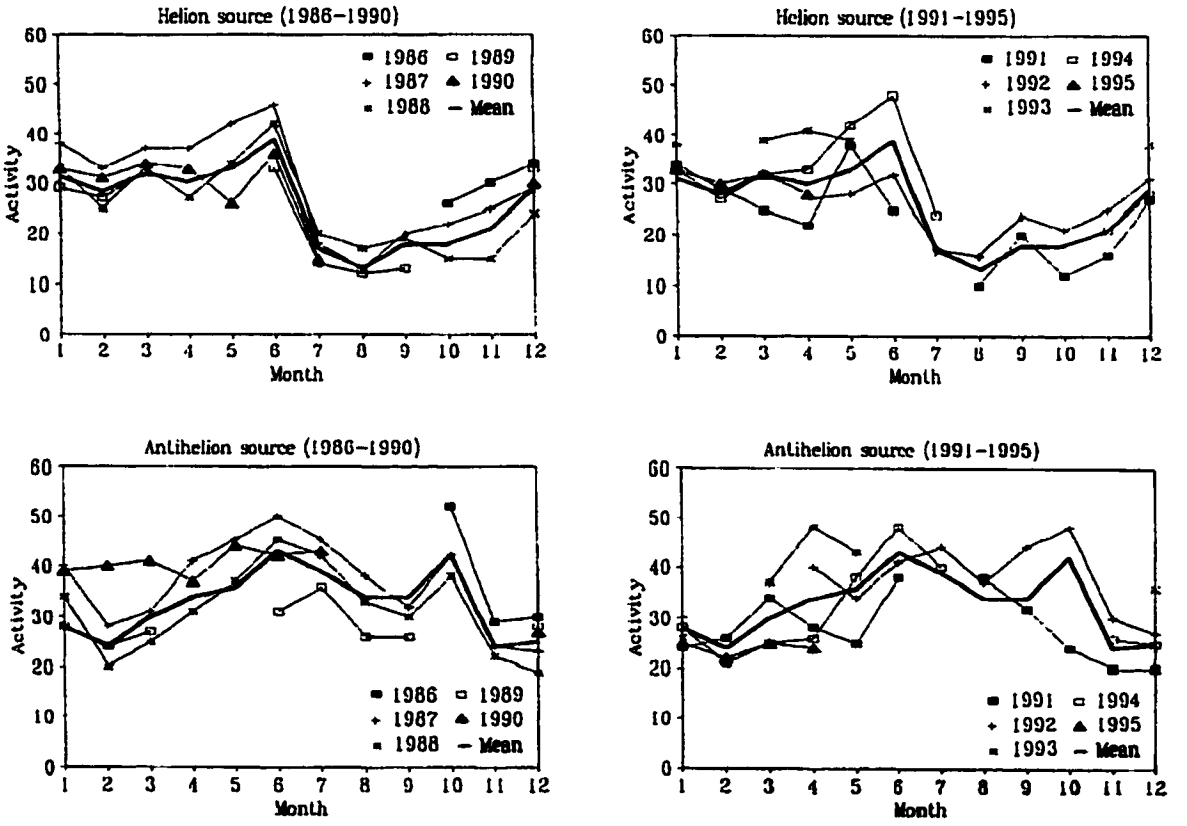

Figure 1.3: Annual variations of the rate of sporadic meteors (helion and antihelion sources) Month 1 = January, Month 12 = December. Units are relative activity, corrected for source elevation. (Poole (1997), observations made in South Africa)

For a particular radiant, echoes will be received from a plane perpendicular to the radiant direction. The echo region would be an infinitely thin line if all meteor echoes occurred at the same height; in reality the echoes are spread over a range of heights. The meteors from a given radiant therefore occur on an echo surface, the area of which can be calculated from a known meteor height distribution by integrating over the part of the plane above the horizon. This is combined with the gain pattern of the transmitting and receiving antennas of the system, which determine how well a given location in the sky can be observed, to obtain a weighted collecting area.

In order to determine the rate of meteors from a particular source, it is necessary to be able to identify which radiant is associated with each meteor. If this cannot be done directly using observations at multiple stations (as is the case with most radars), a statistical measure must be obtained for each radiant (see Chapter 7 for details of this procedure). A correction factor is then applied to this rate.

The correction factor is not well defined. It includes a correction for the size of the Fresnel zone, which depends on the wavelength of the system, on the transmitter power, the gain of the antennas, and on several observing effects, including the initial radius effect, the finite velocity effect, and Faraday rotation (see Chapter 2 and Chapter 5).

The initial radius effect, or attenuation of echoes from trails with significant width, is the least well understood of the correction factors. The fact that meteors detected by radar have a significantly different height distribution from optical meteors has long been known, as has the fact that the radar height distribution depends on the radar frequency. The fact that radar meteors are found in lower numbers than expected from dust and optical measurements was originally (Hughes, 1978) attributed to a large population of low velocity meteors which did not produce enough ionization to be observed by radar reflection. The major reason for the small numbers is actually the height ceiling effect, which affects all radars, but in particular those with frequencies above 10 MHz. This initial radius effect imposes a limit, or ceiling, on the height of meteors that can be detected with radar systems: the height limit is lower for observations at higher frequencies. Many studies have been done showing the variation

in meteor rates with radar frequency (Thomas *et al*, 1986; Olsson-Steel & Elford, 1986, 1987; Elford & Steel, 1988; Steel & Elford, 1991). In particular, observations at 2 MHz and 6 MHz have shown that the peak in meteor ionization heights is much higher than that observed with conventional meteor radars. Unfortunately, observing at low frequencies where the height ceiling is high enough to capture most meteors is not practical due to interference and ionospheric effects at frequencies lower than ~20 MHz.

1.4 The Initial Radius Effect

1.4.1 Reflection of radar signal from a meteor trail

A meteor echo is received when a meteor trail forms perpendicular to the radar beam. Most of the reflected intensity comes from the first Fresnel zone, a segment of trail roughly a kilometer long (see Chapter 2). The amplitude of the echo rises during the fraction of a second needed for the meteor to cross this region. Even at this time, the column of ionization already has a significant width, of order of meters at an altitude of 100 km. As the meteor ablates, both melting and vaporizing, electrons and ions thrown off from it collide with atmospheric atoms until they reach the thermal velocity of the surrounding gas. This will take only a fraction of a second, so the signal received is from this distribution of electrons. The trail then diffuses outward, causing the underdense echo to decay.

An underdense meteor trail is one where the ionized trail is less than critically dense at the frequency of observation. One therefore receives reflections from electrons throughout the underdense trail: each one scatters radiation independently and coherently. Since the radiation from the near and far parts of the trail will have a phase difference upon reaching the receiver, destructive interference will occur if the trail is of order $\lambda/2$ in width. This will not happen in overdense echoes, which have an electron density greater than the critical plasma density; in other words, these trails are radiatively thick. In this case, reflection happens essentially entirely at the

surface of the column, and the amplitude of the echo is not reduced for larger trail radii. A transition echo has an intermediate density, and will have characteristics of both types of echo.

The initial radius of a trail will increase with height, since the atmospheric density, and therefore resistance to the expansion of the trail, decreases exponentially with increasing height. This fact is responsible for the observed wavelength-dependent echo height ceiling effect: at any frequency there is a height above which few underdense echoes can be seen, because the attenuation due to destructive interference from the large radii of the trails is too great. This ceiling is lower for shorter wavelengths, as one would expect. The attenuation of the return pulse will also be affected by how much the trail expands in the time the meteoroid takes to cross the first Fresnel zone (see Chapter 2), and on the actual density profile of the electrons in the trail.

Essentially there are four functions involved in the simplest case of initial radius attenuation. The radial dependence of the electron density of the trail is related to the attenuation of received power with wavelength and initial radius. The variation of attenuated amplitude with height is connected to the third function, the change in initial radius of the trail with height. The attenuated amplitude of the echo power with wavelength and initial radius is found from the Fourier-Bessel transform of the radial electron density function, a cylindrical integral of the radiation scattered by each electron in the trail. A Gaussian electron density function produces a Gaussian decrease in signal strength with increasing initial radius. If one of either the radial electron density or attenuation with wavelength and initial radius are known, it is a relatively straightforward matter to find the other. The attenuated amplitude as a function of height is easily obtained from the variation of initial radius with height and the attenuation with initial radius. These basic functions can be complicated by fragmentation of the meteoroid, by dependence of the initial radius on the velocity of the meteoroid, and by structural differences between meteoroids, for example meteoroids with different parent objects. The radial electron density function may vary from meteor to meteor or along a meteor's trail.

Since the initial radius can be assumed to depend on the mean free path (and

therefore inversely on atmospheric density), the initial radius can be written as

$$r_i \propto \ell^n \tag{1.1}$$

where ℓ is the mean free path (or equivalently $r_i \propto \rho^{-n}$). One can similarly define the exponent b as

$$r_i \propto V^b \tag{1.2}$$

where V is the meteoroid's speed.

1.4.2 Observations of initial radius

Hawkins & Whipple (1958) and Cook *et al* (1962) attempted to calculate the initial radius of meteor trails from photographic records of meteors, by comparing the width of the meteor trails on film with those of stars. Both used data from the Schmidt camera at Mount Palomar, and accounted for focal corrections, atmospheric effects, photographic diffusion and camera aberration. Hawkins and Whipple found that all the trails had diameters less than 4 meters, and most were around 1 meter. Since no precise heights were measured, no height dependence could be found. Cook *et al* (1962) also found most trails to be of order 1 meter, with the possibility of widths up to 6 meters. Hawkins and Whipple found the average radius to be 0.79 m at an average height of 104 km for Perseids and Orionids, and 1.20 m at 94 km for several other showers. Cook *et al* (1962) found r_i =0.97 m at 100 km for Geminids for their whole sample (Hawkins, 1963). To apply these results to radar data, one must also assume that the luminous trail and ionized trails coincide spatially: in principle the ions and excited atoms will have different mean free paths. The neutral part of the trail could extend past the ionized part, so optical observations provide an upper limit to initial radii of the ion trails. More recently, higher resolution video studies of meteor trains have given much larger initial radii (Hawkes, 2002), of order 10 meters.

Initial radius can also be calculated using radar observations. By observing echoes at different frequencies and comparing them, amplitude and number ratios can be cal-

culated. In these multifrequency studies, the amplitude or number ratios can be used to determine the attenuation. The ratio of the amplitudes of an echo as seen on two different radars at a particular height should be nearly the same as the ratio of the numbers of echoes seen by the radars at that height. If the radial distribution of electrons in the trail is known (allowing the attenuated amplitude as a function of initial radius and wavelength to be calculated) then the initial radius can be calculated for each observed height. To do this, the radar transmitter powers and receiver sensitivity must be very well calibrated, at least relative to one another, and heights and amplitudes must be measured precisely. Ideally, the radars should be identical apart from their frequencies and operate simultaneously. Velocity dependence is difficult to calculate from most radar data: some meteors show Fresnel oscillations and the velocity can be calculated from these, but many do not.

The first radar studies of initial radius were done by Greenhow & Hall (1960). They observed echoes at radar wavelengths of 17 m (17 MHz) and 8.3 m (36 MHz) with similar radar systems, using overdense echoes (which are not affected by initial radius attenuation) to calibrate the sensitivities. Decay times were used to estimate heights, and the electron density profile was assumed to be Gaussian. The amplitudes of simultaneous echoes on the two systems were compared, and the ratios used to calculate initial radius. Another data set taken at 4.3 m (70 MHz), which was not coincident with the other two wavelengths, was used to obtain a relation between wavelength and attenuated amplitude in numbers. They found that the exponent n of mean free path dependence (equation 1.1) was 0.35, much less than expected. The initial radius at 90 km was 1 meter. They also found no significant dependence of initial radius on velocity, as calculated using Fresnel oscillations; fitting the standard velocity equation gives b=0 (equation 1.2). Since most meteoroids fragment, and a fragmenting meteoroid will tend to have no Fresnel oscillations, less than ten percent of echoes can be used for this type of velocity calculation. There may be a systematic bias in the results due to the exclusion of fragmenting meteoroids. They also used overdense echoes to estimate initial radius and found a value exceeding 1.8 m.

Kashcheyev & Lebedinets (1963) used two frequencies (75 MHz and 37.5 MHz).

They were not able to find a meaningful dependence of initial radius with height because of the limited useful height range of the higher frequency system, but found an average initial radius of 80 cm at heights around 92 km. They also used Fresnel oscillations to calculate meteor velocities, and found a significant variation of initial radius with velocity, with b=0.4. The authors suggested that the inclusion of a large number of transition echoes in Greenhow and Hall's study might have been responsible for the disagreement in the velocity exponents.

Using frequencies of 31.26 MHz and 46.2 MHz, Bayrachenko (1963) obtained n=0.82. Diffusion coefficients were used to determine the heights of meteors, and the average initial radius around 97 km was of order 1 meter. A velocity relation was derived using 34 meteors, velocities calculated using Fresnel oscillations, and gave b=0.33.

Baggaley (1970) used radar observations at 10 MHz and 28 MHz, calibrated with overdense echoes, to calculate initial radius. He took into account magnetic field effects, and used decay times to obtain heights. Velocities were measured using the rate at which the amplitude increases to maximum, the rise-time method. He found a velocity exponent of b=0.57$\pm$0.16, and a dependence on mean free path of n=0.45$\pm$0.03, with r_i=1.06 m at 100 km.

Overdense echoes can also be used to investigate initial radius. An overdense echo normally has an electron line density along the trail in excess of 10^{14} electrons per meter; however, if the initial radius is large the density of the trail can be reduced to the point where the echo behaves as a transition or underdense echo. By observing the same echo on different frequencies, one can find limits on the initial radius of meteors at those heights. This method was proposed by Delov (1976) and used by Baggaley & Fisher (1980), who used multi-frequency observations of both under and overdense echoes, and found n= 0.63. Baggaley (1980) also investigated the relation between velocity and initial radius, using sporadic meteors and Geminids. With no directional information, he separated the echoes into bins of high Geminid activity and little or no Geminid activity, and compared the initial radius for the Geminid set (with V=35 km/s) with the sporadic set (the sporadic velocity was assumed to be 50

km/s). He found b=1±0.3 and n=0.42±0.07.

Moysya (1969) investigated the relationship between initial radius and velocity, using the data of Kashcheyev and Lebedinets. He constructed two models, one with a strong velocity dependence and one with no velocity dependence, and found that the one with the strong velocity dependence matched the data better.

1.4.3 Modelling trail formation

Manning (1958) was the first to model initial radius on a theoretical basis, using collisional cross sections worked out by Massey & Sida (1955). Manning found that the initial radius should be 14 cm at 93 kilometers altitude and should have n=1 and b=0.09. He also found that the distribution of electrons in the trail should be Gaussian. Dokuchaev (1960) also found that the distribution of electrons should be Gaussian, provided the trail was below 100 km. Grusha (1991) modeled the formation of a meteor trail including random variations in atmospheric density and fragmentation of the meteor itself. Grusha assumed that the density of fragments of the meteor has a Gaussian dependence, and that the radius of the fragmented group of particles decreases exponentially with height. He used n=1, b=0.65 for individual fragments, but obtained an initial radius which reached a minimum at approximately 90 km, increasing rapidly as height is increased and slowly as height is decreased. When the functions were fit to the theoretical data, n=0.13 and b=0.12 were obtained.

Jones (1995) treated all atoms as hard spheres undergoing elastic collisions, and used a Monte Carlo simulation technique to find a theoretical initial distribution. He used the scattering cross-sections of Bronshten (1983) (after Portnyagin and Tokhtas'yev (1974)), which are proportional to $V^{-0.8}$, and obtained an initial radius which goes exactly as mean free path. The radial distribution of electrons generated by this model is not Gaussian: it more closely resembles an exponential.

Since the experimental studies show a much smaller dependence of initial radius on height than expected with conventional theory (Table 1.1, Figure 1.4), Hawkes & Jones (1978) proposed a modified model, which included fragmentation of spinning

Table 1.1: Summary of results of previous studies of initial radius dependence with height ($r_i \propto \ell^n$) and velocity ($r_i \propto V^b$)

Study	n	b
Greenhow and Hall (1960)	0.35	0
Kashcheyev and Lebedinets (1963)	-	0.4
Bayrachenko (1965)	0.82	0.33
Baggaley (1970)	0.45±0.03	0.57±0.16
Baggaley (1980)	0.42±0.07	1±0.3
Baggaley and Fisher (1980)	0.63±10%	-
Baggaley (1981)	0.26	-
Manning (1958) (model)	1	0.09
Grusha (1991) (model)	0.13	0.12
Jones (1995) (model)	1	0.8

bodies to explain this. As a meteoroid fragments, the pieces would be thrown off at the rotational velocity of the surface and give the meteor a larger initial radius than it would otherwise have.

In the dustball model, meteoroids are composed of a large number of small, solid grains, held together with some sort of low boiling point "glue" (Hawkes & Jones, 1975). When the particle enters the atmosphere, the volatile component boils away without producing any light, releasing the component grains. These grains eventually heat and ablate, producing the light and ionization. This model explains the short duration and odd profiles of light curves of faint meteors (Campbell *et al*, 2000), which cannot be explained by the classical single-body theory which assumes a single, solid, uniform object. Most small meteors also appear to have fragmented prior to the onset of luminous ablation, since continuing fragmentation would produce flares and flares are only seen on brighter meteors. Larger meteors will not heat uniformly, so the volatile component may remain unevaporated in the core until the meteoroid has begun to ablate.

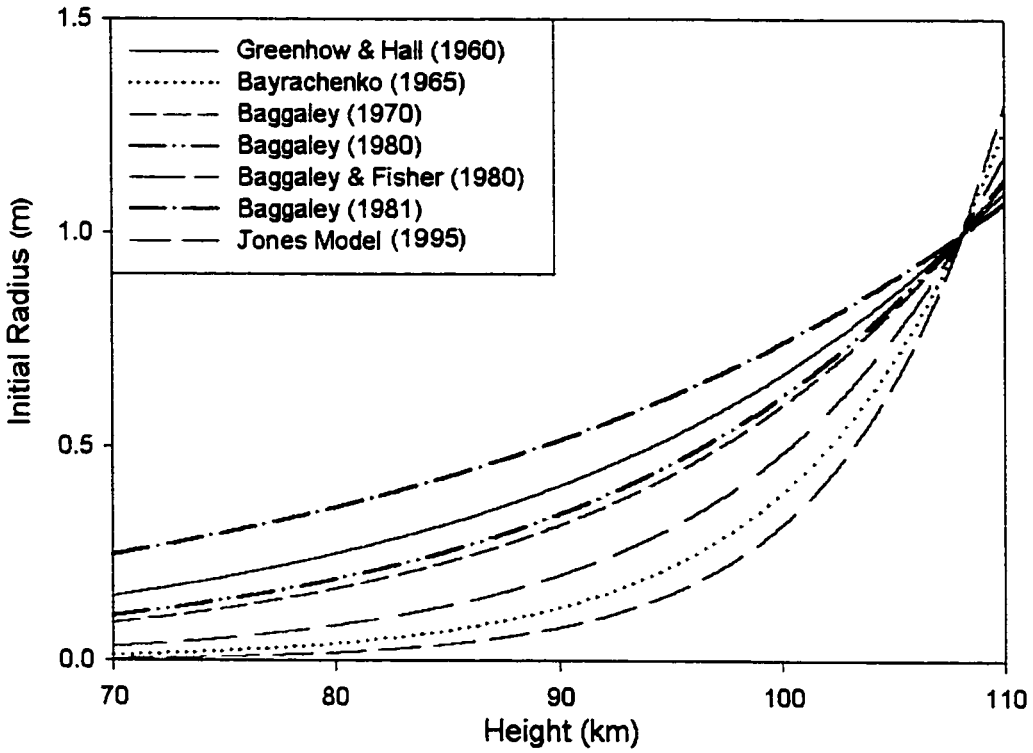

Figure 1.4: Initial radius as a function of height, assuming $r_0 = \ell^n$

If the meteor has fragmented or is fragmenting, the trail of electrons that it produces will not be a simple shape determined only by the ablation process. The echo power will be the sum of the returns off the trails left by each fragment. There are limits on the lag between fragments (Fisher *et al*, 2000; McCrosky, 1958), which set limits on the radial width of the group of fragments. Most meteors do not show lags of more than 200 m. The radial separation will be much smaller than this, since lag along the trail is caused mainly by deceleration of the smaller fragments.

All experimental studies have assumed the distribution of electrons in the trail to be Gaussian. However, this is not the predicted distribution in all models of meteoroid ablation, and certainly need not be the case for fragmenting meteoroids. Because of this, measures of initial radius will be uncertain.

Complications in the calculation of initial radius may also arise if the electron density profile is different for different meteors. For example, a very fragile dustball meteor may have separated into constituent grains long before it begins to ablate,

while a denser meteoroid will take longer to fragment, and may still be fragmenting while it ablates. To look for these sorts of differences, it would be useful to study shower meteors whose properties have been determined to see if they have different dependencies of initial radius on height. There may be magnetic field effects in the expansion of the trail, as investigated by Oppenheim *et al* (2000). Finally, the electron density profile could change with height.

1.4.4 Correcting radar amplitudes and rates

The correction factor of radar amplitude for initial radius, assuming the radial electron density in a meteor trail is Gaussian, is

$$\frac{A}{A_0} = \exp\left(\frac{-4\pi^2 r_0^2}{\lambda^2}\right). \tag{1.3}$$

Assuming the number seen is proportional to the amplitude, and given a reasonable height distribution, we can find the percent of echoes seen at any wavelength.

There are significant differences in initial radius as a function of height as determined from all experimental and theoretical studies of the problem (Figure 1.4). In particular, there is no agreement on the dependence of initial radius on mean free path and on velocity (Table 1.1). The percentage of echoes seen by a radar operating at a particular frequency varies by at least factor of four from one model to another (Figure 1.5). To calculate accurate fluxes, it is necessary to determine which if any of these is correct.

1.5 Statement of Problem

Determining the sporadic meteor flux is important not only for astronomical reasons, but also to evaluate the risk to spacecraft. Radar observations are useful for monitoring the sporadic background, but they suffer from a number of limitations.

The initial radius attenuation produces a large uncertainty in flux measurements. Previous measures of the correction factor vary widely from study to study, and as a

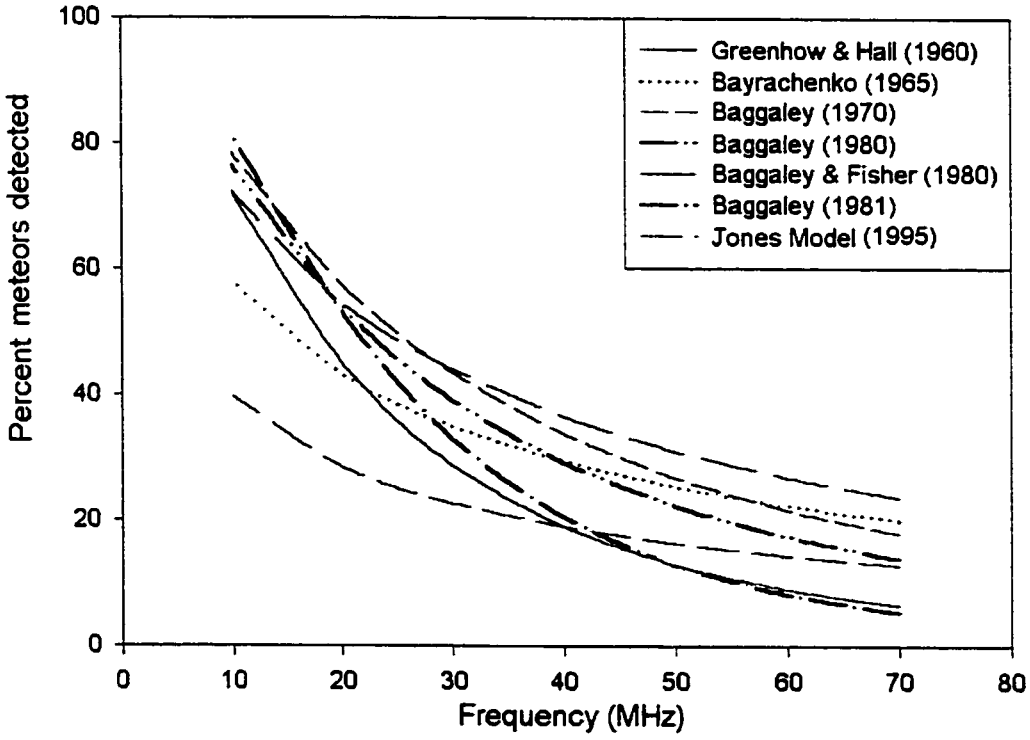

Figure 1.5: Percentage of meteors detected as a function of wavelength for results of different initial radius surveys

result the absolute flux from radar measurements is uncertain by up to a factor of ten. The present study undertakes to determine the correction factor for any frequency, and to use this correction factor to obtain fluxes.

To accomplish this, we will use data from a three frequency radar system. Amplitude ratios between pairs of frequencies at different heights will be determined. A model of initial radius will be constructed which explains the observations. The model will then be used to find the total number of meteors observed at any frequency.

The most important aspect of the model to be developed is the addition of the effects of fragmentation of meteoroids on the attenuation of meteor echoes. The initial radius caused by fragmentation was found to be more important than the size or shape of the trails of individual fragments, so the correction factor depends most strongly on the way the meteoroids fragment. By determining this, some information can be determined about the internal structure of meteoroids.

Chapter 2

Theory

2.1 Attenuation Due to the Initial Trail Radius

To obtain a reliable estimate of the meteor flux from radar observations, we need to know the attenuation of each echo as a function of wavelength and height. This attenuation of radar returns due to initial radius can be calculated, but it requires that the details of the reflection process and the structure of the trail be known. These can be examined both with modelling based on theory, and optical observations. The distribution of electrons in the trail of an individual object must be known, and provision made for the possibility of fragmentation.

2.2 Reflection of Radio Waves from an Infinitely Thin Trail

In monostatic backscatter radar observations, the transmitter and receiver are located in the same place. Backscatter observations are well suited to monitoring sporadic sources, since the geometry is relatively simple and the echo directions can be measured easily: the geometry is more complex in the forward scatter case when the transmitter and receiver are located up to 2000 kilometers apart. However, backscatter observations must be corrected for initial radius effects. Forward scatter systems

are not affected by the initial radius of the trail, since the difference in path length of waves scattered from points through the trail's width are small compared to the wavelengths used. In the backscatter case the difference in path length is of order the size of the trail, so initial radius has a significant effect.

Radar echoes occur because of the scattering of radio waves by individual electrons in the plasma of the meteor trail. Two broad categories of echo can be distinguished: underdense and overdense. In the underdense case, the trail is thin so that there is little secondary scattering of radio waves: the trail is transparent to the radar beam and all electrons around the reflection point contribute to the total returned power. In the overdense case, the electrons have a density that is sufficiently high to prevent radio waves from penetrating into the trail: the echo consists essentially of reflections from the outermost electrons only. Only underdense echoes are affected by attenuation due to initial radius.

Meteor trails diffuse outward rapidly because of the low atmospheric density, and therefore long mean free paths between collisions, at meteor heights. Underdense echoes decay in an exponential fashion as their radius increases; they can no longer be detected when their radius becomes of order the wavelength of observation. Overdense trails persist much longer than underdense trails, since they cease to be visible only when the density at the trail axis drops sufficiently and the echo becomes underdense. They are quickly twisted by atmospheric winds: reflection can then occur from any part of the trail with an axis perpendicular to the radar direction, and the amplitude profile of these echoes tends to be irregular. Underdense echoes can only be detected when the axis of the forming trail is perpendicular to the line of sight of the radar. This specular, or mirror-like, reflection means that echoes from a given radiant lie on a plane perpendicular to the radiant direction. Likewise, if the echo direction but not the radiant is known, the radiant point must lie on a plane perpendicular to the echo direction (Figure 2.1).

Most of the echoes considered in this study are underdense. The reflection process is a problem in diffractive optics, since the wavelengths involved are so long. The reflected echo comes mainly from the specular point, the point on the trail closest to

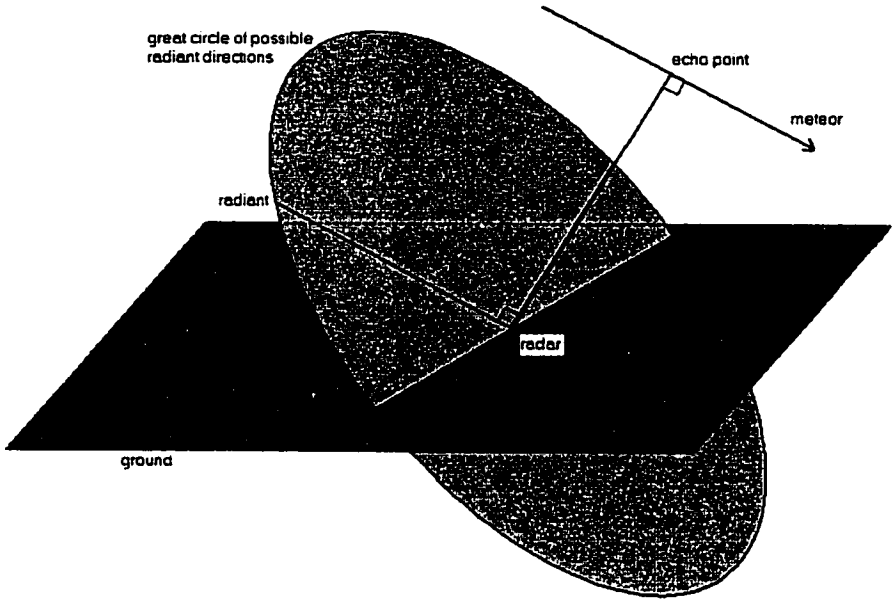

Figure 2.1: Reflection of radar beam from specular meteor trail

the radar, which has a range R_0. As one moves along the trail away from this point, the phase of the return will change as the distance to the source increases, with the phase angle of the form

$$\phi = \frac{4\pi d}{\lambda} \tag{2.1}$$

where d is the extra distance from the reflection point to the receiver; the radar pulse travels twice this distance. When the distance to the source reaches $R_0 + \lambda/4$ the phase difference will be π and there will be destructive interference. The length of the region between these two points is

$$L_F = 2\left(\left(R_0 + \frac{\lambda}{4}\right)^2 - R_0^2\right)^{1/2} \tag{2.2}$$

or

$$L_F = 2\left(\frac{R_0\lambda}{2} + \frac{\lambda^2}{16}\right)^{1/2}. \tag{2.3}$$

λ is much smaller than R_0, so the length of the first Fresnel zone is approximately

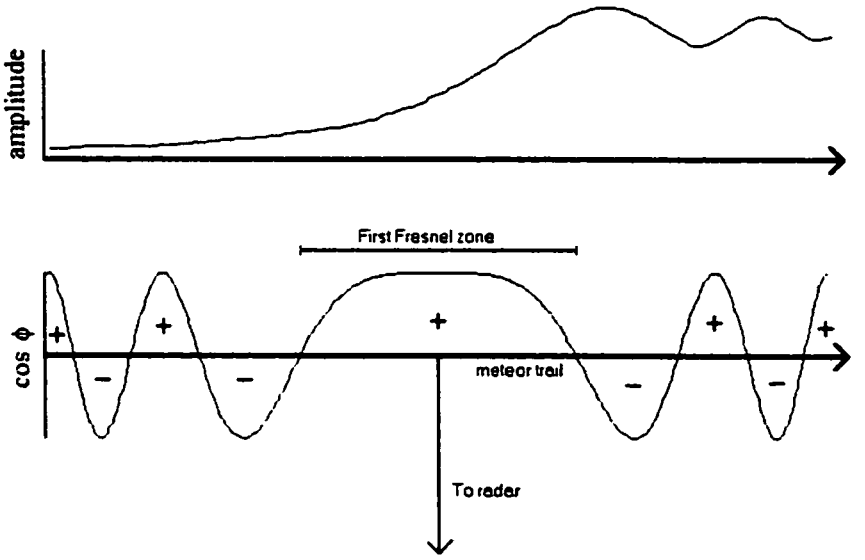

Figure 2.2: Fresnel zones in radio wave reflection from a meteor

$$L_F = (2R_0\lambda)^{1/2} \tag{2.4}$$

which is of order one kilometer for a typical range of 150 km and a wavelength of 10 m. The region inside these points is called the first Fresnel zone, and most of the scattered radiation comes from within this region. The other, progressively smaller Fresnel zones will make diminishing contributions to the total amplitude (Figure 2.2). The amplitude will reach a maximum just after the meteor passes through the first Fresnel zone.

The simplest calculation of power returned from a meteor assumes that the trail is an infinitely thin line (e.g. McKinley (1961)). One can therefore sum the contributions from each electron in the trail to find the total reflected power. The contribution of a single electron can be found by multiplying the transmitted power per unit area by the scattering area of one electron and the effective area of the receiving antenna. The transmitted power at the location of the meteor trail is $(P_T G_T)/(4\pi R^2)$, where P_T is the transmitter power, G_T is the transmitting antenna gain, and R is the range to a particular point on the trail (Figure 2.3). The gain of the antenna is a measure of how the antenna's radiation pattern differs from an isotropic radiator. The power per

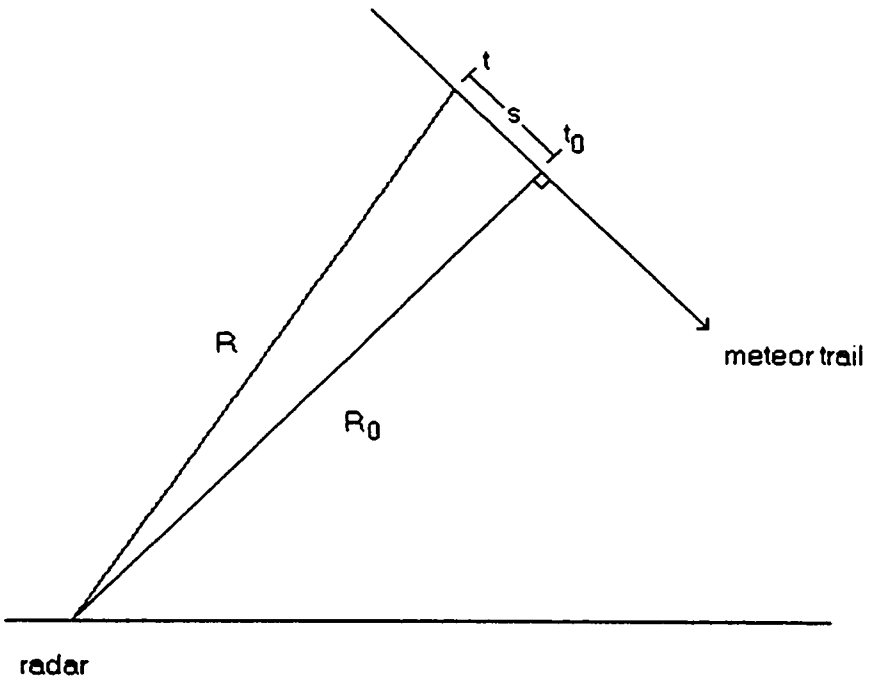

Figure 2.3: Geometry of meteor path relative to radar

unit area scattered by one electron measured at the radar will be $\sigma_e/(4\pi R^2)$ times the transmitted power per unit area at the meteor trail, where σ_e is the scattering cross section of the electron. The effective area of the receiving antenna is $(G_R\lambda^2)/4\pi$, where G_R is the receiving antenna gain in the appropriate direction and λ is the wavelength. The total power received from one electron is therefore:

$$\Delta P_R = \frac{P_T G_T G_R \lambda^2 \sigma_e}{64\pi^3 R^4}. \tag{2.5}$$

To find the total received power, the contribution of each electron must be summed taking into account that the phase will be different for electrons at different points on the trail. The total voltage amplitude will change with time as the meteor trail forms; it will rise rapidly as the meteor passes the specular or t_0 point, and oscillate as it passes through each subsequent Fresnel zone (Figure 2.2). We must therefore add the amplitudes of the returns from each electron, keeping track of the phases.

The voltage at the receiver is simply $(2R_i\Delta P_R)^{\frac{1}{2}}$, where R_i is the receiver input

impedance. There are two terms in the phase angle ϕ: $2\pi ft$ is the phase of the radio wave with frequency f at time t, and $-(4\pi R)/\lambda$ is the change after the wave travels a distance R. R changes as the meteor moves along its path. The in-phase amplitude will be $A\cos\phi$, and the quadrature component $A\sin\phi$.

Assuming the meteor trail has an electron line density q, in electrons per meter, we have the amplitude due to a small element of trail:

$$dA_R = (2R_i\Delta P_R)^{\frac{1}{2}}\, q \sin\left(2\pi ft - \frac{4\pi R}{\lambda}\right) ds \tag{2.6}$$

where ds is a small distance interval along the trail at range R (Figure 2.3). If s_1 is the initial position of the meteor, and s the current position, the total radiation at time t will be:

$$A_R = (2R_i\Delta P_R)^{\frac{1}{2}}\, q \int_{s_1}^{s} \sin\left(2\pi ft - \frac{4\pi R}{\lambda}\right) ds \tag{2.7}$$

here we have assumed q to be constant over the region of integration, and removed it from the integral. This integral is not easy to evaluate, but becomes easier if the following substitutions are made, after McKinley (1961). Since s is much smaller than R_0 in the desired interval, we can use $R \simeq R_0 + s^2/2R_0$, from the Pythagorean theorem and the series expansion of $\left(1 + s^2/{R_0}^2\right)^{\frac{1}{2}}$. We can also use the transformations $\chi = 2\pi ft - (4\pi R_0)/\lambda$ and $2s = x\,(R_0\lambda)^{\frac{1}{2}}$. We then have:

$$A_R = \frac{(2R_i\Delta P_R R_0\lambda)^{\frac{1}{2}}}{2} q \int_{x_1}^{x} \sin\left(\chi - \frac{\pi x^2}{2}\right) dx. \tag{2.8}$$

Expanding the sine function, we have:

$$A_R = \frac{(2R_i\Delta P_R R_0\lambda)^{\frac{1}{2}}}{2} q \int_{x_1}^{x} \left(\sin\chi\cos\frac{\pi x^2}{2} - \cos\chi\sin\frac{\pi x^2}{2}\right) dx. \tag{2.9}$$

Since χ does not vary with s or x, those terms can be removed from the integral. If we then introduce the substitutions:

$$\mathbf{C} = \int_{x_1}^{x} \cos\frac{\pi x^2}{2} dx \tag{2.10}$$

and

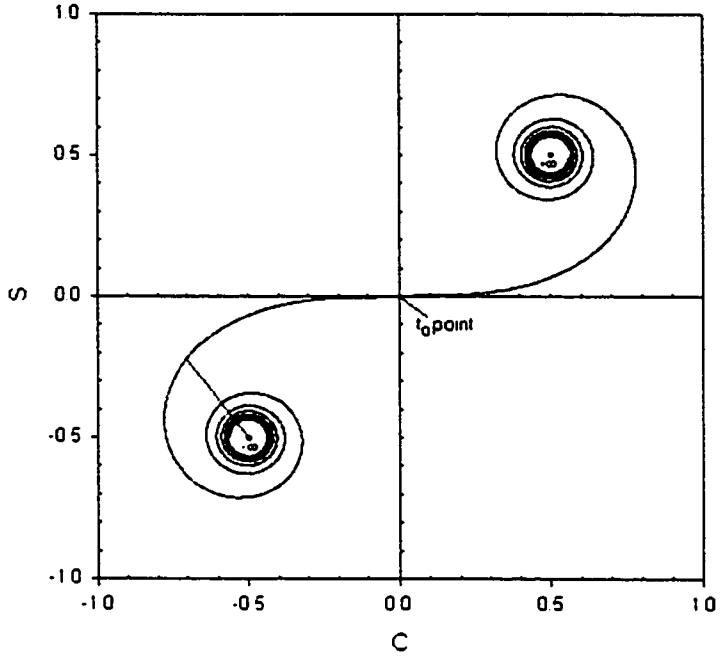

Figure 2.4: Cornu Spiral

$$\mathbf{S} = \int_{x_1}^{x} \sin \frac{\pi x^2}{2} dx \tag{2.11}$$

which are the conventional Fresnel integrals, arising in optical theory, we have:

$$A_R = \frac{(2R_i \Delta P_R R_0 \lambda)^{\frac{1}{2}}}{2} q \left(\mathbf{C} \sin \chi - \mathbf{S} \cos \chi\right). \tag{2.12}$$

This will be the quadrature amplitude. The echo amplitude increases rapidly through the t_0 point, then oscillates while it decays. The amplitude can be determined graphically by plotting $\mathbf{S}$ against $\mathbf{C}$ (Figure 2.4). The meteor begins at $-\infty$. The relative amplitude is the magnitude of a vector joining this point to a point on the curve, and the phase at that point is given by the vector's orientation.

To find the returned power, the amplitude must be squared:

$$P_R = \frac{{A_R}^2}{2R_i} = \frac{\Delta P_R R_0 \lambda}{2} q^2 (\mathbf{C} \sin \chi - \mathbf{S} \cos \chi)^2 \tag{2.13}$$

$$P_R = \frac{\Delta P_R R_0 \lambda}{2} q^2 \left(\mathbf{C}^2 \sin^2 \chi - 2\mathbf{CS} \sin \chi \cos \chi + \mathbf{S}^2 \cos^2 \chi \right). \tag{2.14}$$

Of the two terms in χ, only one varies: $2\pi ft$ varies with time at the frequency of the radar signal. Because the frequency is large, we can take a time average over a short interval. We then have:

$$P_R = \frac{\Delta P_R R_0 \lambda}{2} q^2 \left(\frac{\mathbf{C}^2 + \mathbf{S}^2}{2} \right). \tag{2.15}$$

The term in the bracket, $(\mathbf{C}^2 + \mathbf{S}^2)/2$, is roughly equal to unity when taken over the first few Fresnel zones of the meteor (McKinley, 1961):

$$P_R = 2.5 \times 10^{-32} P_T G_T G_R \left(\frac{\lambda}{R_0} \right)^3 q^2. \tag{2.16}$$

The amplitude of the echo will be

$$A = cV \tag{2.17}$$

where c is some constant determined from the hardware and V is the voltage output by the receiver, and the voltage is given by

$$V^2 = 2R_i P_R \tag{2.18}$$

where R_i=50 Ohms is the impedance at the receiver. The amplitude is therefore proportional to the square root of power.

2.3 Trail Formation Models

In the simple case described above, there is no attenuation of radar echoes with height. Since this attenuation is observed, the simple model of an infinitely thin line of meteor plasma is not complete. In order to calculate the echo attenuation, the internal structure of the trail must be known: in particular, the trail's radial electron density. This problem can be addressed by modelling the formation of the trail.

2.3.1 Collisional models

In the simplest model of trail formation, each ablating atom is modelled as a hard sphere with a radius equal to the radius of its scattering cross section. The meteor trail is formed as ablated atoms of the meteor are slowed by collisions with air molecules to thermal velocities. According to Manning (1958), this process will take between 14 and 20 collisions; each collision will tend to reduce the forward momentum of the ablated atom. Since all meteors travel faster than 10 km/s, there will be enough kinetic energy in the collision between an ablated atom and a molecule in the atmosphere to ionize the meteor atom. The probability of ionization increases as the velocity to the third or fourth power (Bronshten, 1983; Jones, 1997), and approaches unity as the velocity approaches 70 km/s. It is therefore very probable that when the atom reaches thermal equilibrium, it will be ionized.

The electrons are much more mobile than the ions, but will tend to remain with the ions, preserving quasi-neutrality: the expansion of the trail is therefore determined by the motion of the ions. The distance travelled by each atom between collisions depends on its scattering cross section and on the atmospheric density. Manning (1958) assumes the scattering cross section to be that of ions at thermal velocities, but Massey & Sida (1955) argued that at meteoric velocities the fact that the atom is ionized makes little difference, and the scattering cross section should be that of neutral atoms. From Bronshten (1983), after Portnyagin and Tokhtas'yev (1974), Jones (1995) uses a scattering cross section proportional to $v^{-0.8}$, and the atomic rather than ionic scattering cross section. Since by this model atoms with higher velocities will have smaller scattering cross sections, they will tend to travel farther between collisions. This implies that faster meteors produce wider trails, so that faster meteors not only ablate higher than slower meteors, but will also have wider trails at a given height, further biasing radar observations against them.

The most important role of modelling is to determine the radial distribution of electrons, and hence how attenuation depends on wavelength (see section 2.4). The density of electrons (following the density of ions) is expected to be greatest at the

trail axis, and to taper off with increasing distance from the axis, but the form of the radial density function must be determined. Manning (1958) assumed that the electrons in a trail would have a Gaussian distribution. The simulation code of Jones (1995), on the other hand, gives a distribution closer to exponential, having a sharper central peak. In both models, the initial radius is defined as the root mean squared value of the radial distance of each electron from the trail axis.

The process of trail formation is considered complete when ablated atoms have reached thermal velocities. If the models of Manning (1958) and Jones (1995) are correct, this will require at most 20 collisions, after which the atom will have slowed from a speed of tens of kilometers a second to hundreds of meters a second. A simple simulation of hard spheres undergoing elastic collisions with stationary particles finds that on average 1 millisecond is needed for a meteoritic atom with a speed of 30 km/s to reach thermal velocities at 95 kilometers altitude: faster meteors reach equilibrium more quickly since they take less time for 20 collisions.

2.3.2 Plasma models

The hard sphere model is not exact for several reasons. It assumes that all molecules are spherical (which is not the case for many diatomic atmospheric gases) and it ignores any interatomic forces other than during collisions. It also ignores electric and magnetic forces on the ions from external fields. Magnetic effects will be important above 95 km, when the motion of electrons perpendicular to magnetic field lines will be retarded (Kaiser, 1968; Kaiser *et al*, 1969; Jones, 1991; Ceplecha *et al*, 1998). This will tend to produce trains with an elliptical rather than a circular cross section. Meteor trains should properly be treated as plasmas (Jones, 1991), with full account taken of the electromagnetic interactions between electrons and ions. The simulation in this case becomes much more complex than the hard sphere approximation.

Only simplified plasma simulations have been done; Oppenheim *et al* (2000) have modelled trails as two dimensional plasmas, using kinetic theory for the ions and a fluid model for the electrons. They predicted that the diffusion process will be turbulent on small time scales, producing a highly irregular electron density after 1.5

ms. The initial distribution of ionization had a Gaussian cross section and initial radius of approximately 1 meter. The simulation thus does not apply to the actual formation of the trail, but to its time development; even so, the simulation may provide useful information since the highest part of the trail will begin the diffusion process before the lowest part has finished forming. The meteor plasma modelled was only fifteen times the background density, and therefore similar to the faintest radar echoes at the maximum level of the E region. At typical meteor heights, the background ionization varies from 10^8 m^{-3} to 10^{10} m^{-3}: meteor trails can vary from ten to ten thousand times the background electron density. The numerical solution was less accurate at higher densities. Because the model uses only two dimensions, uses a fluid model for the electrons and simulates a trail less dense than those being studied, the results were not used in our models, but further research along these lines may yield important insights into the final structure of the trail.

Turbulence in the trail (Dyrud *et al*, 2002) may act to oppose the magnetic field, allowing trails to diffuse uniformly even at heights greater than 95 km. Jones (1991) suggested that even where magnetic fields strongly affect diffusion, the initial distribution will be roughly circular since the atoms will be ionized only after several collisions. Before ionization, their motion will be unaffected by the magnetic field.

2.3.3 Initial radius as a function of height

Initial radius varies with height. The collisional models predict that the initial radius should increase directly as the mean free path; this would mean that it increases exponentially with height. Most attempts to describe the height dependence of initial radius use mean free path to some exponent with a value between 0 and 1, of the form:

$$r_i \propto \ell^n \tag{2.19}$$

where ℓ is the mean free path and n the exponent. The theories of the trail formation of non-fragmenting meteors of Manning (1958) and Jones (1995) predict that the

value of n should be 1.

2.4 Reflection from a Trail of Finite Width

When a radar beam is reflected from a trail with a nonzero initial width, different electrons will be at slightly different distances to the radar, and the returns will not be in phase. The attenuation of an echo due to initial radius effects can be calculated by summing the reflection from each electron. The contributions from each electron will be equal in amplitude, but will have different phases depending on the position of the scattering electron. The attenuation will depend on the sum of the phases of the reflection from each electron. We obtain an integral for amplitude of the form:

$$a\left(\vec{k}\right) = a_0 \int n\left(\vec{r}\right) e^{i\vec{k}\cdot\vec{r}} d\vec{r} \tag{2.20}$$

for a thin slice of cylindrical column of ionization (Figure 2.5). Here $\vec{k}$ is the wave vector, $\vec{r}$ is the position vector of the electron relative to the axis of the cylinder, and a_0 is the amplitude of the same trail with no width.

If the trail has cylindrical symmetry, the density of electrons $n\left(\vec{r}\right)$ depends only on the distance from the trail axis, so $n\left(r,\theta\right) = n\left(r\right)$. The equation reduces to:

$$a\left(k\right) = a_0 \int_{r=0}^{\infty} \int_{\theta=0}^{2\pi} rn\left(r\right) \left(\cos\left(kr\cos\theta\right) + \imath \sin\left(kr\cos\theta\right)\right) dr d\theta. \tag{2.21}$$

The integral over θ can be split into cosine and sine components. The sine function is antisymmetric about π in θ, so that integral is 0. We are left with:

$$a\left(k\right) = a_0 \int_0^{\infty} rn\left(r\right) \int_0^{2\pi} \cos\left(kr\cos\theta\right) dr d\theta. \tag{2.22}$$

A Bessel function of the first kind is defined as:

$$J_0\left(x\right) = \frac{1}{\pi} \int_0^{\pi} \cos\left(x\sin\theta\right) d\theta. \tag{2.23}$$

In order to make the integral in equation 2.22 analogous to that in equation 2.23, we substitute $\theta' = \theta + \frac{\pi}{2}$ into equation 2.22. Since the integrand is symmetric about

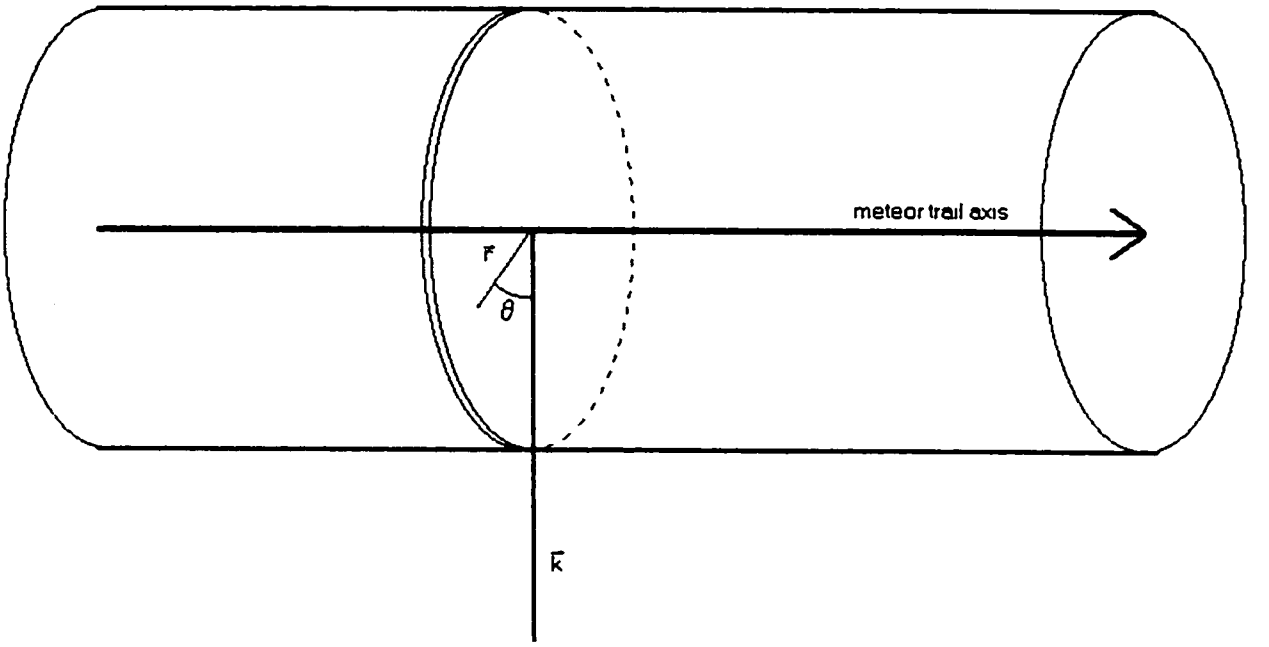

Figure 2.5: Reflection of radar signal from an electron in a meteor trail

π, we can also change the upper integration limit from 2π to π, taking out a factor of 2:

$$a(k) = 2a_0 \int_0^{\infty} rn(r) \int_0^{\pi} \cos(kr \sin\theta') \, dr d\theta'. \tag{2.24}$$

Substituting equation 2.23, the definition of a Bessel function, in equation 2.24, we have:

$$a(k) = 2\pi a_0 \int_0^{\infty} rn(r) J_0(kr) \, dr \tag{2.25}$$

so the amplitude is proportional to the Fourier-Bessel transform of the electron density function. The attenuation depends both on the wavelength of the radar and on the radius of the trail. If the electron density function is Gaussian, the Fourier-Bessel transform is also Gaussian; and according to Jones (1995) the transform is approximately Gaussian if $k^2\langle r^2 \rangle \ll 1$. Otherwise we must solve equation 2.25 exactly to obtain the relation between amplitude and wavelength/initial radius. Figure 2.6 shows the Fourier-Bessel transforms of a Gaussian and an exponential.

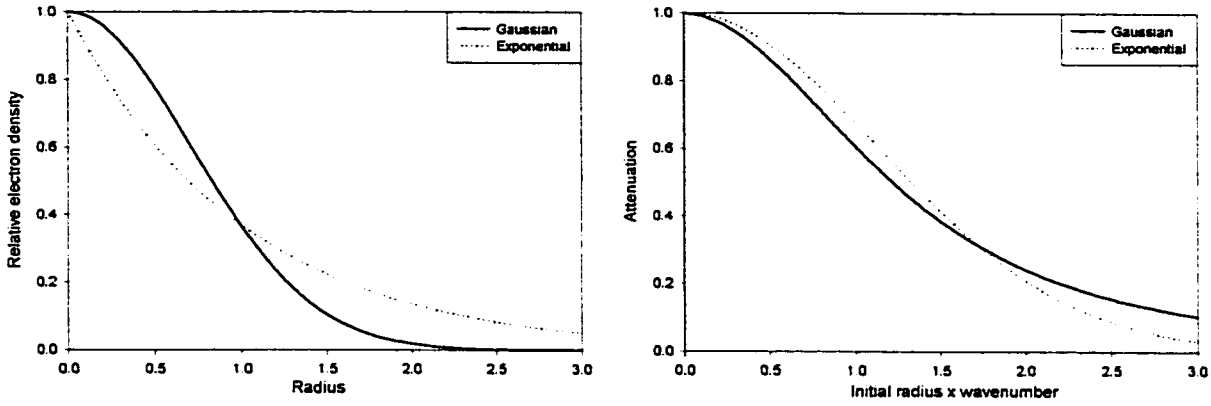

Figure 2.6: Fourier-Bessel transforms of an exponential and a Gaussian function

2.5 Determining Initial Radius from Radar Observations

The first attempt at determining the attenuation of echoes as a function of height was made with the radial distribution generated with the code of W. Jones (Jones, 1995). The method used was similar to that of Greenhow & Hall (1960), using the exponential radial distribution instead of a Gaussian. The number of echoes seen on each frequency in a given height interval are plotted. The number at the longer wavelength is assumed to be correct, and the number at the shorter wavelength is corrected by that amount. If the trail is assumed to be Gaussian, the amplitude after attenuation will be:

$$a = a_0 \exp\left(-\left(\frac{2\pi r_0}{\lambda}\right)^2\right) \tag{2.26}$$

where a_0 is the amplitude without attenuation, r_0 is the initial radius and λ is the wavelength. If one takes the ratio of the amplitudes at two different wavelengths, one has:

$$\frac{a_1}{a_2} = \exp\left(-(2\pi r_0)^2\left(\frac{1}{{\lambda_1}^2} - \frac{1}{{\lambda_2}^2}\right)\right). \tag{2.27}$$

The number of meteors seen can be related to the smallest mass detectable by the system with the mass distribution index of the meteoroid population. We assume

that the masses of particles follow a power law of the form:

$$dn \propto m^{-s} \tag{2.28}$$

where dn is the number of particles falling inside the mass range m to $m + dm$, and s is the mass distribution index. For any positive s, the number of particles at a given small mass will be larger than at a large mass. The higher the value of s, the greater the excess of small particles will be. Showers typically have s values of around 1.7; sporadic meteors have an s between 2 and 2.3.

Integrating this equation from the smallest mass, we have a cumulative number of meteoroids N_C

$$N_C \propto \int m^{-s} dm \tag{2.29}$$

or

$$N_C = C m^{1-s} \tag{2.30}$$

larger than mass m. C is a constant.

Since the amplitude of an echo is proportional to the mass of the meteor, and the number of echoes seen is related to the smallest detectable mass of the system, the ratio of the numbers of echoes seen on each radar at a particular height is related to the amplitude ratio at that height as:

$$\frac{a_1}{a_2} = \left(\frac{N_1}{N_2}\right)^{1-s} \tag{2.31}$$

where s is the mass distribution index. If s is assumed to be 2, the amplitude ratio will be equal to the number ratio.

Starting with the ratio of numbers of echoes at two different wavelengths, one can calculate the initial radius, and then calculate the absolute number of echoes. Greenhow & Hall (1960) used both number ratios and amplitude ratios to find their relation of attenuation and height. To find the percentage of meteors detected at any

frequency, they plotted three points for the three radars and fitted a spline curve to them.

There are several difficulties with each approach. The attenuation as a function of wavelength must be known: if the meteor trails do not have a Gaussian distribution, the attenuation function will not be Gaussian. When comparing numbers of echoes, the two radars used must have a well known limiting magnitude and no differences in the selection criteria for echoes. When comparing amplitudes, factors like the transmitted power, receiver calibrations and gain patterns of the antenna must be taken into account. A systematic shift of 1% in the amplitude ratios was found to have little effect on the results. The amplitudes must therefore be measured to within 1%, and the transmitter powers to 2%.

Number comparisons on different frequencies were not practical for our systems because of the interference that affected the 17.45 MHz observations daily and occasionally the 29.85 MHz observations. Instead, amplitude ratios were used to calculate the initial radius assuming the electron density function was exponential.

With this method, the initial radius was calculated at all heights with sufficient numbers (Figure 2.7). The radius shows a slight increase and then a decrease with height on both pairs of frequencies, with significant error on most of the points, and the values obtained with different systems do not agree.

Using different functional forms gave no better results, and no simple solution could be found. The results depended on the day the data were taken, and often no solution could be found. Plotting individual amplitude ratios (see Figure 4.5) showed that the source of the problem was the large scatter in the points, which is not predicted by the simple theory.

From these results, it was apparent that a more detailed analysis of the problem was required. The amplitudes and heights had to be measured very precisely, to remove as much measurement error as possible. It also was unlikely that a simple model could explain the results, so a more detailed model had to be constructed along with a more detailed examination of the data.

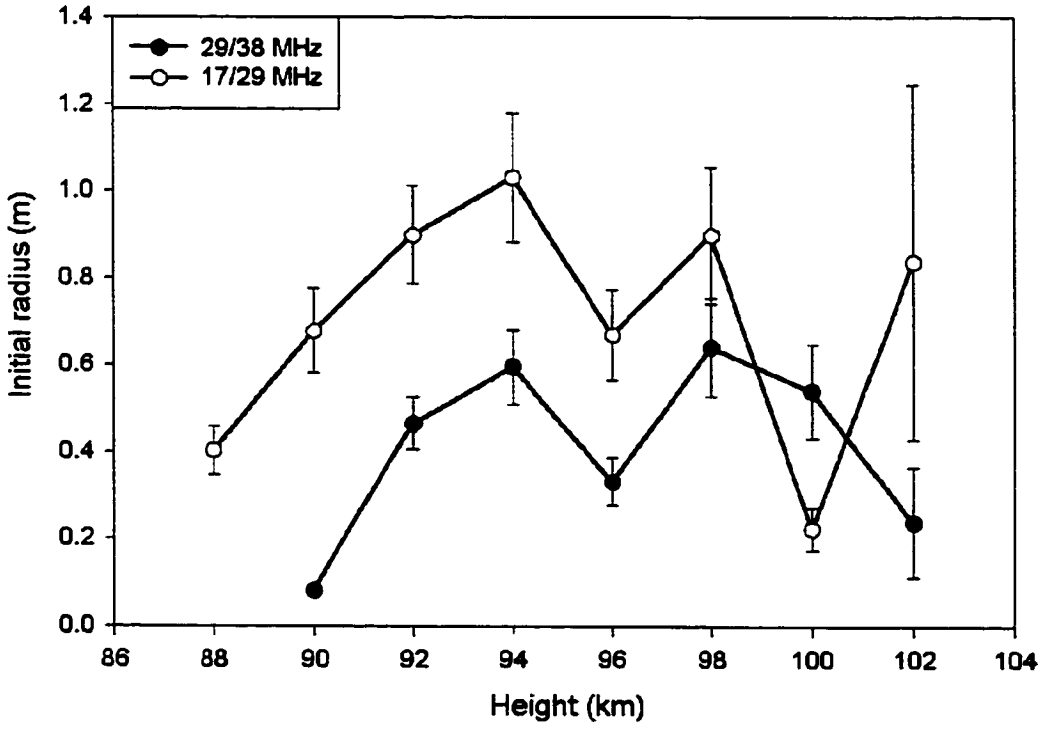

Figure 2.7: Calculated initial trail radius with simple model of trail for two pairs of radar frequencies

2.6 Further Attenuation Due to Fragmentation

2.6.1 Fragmentation

There are a number of reasons for including fragmentation in the model. All experimental studies of initial radius seem to indicate that the initial radius increases more slowly with height than expected from theory (e.g. Greenhow & Hall (1960), Baggaley (1970)). Hawkes & Jones (1978) proposed fragmentation as an explanation of this phenomena. The fragmentation theory is supported by many observations (McCrosky, 1955; Jacchia, 1955; Hawkins & Whipple, 1958; Öpik, 1958; Campbell *et al*, 1998). Hawkes and Jones argue that, in the process of colliding randomly with other meteoroids in space, most particles will acquire a net spin. When the object fragments in the atmosphere, the smaller fragments will therefore be thrown away from the axis of rotation with some initial velocity. This may produce a distribution of fragments with a large lateral scatter.

Fragmentation can be added to an attenuation model in a fairly straightforward manner. Since all echoes under consideration are underdense, the trail of electrons from each individual fragment can be treated independently of all the others. The resulting radar echoes can be summed, taking into account that the phases of the echoes from each will be slightly different due to lateral separation of the grains. The grains can be assumed to have some distribution with respect to the axis of the meteor's path; they will also have some size distribution and a total radius which may depend on height.

There is currently no way to determine the radial distribution of the fragments. A few likely candidates are Gaussian, radially uniform, and exponential distributions: also, a hollow trail where few of the fragments lie on the trail axis is possible (Figure 2.8). The distribution will depend on the circumstances of fragmentation and on the dynamic flight of each fragment after separation from the main body.

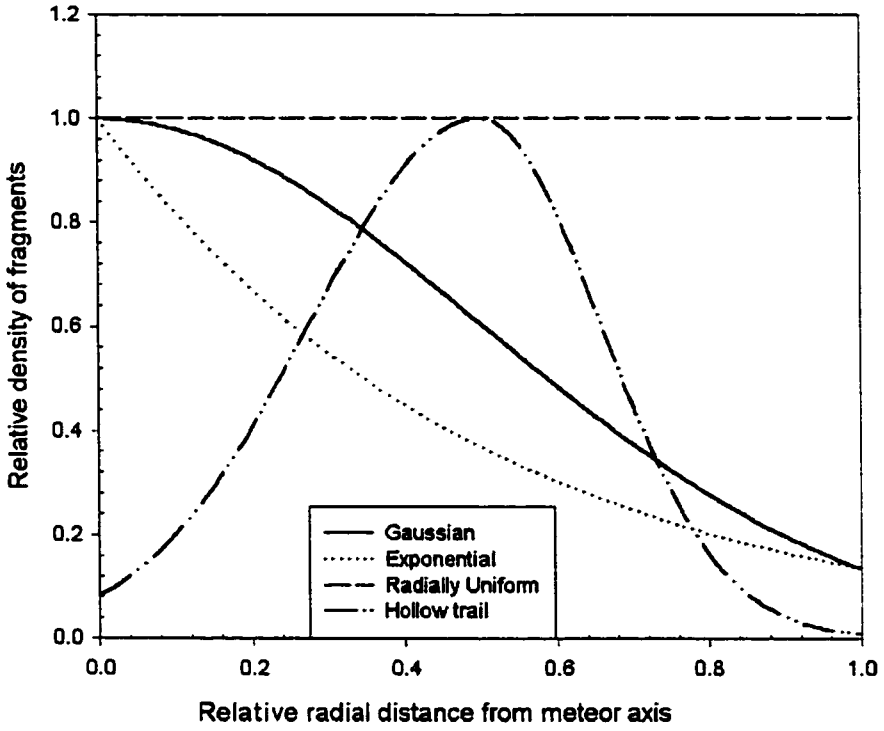

Figure 2.8: Possible radial density functions of fragments

2.6.2 Height dependence of fragmentation radius

The height dependence of the fragmentation radius, or radial spread of the fragments, must also be experimentally determined. The meteor fragments may spread out during the luminous portion of its trajectory, increasing the fragmentation radius with decreasing height. Alternatively, if larger fragments stay closer to the axis than smaller fragments, the fragmentation radius may decrease with height as the small outer fragments are ablated and only the large fragments remain (Figure 2.9). The simplest model assumes a linear dependence of fragmentation radius on height, with two coefficients to be determined, a and b.

$$r_f = ah + b \tag{2.32}$$

These coefficients can be found by fitting multi-frequency radar observations to theory, assuming that each fragment produces a particular distribution of electrons, the radius of which is proportional to the mean free path.

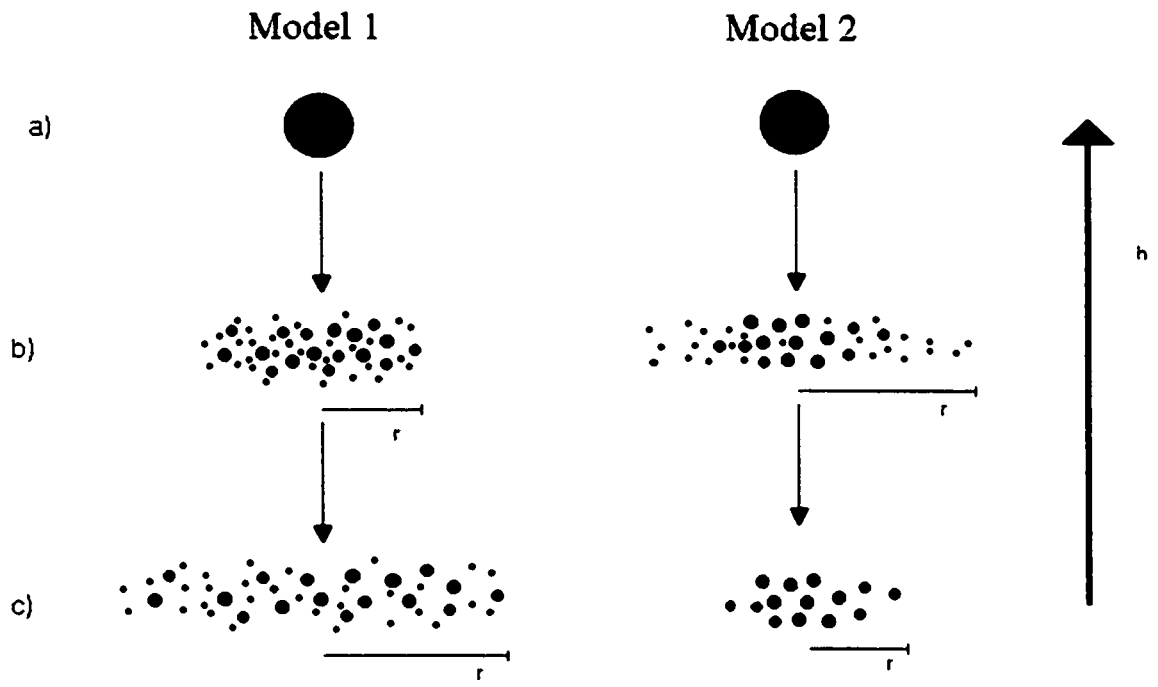

Figure 2.9: Possible development of fragmented meteor. At a), the meteor is still a single object. At b), it has just broken apart; at c) it has travelled some distance.

2.7 Summary

The important functions in calculating the effects of initial trail radius are: the radial dependence of the electron density in a trail, the radial dependence of fragment density of a meteor, the height dependence of the initial radius of a single trail, and the radial dependence of fragments from the meteor axis. For each of these, a functional form must be chosen and the coefficients can then be found. In addition, the mass distribution index of the fragments must be determined. Some can be found by modelling and comparing video data: the others must be found with multi-frequency radar data.

Chapter 3

Equipment

3.1 Tavistock Radar

As discussed in the previous chapter, we planned to use accurate amplitude ratios of meteor echoes observed on several frequencies to determine the attenuation due to initial radius. This requires that the radar systems be very well calibrated, so that differences in amplitudes are not caused by differences in transmitter power or receiver calibrations. The errors on these two quantities should be no more than 2%.

A triple frequency SKiYMET HF/VHF radar was constructed both as a meteor patrol radar and to investigate the initial radius effect. The radar is a joint product between Mardoc Inc. of Canada and Genesis Software of Australia. The hardware was built by Tomco Electronics, operating software and computer hardware provided by Genesis Software of Adelaide Australia, and Mardoc Inc. supplied the scientific analysis software and the antennas. Except for the frequencies, each radar system was constructed identically. The systems were designed to be operated simultaneously and for real-time detection and analysis of meteors. The detection software was designed for investigation of atmospheric winds with meteor trails, but was used in this case for the detection of all meteors. The three radars operated at 17.45 MHz, 29.85 MHz and 38.15MHz (referred to hereafter as 17, 29 and 38 MHz), and had peak powers of 6 kW. They were located in Tavistock, Ontario (43.264N, 80.772W).

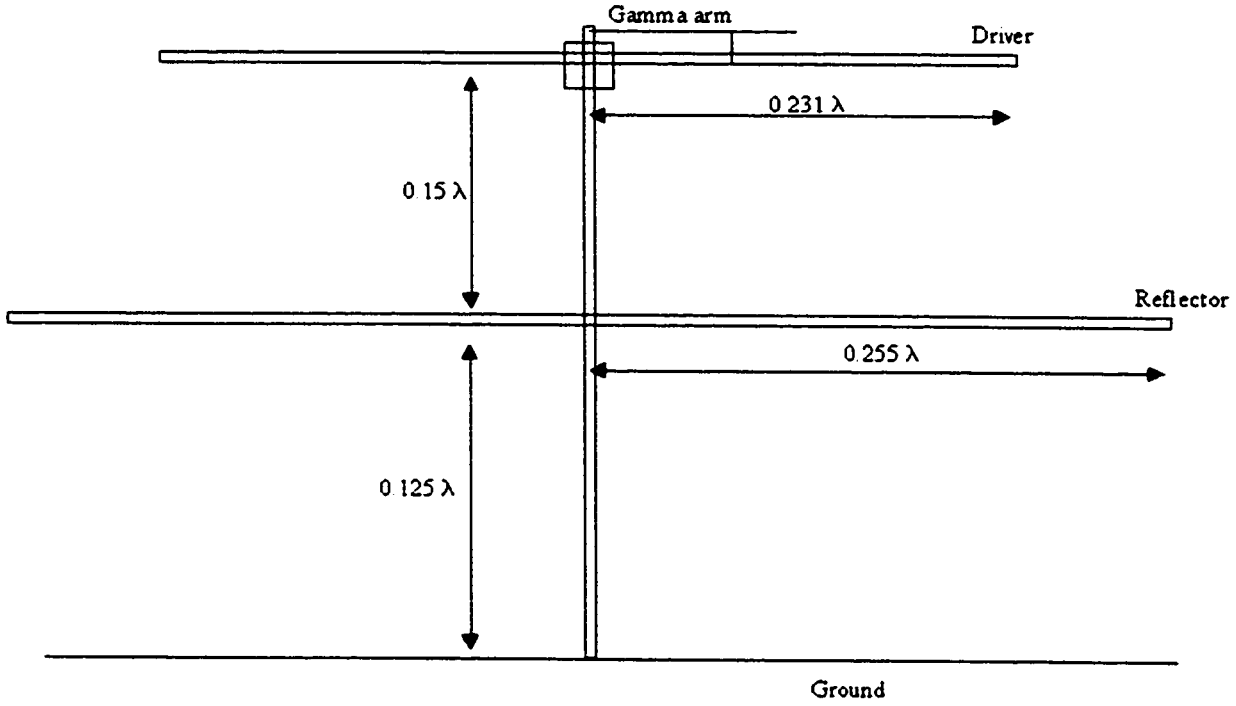

Figure 3.1: Dimensions of receiver antennas

3.2 Antenna Layout

3.2.1 Antennas

The antennas for the Tavistock system were designed to detect meteors over most of the sky. This broad radiation pattern provided the best possible coverage for sporadic sources at all times. The transmitting antennas were simple three element Yagi antennas. The receiving antennas were two element Yagis (Figure 3.1, Figure 3.2). The sensitivity varied slightly azimuthally, the maximum sensitivity on each system being toward the east and west; it also varied with elevation and had the greatest gain at an elevation of 35°. The gain patterns were calculated using the NEC software package (Figures 3.3 and 3.4). The software takes as input the dimensions and physical parameters of the antennas, and uses assumptions about the properties of the ground (conductivity $\sigma = 0.03$ Siemens/m and dielectric constant $\epsilon_r = 20$) to calculate the gain pattern. The patterns calculated were used in all analysis and simulations.

The maximum gain of the transmitting antennas was roughly 7.5 dBi for all three

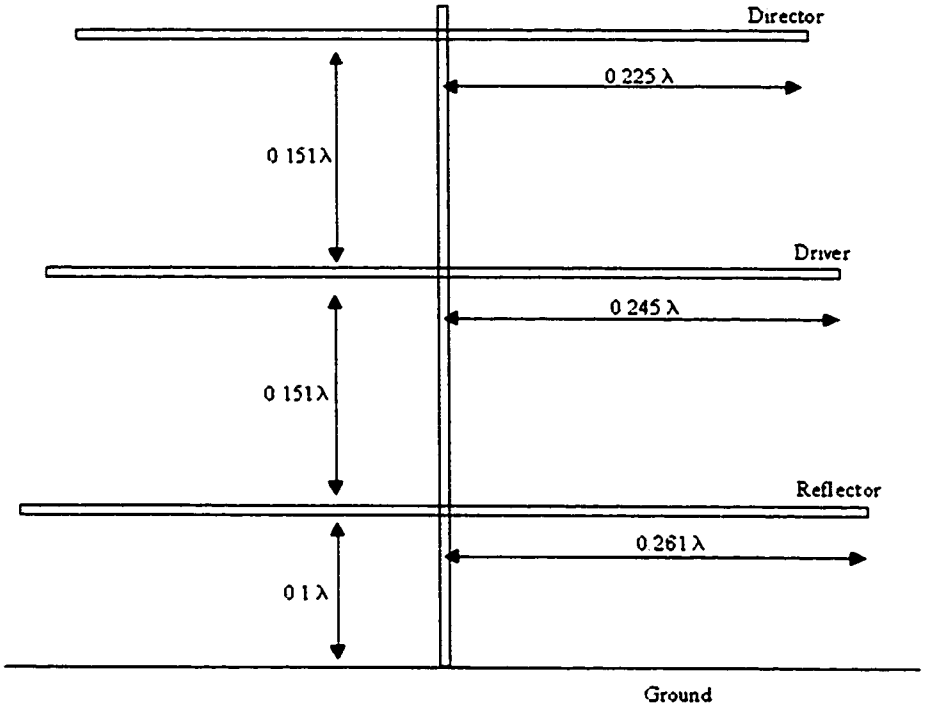

Figure 3.2: Dimensions of transmitter antennas

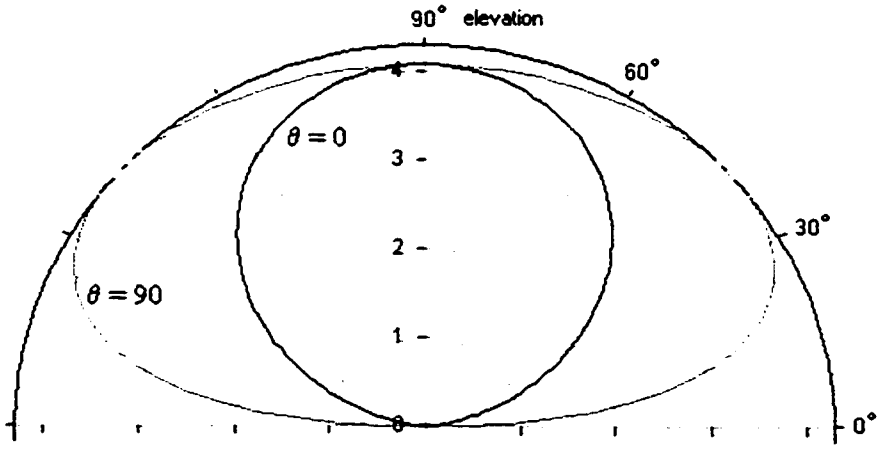

Figure 3.3: Gain of Tindal2 receiving antenna at 0° and 90° azimuth in linear units

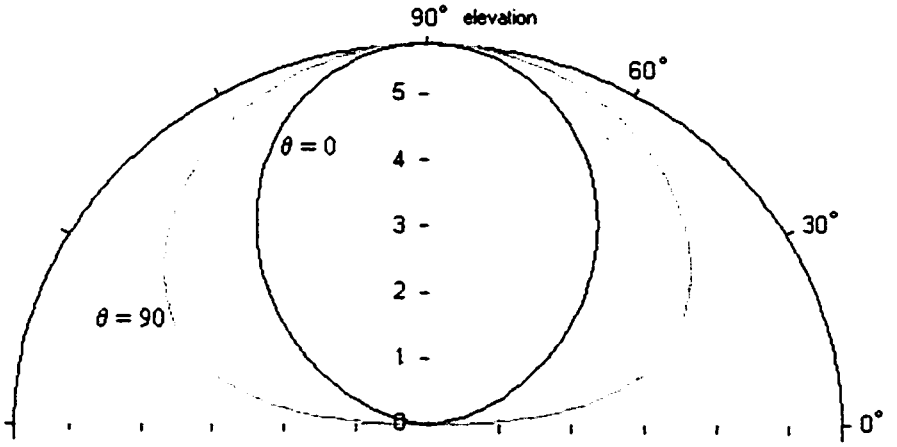

Figure 3.4: Gain of Tindal2 transmitting antenna

systems, or 5.6× that of an isotropic radiator. The receiver antennas had a maximum gain of 6.3 dBi, or 4.3× isotropic. Each system had one transmitting antenna and seven receiving antennas. The antennas were connected to the radar trailer with RG-213 coaxial cable, which had an impedence of 50 Ohms. The phase shift of each cable was measured and accounted for in the analysis software.

3.2.2 Interferometer

In principle, only two antennas are needed in a particular direction to specify the angle to the echo in that direction (Figure 3.5). Since the phase difference between the two antennas, caused by the difference in path length, will be

$$\psi = -\frac{2\pi\Delta s}{\lambda} \tag{3.1}$$

and $\Delta s = d\sin\phi$, where ϕ is the zenith angle, the zenith angle can be found as:

$$\sin\phi = -\frac{\lambda\psi}{2\pi d}. \tag{3.2}$$

If the antenna spacing is less than $\lambda/2$, there will be a unique solution. If the spacing is greater than $\lambda/2$, there will be many possible solutions all separated by 2π. However, antennas with spacings less than $\lambda/2$ suffer from mutual coupling which can

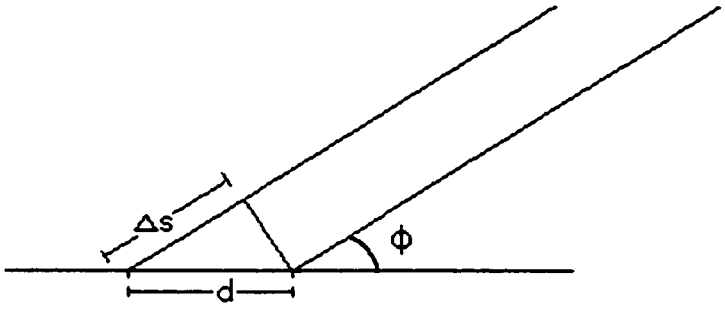

Figure 3.5: Two element interferometer

introduce large errors in the phases measured at each (Hocking *et al*, 1997; Jones *et al*, 1998). Jones *et al* (1998) proposed a three element design to remove the ambiguities while keeping the antennas far enough apart to ensure that no significant coupling took place between the antennas. The two outer antennas are spaced at 2 λ and 2.5λ from the center, reference antenna. The phase on each of the outer antennas is determined relative to the phase of the center antenna, giving two equations for the zenith angle:

$$\sin\phi = -\frac{\lambda\psi_1}{2\pi d_1} \tag{3.3}$$

and

$$\sin\phi = -\frac{\lambda\psi_2}{2\pi d_2}. \tag{3.4}$$

The zenith angle can calculated using two values: the sum and the difference of the two phases.

$$\sin\phi = -\frac{\lambda\left(\psi_1 - \psi_2\right)}{2\pi\left(d_1 + d_2\right)} \tag{3.5}$$

$$\sin\phi = -\frac{\lambda\left(\psi_1 + \psi_2\right)}{2\pi\left(d_1 - d_2\right)} \tag{3.6}$$

Equation 3.6 has a "virtual separation" of antennas $d_1 - d_2$ of $\lambda/2$, so there is a unique solution. This solution will not be very precise, however: even small phase errors give a large uncertainty in angle. Equation 3.5 will give a much more precise

answer, but will be ambiguous. The answer to equation 3.6 can be used to choose the correct solution to equation 3.5, provided the phase errors are not too great.

The angle can be refined further with another antenna at a still greater distance. This will give even more solutions, closely spaced: the correct solution can be chosen from the solution to the first two equations. In principle, provided the signal to noise ratio of the echo is high enough to yield sufficiently accurate phase measurements, the baseline could be increased further and more accurate angles could be obtained, but using a total baseline of 7λ is sufficient for most purposes.

By using two orthogonal arrays, the elevation and azimuth can be uniquely determined to better than 2° (Jones *et al*, 1998). By comparing angles measured on two of the systems for the same meteors, one can obtain an estimate of the actual error. The standard deviation in zenith angle is roughly 1° and in azimuth it is 0.4°, as estimated from comparison of 29 MHz and 38 MHz observations of identical meteors.

Each radar system has seven receiving antennas laid out in the manner described above (Figure 3.6). The three arrays were arranged with a minimum of overlap in the field (Figure 3.7). The antenna arrays were aligned and their orientations measured by sighting astronomical objects and calculating azimuths. All arrays had their main axis 16° West of North. The terrain was very level, making differences in heights for the antennas negligible. The only significant irregularities were present in the 17 MHz array, which covered the greatest area; no attempt was made to correct for these.

The design of the interferometer is due to Jones *et al* (1998).

3.3 Transmitter and Receivers

The transmitter consists of six solid-state units, each of which is capable of producing 1 kW of power. The transmitter unit is capable of generating 6 kW, but the exact power level can change over time due to failed modules and other technical malfunctions. The power output of the transmitter must be known accurately for meaningful comparison between frequencies: for this purpose a power monitoring system has been installed and calibrated. The power monitoring system measures the power ev-

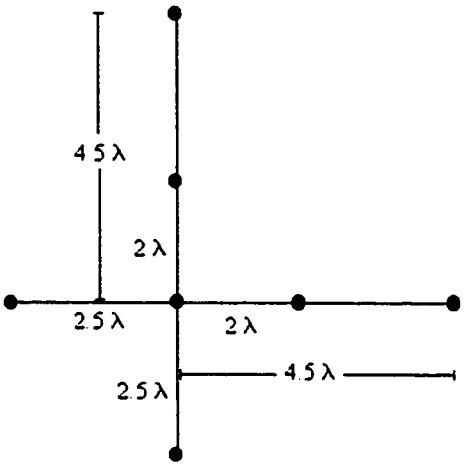

Figure 3.6: Interferometer array spacing in wavelengths

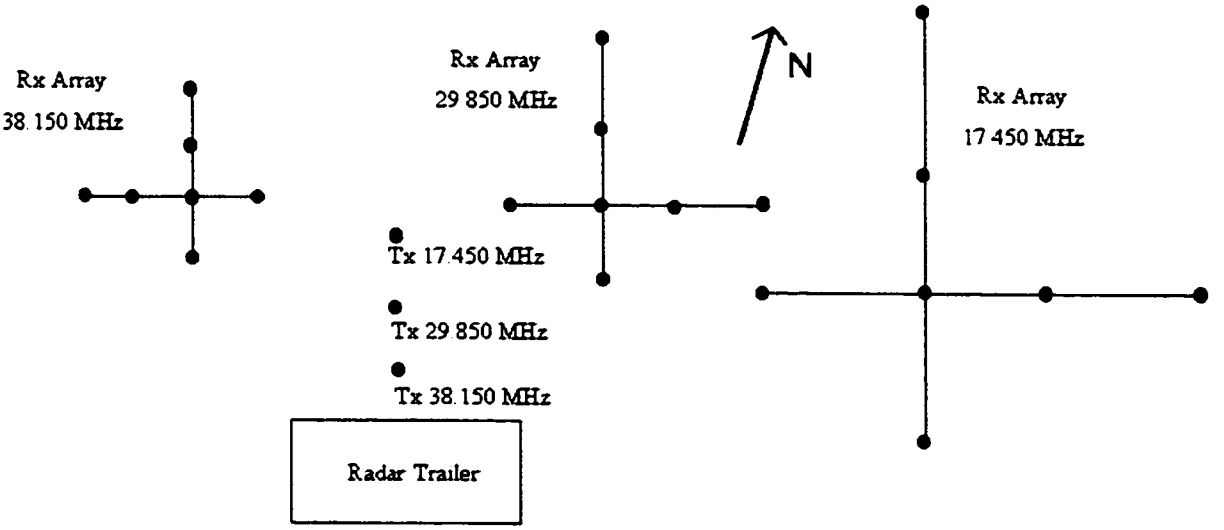

Figure 3.7: Ground plan of three antenna sets for Tavistock multifrequency radar

ery 30 minutes and writes the values to a text file. The system was calibrated using a calorimeter power meter.

The receiver unit consists of seven identical receivers, one for each antenna. Each produces a voltage which is translated into amplitude, a 16 bit binary value. The receivers must be calibrated to determine the relation between voltage and amplitude in order to calculate the received power. This is done by replacing the antenna by a signal generator and measuring the amplitude from the receiver; knowing the input power it is possible to calculate the voltage and, by altering the generated power, to calculate the proportionality between power and voltage.

3.4 Basic Radar Parameters

The most basic radar can determine range, time and amplitude of a signal. A pulse is produced in the transmitter, sent from the transmitting antenna, reflects off the observed object and is received at the receiving antenna. The time the pulse takes between being transmitted and received can be used to calculate the distance. Since the pulse travels at the speed of light c, and covers twice the range in a time Δt, the range can be found as:

$$R_0 = \frac{1}{2} c \Delta t. \tag{3.7}$$

Problems may occur if the pulses are close together compared to the total region to be sampled: there may be more than one possible range for a given echo. This can be avoided by reducing the pulse repetition frequency (PRF), but this lowers the total power output.

The total power output is the product of the peak power generated by the transmitter and the duty cycle. The radar produces pulses of width d, at intervals of $\frac{1}{PRF}$ (Figure 3.8). The duty cycle describes the amount of time during each cycle where the transmitter is active.

Ideally, if precise amplitudes are needed, the pulse is a perfect rectangle. Its width determines how accurately range can be determined. In practice, because the pulse

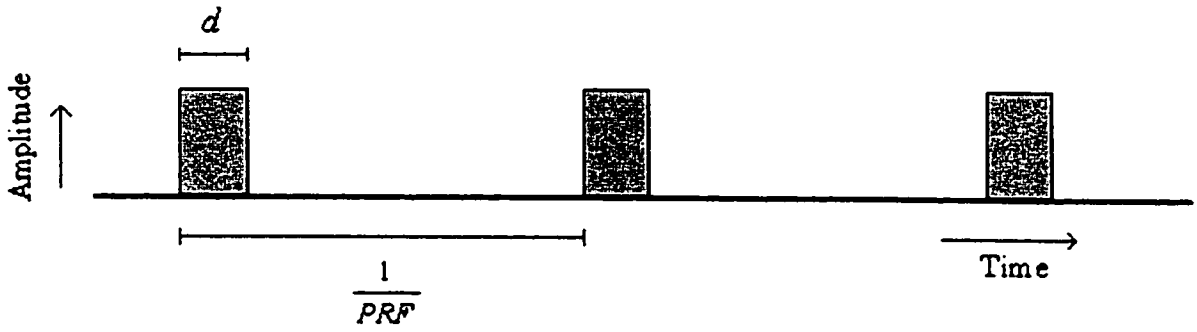

Figure 3.8: Transmitter pulses

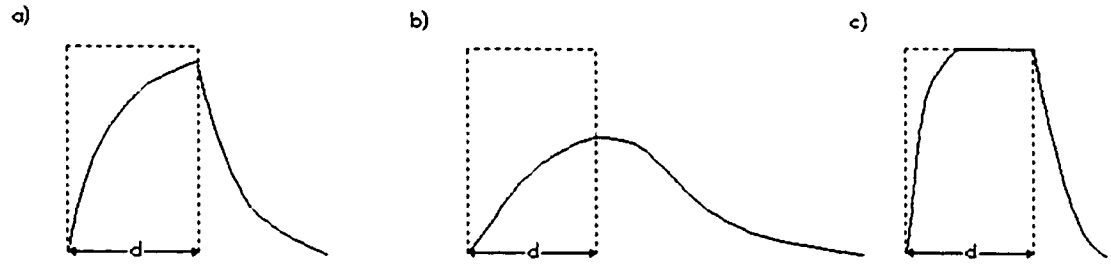

Figure 3.9: Rectangular pulses after passing through a bandwidth filter. a) with $\Delta f = 1/d$; b) with $\Delta f < 1/d$; c) with $\Delta f > 1/d$.

must be sent with a particular bandwidth Δf, the shape will not be perfectly square. The amount of distortion depends on the relative sizes of the pulse width and the bandwidth: if Δf is smaller than $1/d$ then the pulse will be spread significantly and will not reach its maximum amplitude. If Δf is larger than $1/d$ the pulse will be only slightly distorted (Figure 3.9). If the pulse is not square, the amplitude cannot be determined very precisely from a single sample, since that sample may fall anywhere on the returned pulse and is not necessarily the peak amplitude (Figure 3.10). During the data collection for this experiment, the pulse resolutions were either 4 or 8 kilometers long, corresponding to temporal lengths of 26.6×10^{-6} seconds and 53.2×10^{-6} seconds. A 50 kHz bandwidth was used, which is larger than $1/d$ for both modes. The pulses were therefore only slightly distorted from their original shape.

Accurate ranges are essential, since they are needed to calculate accurate heights.

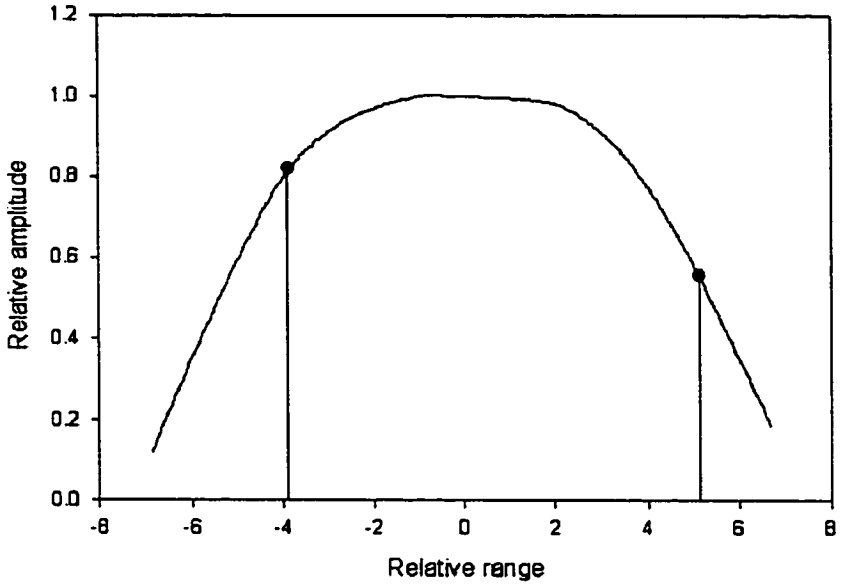

Figure 3.10: Undersampling a pulse

Accurate amplitudes are also required, otherwise the ratio of amplitudes on different frequencies is meaningless. We chose therefore to use a long pulse, a lower PRF and to sample the returned pulse many times. Each sample will be offset from the next by one range bin. If the shape of the pulse is known, each return can be fitted to a curve and the maximum amplitude and corresponding range can be calculated (Figure 3.11). The pulse shape can be determined by oversampling a long pulse and plotting the returns (Figure 3.12).

We simulated echoes from meteors with various pulse lengths and sampling intervals to determine the minimum number of samples per pulse required to obtain an accurate estimate of the amplitude. Noise was added to each return in a random way. We found that, using a shaped pulse of width T, having a sampling interval between $0.3T$ and $0.4T$ was sufficient to find the maximum amplitude to within the noise limits. This could be sampling every 1.5 km for a 4 km pulse or every 3 km for a 8 km pulse. Not all meteors will be sampled the required 3 times, but because the tapered edges of the pulse extend past the width, most meteors with significant signal to noise ratios will.

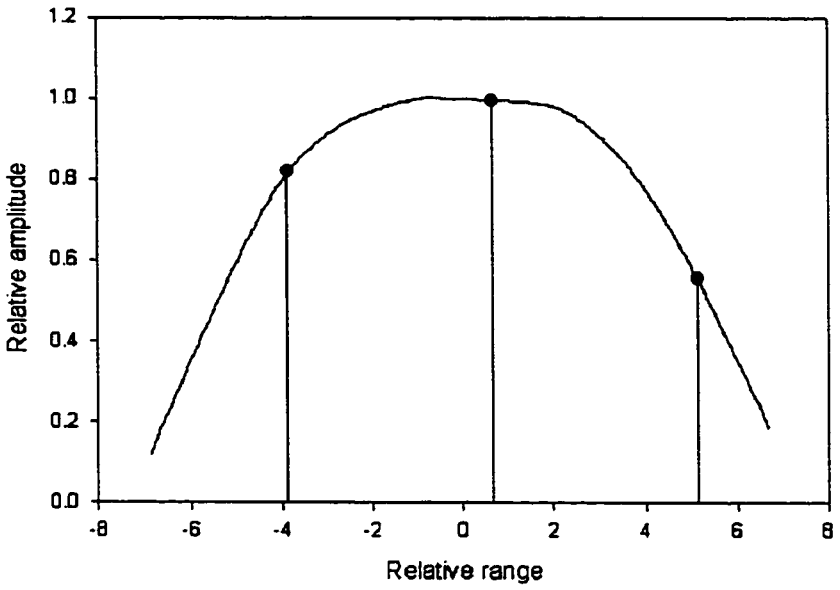

Figure 3.11: Well-sampled pulse

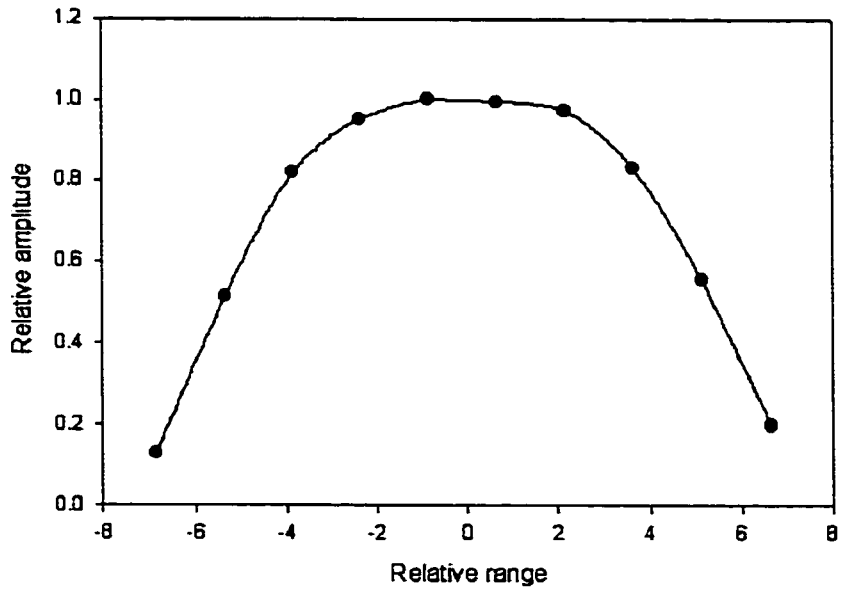

Figure 3.12: Actual 10 km pulse, sampled at 1.5 km intervals, on 29 MHz system

Table 3.1: Sky noise temperatures for three frequency radar; daily minimum and maximum

f (MHz)	Tmin (K)	Tmax (K)
17.45	30 000	500 000
29.85	15 000	100 000
38.15	8 000	80 000

3.5 System Limits

3.5.1 Noise

It is important to calculate the noise of each system in order to determine the limiting magnitude, since the faintest meteor visible will depend on the background levels. On the 29 and 38 MHz systems, the main source of noise is cosmic. On the 17 MHz system, terrestrial interference is much larger than cosmic noise for parts of the day: it has a large diurnal variation. Noise power P_n in radio systems is usually defined as

$$P_n = kT_{eff}\Delta f \tag{3.8}$$

where k is the Boltzmann constant, Δf is the bandwidth of the radar, and T_{eff} is an effective temperature, which has nothing to do with the operating temperature of the radar but is equivalent to the noise in a resistor which dissipates more energy when warmer.

The cosmic noise temperature on the three systems varies between 10^4 K and 10^6 K (Table 3.1). By contrast, the noise in the transmission lines and receiver has an effective temperature of order 360K, several orders of magnitude less than the sky temperature. The noise introduced by the equipment can therefore safely be ignored.

It is interesting to note that the noise on each system follows a nearly sinusoidal trend over the course of each day. If the noise level is plotted along with the elevation of Casseiopeia A, a supernova remnant, it is clear that most of the noise on these systems is due to radiation from that object (Figure 3.13). From the elevation of

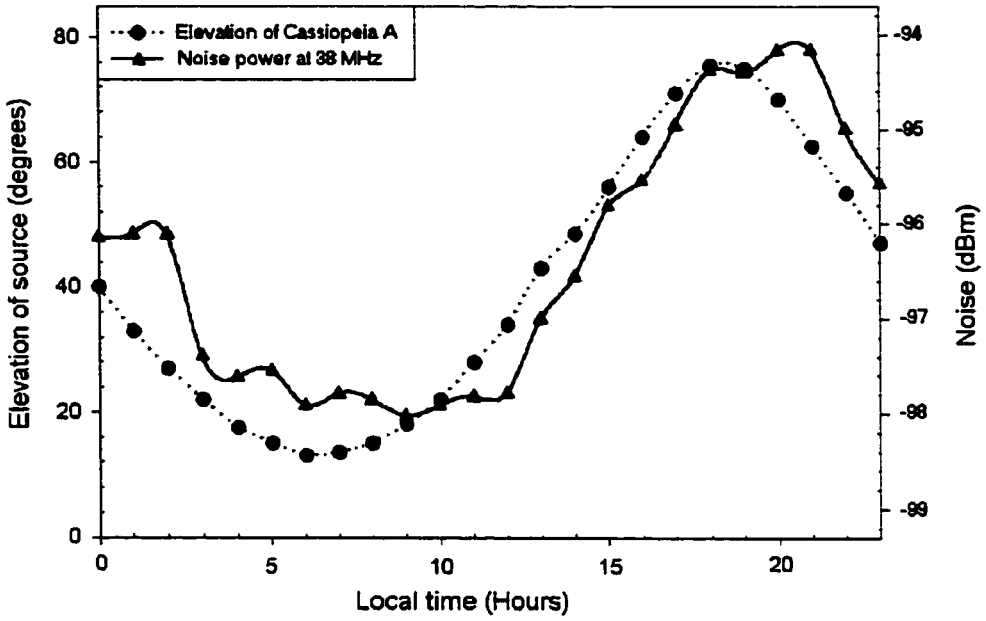

Figure 3.13: Measured noise levels on 38 MHz system on 12/12/1999, and elevation of Cassiopeia A supernova remnant for same day.

Cass A it is therefore possible to calculate the noise at any time of day on any day of the year.

3.5.2 Limiting sensitivity

If the noise power is known, the limiting magnitude can be calculated in a straightforward manner. The minimum echo strength required for detection is set to five times the noise power in the detection software. The electron line density of this meteor can be calculated from equation 2.16, which can be rearranged as follows:

$$q = \left(\frac{R_0}{\lambda}\right)^{\frac{3}{2}} \left(\frac{5P_N}{2.5 \times 10^{-32} P_T G_T G_R}\right)^{\frac{1}{2}} \tag{3.9}$$

where P_N is the noise power. Knowing q, the radar magnitude is defined to be:

$$M_r = 42.4 - 2.65 \log q \tag{3.10}$$

for non-shower meteors (McKinley, 1961). Radar magnitudes were developed using simultaneous visual and radar observations (Lindblad, 1956; Millman & McKinley,

1956), but do not necessarily correspond to optical magnitudes for meteors fainter than magnitude 5^M.

The exact limiting magnitude will vary with the transmitter power, and is different for different altitudes and azimuths. Using peak power values of 6 kW for each system, and taking the most typical altitude, the limiting electron line density for all three systems is approximately 10^{13} electrons/meter, corresponding to a magnitude of $+9^M$. This corresponds to a mass of 10^{-7} kg.

3.6 Detection Software

The detection software for the Tavistock radar was written for the SKYiMET meteor radars (see Hocking *et al* (2001) for a complete treatment). It uses a two-stage process to detect the rapid increases in received power of meteor echoes, and applies filters to remove signals caused by airplanes, lightning, E-region ionospheric echoes, RF interference and other unwanted sources. In the first stage, broad filters are applied to isolate signals which may belong to meteors. These fairly unrestrictive tests can be done very quickly, so even at high echo rates the computing time is very small for each detection and the first stage can be accomplished in real time. The in-phase and quadrature amplitudes from each receiver are saved from a small interval of time around the possible meteor and these files are stored on the disk. The second detection stage operates in parallel, and for usual rates can finish the process within seconds: it does not interfere with the collection of data since it only runs when the processor has free time. If the load on the CPU is too high, it can wait and perform the analysis on the stored event files when the processor has free time.

The first task of the detector is to find sudden increases in amplitude. In order to do this efficiently, the in-phase and quadrature signals are averaged over four points, reducing the temporal resolution for this test only (the complete data set is saved and used in its entirety for the second stage of analysis). The amplitudes are then incoherently averaged on all channels: since the phases are different depending on the geometry, it is not possible to average them coherently in real time. If three points

in a row are found which exceed the standard deviation of the previous points by an amount greater than five standard deviations, the object is a possible meteor. If the event does not stay high for three points in a row, it is likely to be a noise spike.

Underdense meteors have a rapid rise in amplitude, and generally last less than three seconds. The next test then checks to see that the rise time is less than 0.3 s, and that the amplitude has returned to the noise level within three seconds of the peak. This will remove most aircraft, which generally take many seconds to pass through the beam, E-region echoes, and most overdense meteors.

Some forms of interference, including lightning and RF interference, may have significant amplitude variations and therefore not be discriminated against by the previous test. The next test then checks to make sure the decay is fairly smooth. A search is done for the place where the echo falls to 0.3 times the maximum amplitude. If the signal then rises again to 0.7 times the maximum, the event is rejected. This will also reject some overdense meteors.

If a signal is not noise, the rate of change of phase should be similar on all antennas. To enhance the signal, a complex cross correlation is done on each pair of antennas. In a standard cross correlation, two waveforms covering the same time interval with n points are compared. The time index, or relative start time, of one waveform is varied from -n to n, and for each time lag the two waveforms are multiplied where they overlap. The resulting values are summed and normalized, so that each lag has a corresponding number. Plotting the correlation function against time lag gives a new function which is a measure of how alike the waveforms are. The cross correlation is defined as:

$$Corr(t) \equiv \int_{-\infty}^{\infty} g(\tau + t)h(\tau)d\tau \tag{3.11}$$

where t is the lag. A complex cross correlation works in the same way, using complex amplitudes and yielding an in-phase and quadrature component to the correlation function.

$$CCorr(t) \equiv \int_{-\infty}^{\infty} g(\tau + t)^* h(\tau) \tag{3.12}$$

The rate of change of phase of this function at zero lag is found for each pair of antennas, and the variance compared. If the standard deviation of these numbers is high, then the signal is very noisy and is discarded. Meteors which have passed all the above tests are saved in a file containing all the amplitude data from 1 second before the peak to 3 seconds following it.

The initial detection algorithm removes most unwanted signals, but some may remain. The second stage analysis applies more rigorous tests.

In the first test, the peak amplitude is required to exceed the amplitude at other points by at least a factor of two. Three intervals are chosen for comparison: one including the first quarter second of the saved file, well before the meteor, the second just before the peak, and the third 0.7 s after the peak. Each 0.25 second interval is averaged and the RMS value compared to the peak.

Assuming the peak is sufficiently high, the part of the file before the meteor is examined. Since E-region echoes may have a sudden rise in amplitude which can be mistaken for a meteor, the second before the signal's occurrence is checked for correlation. Cross correlations are done on all pairs of antennas on the second before the signal appeared, and the rate of change of phase found for each. A true meteor will show no correlation among the antennas prior to the signal, while an aircraft or ionosphere echo suddenly increasing in strength will show correlation. If the standard deviation of the change of phase on the cross correlation on each pair of antennas is high in the second before the peak, the echo is rejected.

Finally, the same sort of test is applied to the region where the event occurred. If the standard deviation of the change of phase values is small, then the noise in the signal is low and the meteor is accepted. Most of the meteors which pass all these tests will be underdense, but a few overdense and transition echoes may be included if they have short durations due to wind or other disturbances.

3.7 Radiant Determination

In order to separate out meteors from a particular shower or sporadic source for flux measurements or for initial radius investigations, some way of determining radiants is necessary. It is not possible to find the radiant exactly for a particular echo without more information, but a statistical treatment allows fluxes of meteors from a particular radiant to be calculated. When a shower is very active, shower meteors can be separated from the sporadics with relatively few erroneous meteors.

The basic procedure is the method of Jones (Jones & Morton, 1977; Jones, 1977; Morton & Jones, 1982), described in detail in section 7.2. Specular meteor echoes are detected ninety degrees from the radiant, so for an echo to belong to a particular radiant it must lie on a great circle 90° away. The number of echoes which lie along a band 90° from the radiant and with a width equal to the angular error of the interferometer is roughly the number which come from that radiant. This basic procedure can be used to find shower meteors for analysis, or as a starting point for flux calculations.

Some of the echoes found by the above procedure will be from other radiants, the echo lines of which cross the desired echo line at that point. In order to calculate an accurate flux, these echoes must be statistically removed, since there is no way to distinguish them individually. We therefore take an area on either side of the echo band of area equal to the band itself, and subtract the number of echoes in that area. This background subtraction will remove a number of echoes roughly equal to the background, and the resulting rate should give a reasonable flux.

3.8 Measurement of Decay Times

While very precise heights can be calculated with the interferometer, it is of interest to look at the heights as calculated from the decay of underdense echoes. In particular, the heights calculated from the decay times can be used to filter out any overdense echoes which may have passed the other tests in the echo detection software.

Underdense meteors decay exponentially after their peak. The decay time is the time for the echo to fall from the peak amplitude to 1/e of the peak. The amplitude follows a function of the form:

$$A = A_0 \exp\left(-\frac{t}{\tau}\right) \tag{3.13}$$

where τ is the decay time, A_0 is the peak amplitude, and t is the time since the peak. The graph of the natural logarithm of amplitude against time will be a straight line with slope -1/τ.

To improve the signal quality for the measurement, the in phase and quadrature signals on all receiver channels are coherently integrated. An autocorrelation is then performed on the data to further increase the quality; an autocorrelation is the same as a cross correlation (Equation 3.11) but involves multiplying the function by itself. The slope of the line of the natural log of amplitude against time is found with a standard linear regression, and if the error in the slope calculation is not too high the decay time is calculated from the result. The height of a meteor in kilometers can be roughly calculated from the decay time by finding the diffusion coefficient, D, from the decay time:

$$D = \frac{\lambda^2}{16\pi^2\tau}. \tag{3.14}$$

The height depends linearly on the ambipolar diffusion coefficient. The relation has been determined experimentally by several groups: recently it has been calculated by Jones & Jones (1990), using laboratory measurements and observations. They found:

$$\log D = 0.06h - 4.72. \tag{3.15}$$

where the height h is measured in kilometers.

Since the heights are measured much more accurately with the interferometer, the decay times are most useful in sorting out ambiguous echoes and eliminating the few overdense and transition echoes which pass the detection tests. Transition and

overdense echoes can pass the detection filters if the trains are suddenly twisted by the wind in such a way that they are no longer specular. While they pass the filter because they drop to the background level within three seconds in a fairly smooth fashion, the decay profile will be a poor exponential and the decay time will not necessarily correspond to the height at which the meteor occurs. A few transition echoes may still pass this test, but most will be eliminated. The decay times can also distinguish among ambiguous echoes. Although the decay time height may be in error by several kilometers, it may still able to distinguish which of two possible geometries is correct if there are more than one possible range or angle combination.

3.9 Summary

In order to gather useful observations for comparing echo amplitudes on more than one frequency, the radars must be similar and well calibrated. Power measurements were made close to the time of observations for all data used, and the power levels were monitored carefully for the duration of the observations. The receivers were calibrated close to the observing time as well. The echoes recorded by the radar will be largely underdense, with a few transition and overdense meteors. Statistical fluxes can be calculated from the data collected as long as care is taken to remove the background flux.

Chapter 4

Data Collection and Analysis

4.1 Amplitude Ratios

Once the data have been collected, they must be processed. Filters are applied to remove any echoes with suspect heights or amplitudes, and simultaneous echoes on two frequencies are found. The amplitude ratios of these meteors are calculated for analysis.

To investigate the initial trail radius as a function of height, we need to compare the amplitudes of underdense echoes recorded simultaneously on two frequencies. If the initial radius and physical characteristics of the trail are the same for all meteors at a given height, the points should fall on a curve such as those in Figure 4.1 in the amplitude ratio/height graph.

If there were no initial radius effect, the ratio of amplitudes at different frequencies would be simple to calculate. From Equation 2.16 and Equation 2.18, the voltage in the receiver for one system will be:

$$V_1 = 2R_i \left[2.5 \times 10^{-32} P_{T1} G_{T1} G_{R1} \left(\frac{\lambda_1}{R_0} \right)^3 q^2 \right]^{\frac{1}{2}}. \tag{4.1}$$

The amplitude will be (from Equation 2.17):

$$A_1 = c_1 3.2 \times 10^{-16} \left[P_{T1} G_{T1} G_{R1} \right]^{\frac{1}{2}} \left(\frac{\lambda_1}{R_0} \right)^{\frac{3}{2}} q. \tag{4.2}$$

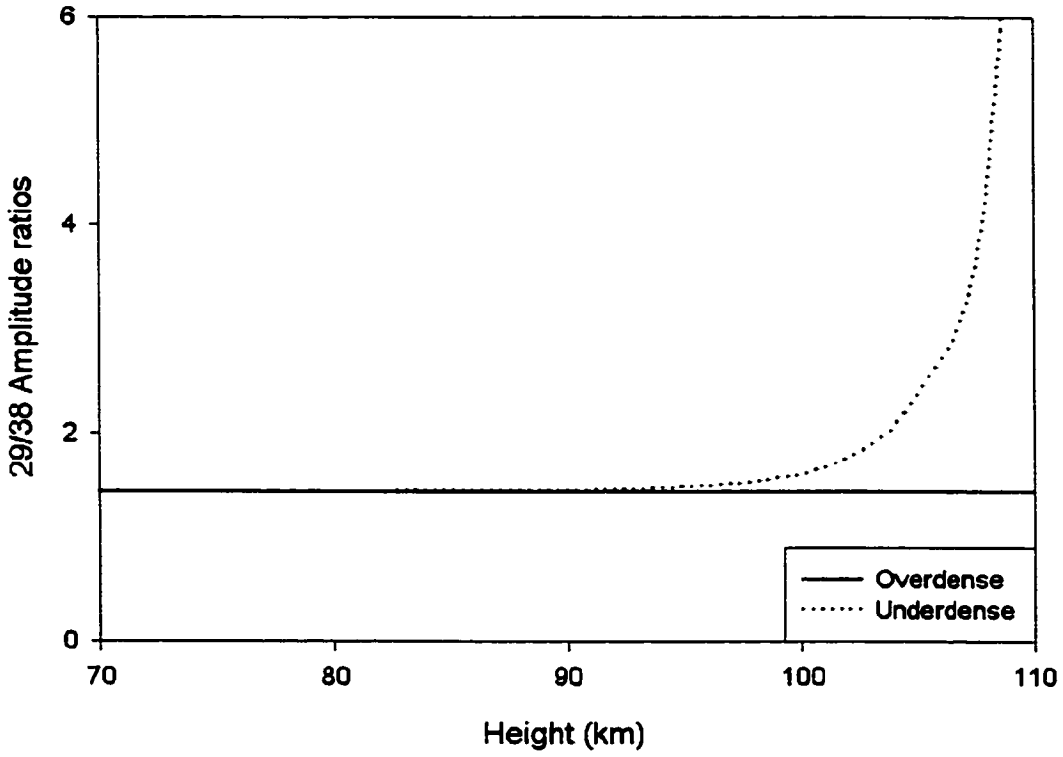

Figure 4.1: Amplitude ratios for 29 and 38 MHz for overdense echoes, and underdense with a simple model of initial trail radius

If the antennas are identical, the transmitter and receiver antenna gains G_T and G_R will be the same on both systems. The impedance R_i of both sets of cables is the same, and the range R_0 and electron line density q are the same since the same meteor is being observed. The amplitude ratio will therefore be:

$$\frac{A_1}{A_2} = \frac{c_1}{c_2}\left(\frac{P_{T1}}{P_{T2}}\right)^{\frac{1}{2}}\left(\frac{\lambda_1}{\lambda_2}\right)^{\frac{3}{2}}. \tag{4.3}$$

If the receiver calibration and the transmitted power are measured carefully and the echo strengths adjusted, the amplitude ratio will depend only on the ratio of the wavelengths of the systems raised to the power of 3/2.

Not all echoes are suitable for analysis. Transition and overdense echoes will be unaffected by initial radius and will have constant amplitude ratios as described above. The heights and amplitudes of underdense echoes must be accurately measured, or scatter will be introduced. For this reason, extra filters are added to remove meteors

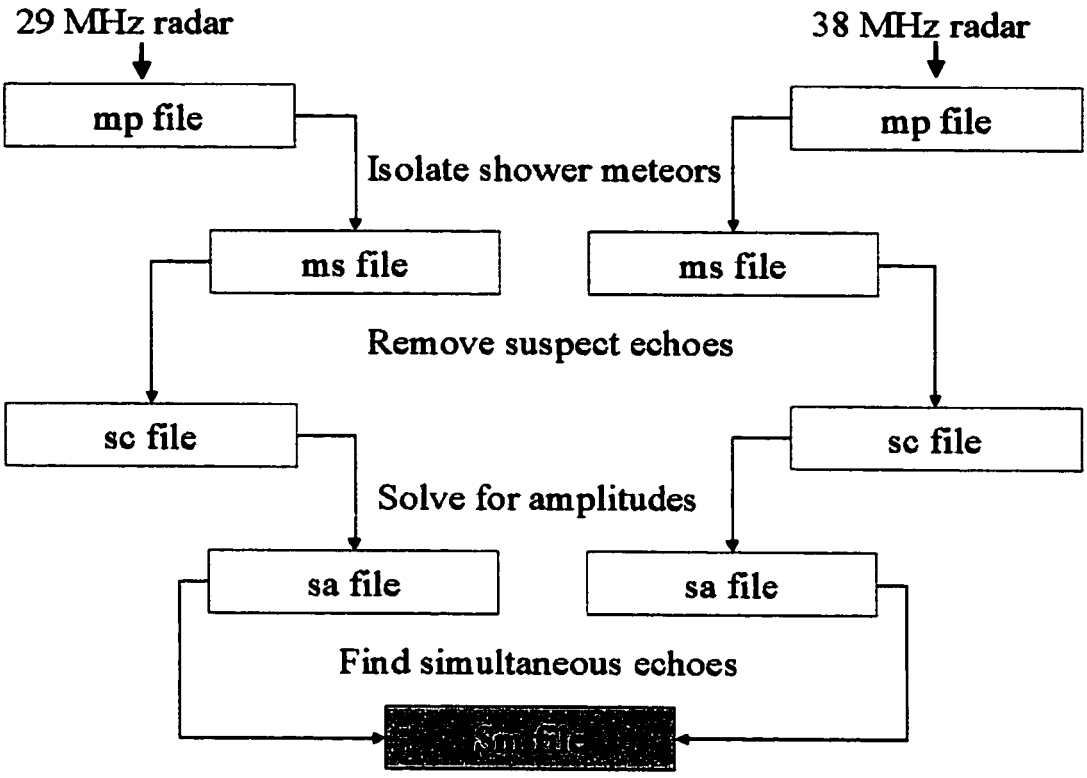

Figure 4.2: Data files at each stage of processing

which are potentially overdense or transition, and which may have significant height and amplitude errors. The amplitude of each echo is calculated by sampling the returned pulse several times and fitting the known shape of the pulse. This will eliminate errors due to sampling away from the peak of the pulse. (Figure 4.2)

Because the initial radius attenuation may depend on fragmentation and therefore the meteoroid structure, and because it may depend on velocity, the analysis was initially done for Geminid meteors only. This will provide a test of the method on the simplest case, where all meteors have identical velocities and similar compositions. The Geminids are one of the most active showers on the radar, since they are lower in velocity than many other streams and penetrate farther into the atmosphere. They may, however, differ significantly from other, cometary meteoroids since their parent object, 3200 Phaethon, appears to be an asteroid. Jacchia, Verniani & Briggs (1965), however, found that although Geminids were denser than average meteors, they had the same fragmentation index, so while our results will need to be scaled in height,

the fragmentation factor derived from them should be universally applicable. The fact that we have ignored the effects of velocity on initial radius may also affect the accuracy of our results when applied to sporadic meteors, but it offers a valuable test of the new method of calculating the fraction of echoes unobserved due to initial radius which can be applied specifically to other meteors afterwards.

4.2 Collected Data

The data files from the radar contain a list of all meteor echoes which passed the detection tests described in the previous chapter. The files produced by the radar have names of the form mpYYYYMMDD.tindalx.mpd, the x being 1 for the 17 MHz system, 2 for 29 and 3 for 38 MHz. These files contain headers listing information about the radar's location, antenna coordinates, and other information: these headers were removed prior to analysis and the resulting files, called mp files, contain only a single header line and the data for each meteor. They have names of the form mpYYMMDD.dat, where only the last two digits of the year are used. For each meteor, the date, time, range, height, positional angles, the amplitude and decay time are stored, among other data. If more than one range or set of angles was possible, the meteor was labeled ambiguous, and all possible geometries kept: a number in the file listed the number of possible geometries. When long pulses are used, a single meteor may have several records associated with it, each differing in range by one sampling interval and having a different amplitude. Data files for each meteor were also saved during shower observations and could be consulted later: these binary files contain the in-phase and quadrature amplitude data for each antenna. These files had names of the form MEYYYYMMDD.xxxxx, and the five-character extension was recorded in the mpd file.

Table 4.1 is an example of an mp file, for December 13, 2001 from the 38 MHz system.

Table 4.1: Sample mp file, 38 MHz system, for December 13, 2001. The columns are date, time of echo, raw data file extension, range, height, radial velocity, error in radial velocity, azimuth (degrees east of north), zenith angle, ambiguity, estimated error in phase, antenna pair, reference receiver, maximum amplitude, decay time, and estimated meteor velocity (-9.9 if no velocity calculation was possible).

Date	Time	File	Rge	Ht	Vrad	delVr	Theta	Phi0	Ambig	Delphase	ant pair	IREX	amax	Tau	vmet
01/12/13	0:01:39.7	00000	154.0	86.8	14.91	0.52	56.3	140.6	1	7.8	14	1	2030.0	0.116	-9.990
01/12/13	0:02:25.2	00001	115.0	95.7	4.62	1.60	34.0	143.2	1	13.3	35	1	2475.0	0.042	-9.990
01/12/13	0:02:25.2	00002	112.0	93.4	6.37	1.74	33.8	142.9	1	10.0	35	1	2650.0	0.043	-9.990
01/12/13	0:03:11.1	00003	130.0	100.8	-55.29	0.16	39.5	191.7	1	3.4	14	1	8495.0	0.028	-9.990
01/12/13	0:03:11.1	00004	136.0	105.4	-55.38	0.10	39.6	191.7	1	2.5	13	1	9328.0	0.029	-9.990
01/12/13	0:03:11.1	00005	133.0	103.2	-55.28	0.17	39.5	191.6	1	2.8	14	1	12411.0	0.028	-9.990
01/12/13	0:04:31.6	00006	112.0	90.5	-19.65	0.97	36.4	181.5	1	5.0	13	1	2510.0	0.068	-9.990
01/12/13	0:04:31.6	00008	109.0	88.1	-18.78	1.35	36.4	181.6	1	9.7	45	1	2424.0	0.066	-9.990
01/12/13	0:04:44.0	00009	118.0	88.7	-19.10	1.94	41.6	291.0	1	16.4	45	1	1754.0	0.090	-9.990
01/12/13	0:04:44.0	0000A	115.0	86.7	-19.34	0.88	41.4	291.2	1	6.3	14	1	2596.0	0.109	-9.990
01/12/13	0:04:44.0	0000B	112.0	84.4	-20.48	1.06	41.4	291.1	1	5.5	45	1	2020.0	0.107	-9.990
01/12/13	0:05:22.4	0000C	136.0	96.9	-18.21	0.31	45.0	294.3	1	5.1	23	1	5853.0	0.027	-9.990
01/12/13	0:05:22.4	0000D	133.0	94.8	-18.96	0.23	45.0	294.3	1	5.1	45	1	7194.0	0.027	-9.990
01/12/13	0:05:22.4	0000E	130.0	92.7	-18.03	0.49	44.9	294.4	1	5.9	35	1	4620.0	0.027	-9.990
01/12/13	0:06:42.7	0000F	109.0	89.9	-7.67	4.29	34.7	222.2	1	14.9	25	1	1663.0	0.024	-9.990
01/12/13	0:07:15.7	0000H	97.0	88.5	-4.15	5.39	24.3	154.6	1	33.4	24	1	1144.0	0.022	-9.990
01/12/13	0:08:25.8	0000I	97.0	91.1	-13.87	1.12	20.3	166.7	1	7.4	13	1	2439.0	0.090	-9.990
01/12/13	0:08:25.8	0000J	94.0	88.2	-15.31	0.88	20.3	167.1	1	7.6	13	1	2843.0	0.086	-9.990
01/12/13	0:10:05.0	0000W	91.0	88.9	-8.37	1.33	12.5	213.9	1	7.6	14	1	2115.0	0.073	-9.990
01/12/13	0:10:05.0	0000X	88.0	85.8	-8.44	2.25	12.8	213.0	1	10.0	15	1	1742.0	0.067	-9.990
01/12/13	0:10:05.0	0000Y	94.0	91.8	-6.17	2.44	12.5	212.7	1	15.5	45	1	1480.0	0.067	-9.990
01/12/13	0:10:38.4	0000Z	121.0	92.0	4.27	0.04	40.9	205.0	1	2.5	24	1	13401.0	0.095	-9.990
01/12/13	0:10:38.3	00010	124.0	94.3	4.24	0.04	40.9	205.0	1	2.1	23	1	13317.0	0.093	-9.990
01/12/13	0:10:38.4	00011	127.0	96.8	4.18	0.30	40.7	204.9	1	6.1	14	1	3758.0	0.101	-9.990
01/12/13	0:10:38.3	00012	118.0	89.5	4.30	0.29	41.1	205.0	1	1.7	13	1	3951.0	0.093	-9.990
01/12/13	0:11:30.5	00013	91.0	88.8	-0.25	0.08	12.7	206.9	1	4.8	45	1	8372.0	0.067	-9.990
01/12/13	0:11:30.5	00014	88.0	85.8	-0.54	0.06	12.9	206.6	1	2.6	45	1	14314.0	0.072	-9.990
01/12/13	0:11:30.5	00015	85.0	82.9	-0.65	0.06	12.9	206.6	1	0.5	45	1	11574.0	0.075	-9.990
01/12/13	0:11:31.1	00017	118.0	90.7	-10.58	0.81	40.1	289.0	1	6.7	23	1	2015.0	0.132	-9.990

4.3 Amplitude Measurements

The first task in finding accurate amplitudes is to find the shape of the pulse. This can be done by increasing the length of the pulse and sampling more frequently; a curve can then be fit to the resulting shape. The returned shape will differ slightly from the shape given to the transmitter because of the finite bandwidth, so it is necessary to measure the returned pulse rather than the shape produced in the transmitter.

Shaped pulses, which are rectangular with tapered edges, were chosen since they produced a function which was easy to fit. To determine the shape, ten kilometer pulses were transmitted and sampled every 1.5 kilometers. The highest amplitude meteors (with the maximum number of points) were chosen on each frequency and curve fits done in TableCurve 2D v3. This package fits over 3000 functions to the given points, calculates the error, and ranks them. The function which best described the shape of the returned pulse was an asymmetric double sigmoidal curve, defined as:

$$y = a + \left[\frac{b}{1+\exp\left(-\left(x-c+\frac{d}{2}\right)/e\right)}\right]\left[1-\frac{1}{1+\exp\left(-\left(x-c-\frac{d}{2}\right)/f\right)}\right]. \quad (4.4)$$

Here, y is the amplitude and x is the range bin. The coefficients are a, b, c, d, e and f. The vertical offset is a, and can be set to zero since all echoes can be assumed to start at the zero level. b represents the peak of the curve, and corresponds to the maximum amplitude of the meteor. The horizontal distance to the peak of the curve is c, and will be the range at which the maximum amplitude occurred. The width of the curve is d, and is known for any observing run. e and f are measures of the steepness of the curve's rise and fall, respectively. The quantity e or f scales with the width of the pulse, and by calculating e/d and f/d from the curve fit one can find the appropriate values for any pulse width.

Once a general pulse shape is known, the amplitude and range to maximum of any echo with several samples can be calculated. The only two unknowns in Equation 4.4 will be b and c, corresponding to the amplitude and range of the peak. The curve fit is done numerically rather than analytically, so each parameter is varied and the

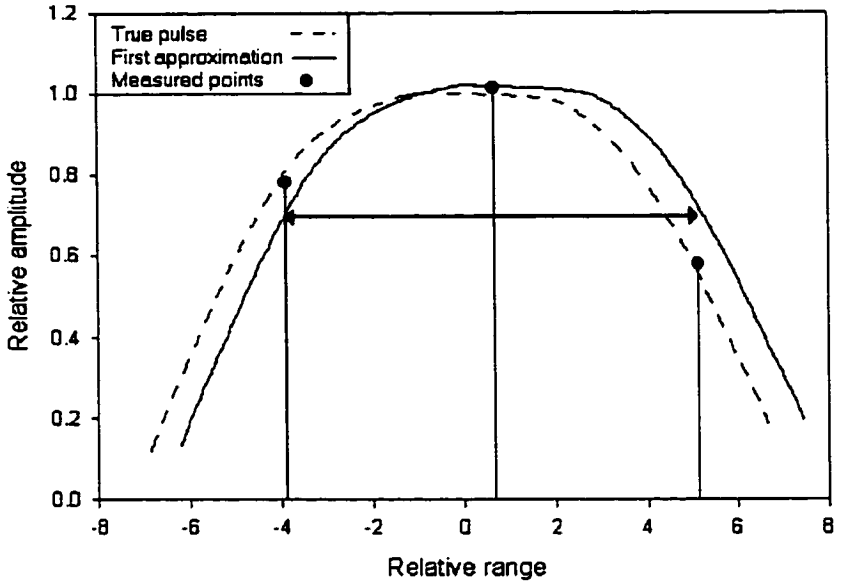

Figure 4.3: First approximation of pulse shape, varied to find the best range to the centre.

one with the least error is chosen. Since the maximum amplitude and corresponding range must be in the center of the curve, good starting approximations can be found. The largest amplitude measurement is first used as the maximum amplitude, and the range varied from the range of the largest measured amplitude to half the pulse width on either side. (Figure 4.3) Once the best range offset is found, this is used as c and the amplitude value is stepped to 10% above and below the measured maximum to find fit with the least error.

The pulse length and sampling interval cannot be altered arbitrarily. The duty cycle must not be significantly increased, to avoid overloading the transmitter. This means that if the pulse length is increased, the PRF must be dropped so that fewer pulses are sent each second. The sampling interval must be at least 1.5 km, due to software constraints. The number of data points sampled must not exceed the capacity of the data bus: a maximum of 80 gates is allowed per pulse. The range to be sampled after each pulse is the aliasing distance, or the distance a pulse can travel and return to the radar from one pulse to the next. The time available is 1/PRF, so the lower the PRF, the longer the aliasing distance, and the more points must be

Table 4.2: Radar Data Collecting Modes

Mode	Length of Pulse(km)	PRF (Hz)	Alias Range(km)	Resolution (km)	Range Sampled(km)	Gates Used
Standard	2	2144	70	2	60	30
10 km	10	536	280	1.5	120	80
8 km	8	536	280	3	240	80
4km	4	1072	140	1.5	120	80

sampled to completely cover it. If the PRF is too low and the sampling rate too high, there will be a blank space where echoes cannot be detected. A blank space of more than twice the pulse length is left in any mode to ensure that the receivers do not sample when the transmitter is on, to avoid saturating them. For example, in the standard operating mode, the PRF is 2144 pulses per second. A pulse can travel (at the speed of light) 140 km in the 13.3 microseconds between pulses, so the radar can receive returns from anything within 70km. If the object is more distant, the return will be received after the following pulse. The region from 0 to 60 km is sampled, leaving a 10 km blank for the transmitted pulse.

The 10 km pulse mode was used only for determining the shape of the pulses: since the range between 120 and 280 km could not be sampled in this mode, it was not useful for data collection. Both the 8 km and 4 km pulse modes gave fairly complete coverage of range.

The lowest sampling interval easily achieved was 1.5 km for a 4 km pulse, or 3 km for an 8 km pulse (Table 4.2). The longer pulses were needed for a velocity experiment being run during the 2001 Geminids. A simulation routine was written which generated amplitude measurements spaced 1.5 km apart on a 4 km pulse, with randomly generated noise added to each amplitude sample. It was found that for echoes which were sampled at least three times, amplitudes could be measured to better than 2%, with an average of 0.6% for echoes with signal-to-noise ratios of at least 10 dB. For the faintest echoes, the errors were better than 5% for echoes down to 5dB. By contrast, if the maximum of the measured amplitudes was taken to be the true one, the errors were an average of 1.3% with individual errors greater than 3% for echoes with a SNR greater than 10; and more than 10% for the faintest echoes.

4.4 Echo Selection

Since only Geminid meteors were to be used in the preliminary analysis, the first step in the data analysis was to sort out possible shower meteors. While there is no way to uniquely identify Geminid meteors with the current system design, on the days around the Geminid maximum the stream meteors will outnumber sporadics on the echo line by nearly an order of magnitude.

Shower meteors were isolated using a C++ program. It generated a ground based unit vector to the radiant at the time of each meteor, took the dot product with a unit vector pointing to the meteor, and if the result was greater than $\cos(87°)$ the meteor was accepted. Meteors passing this test were written to a new data file.

Several extra filters were applied to the data to remove unsuitable echoes, including all echoes which might be overdense or transition, and those which had suspect amplitudes or heights.

The first filter removed all echoes with a zenith angle more than 68°. Echoes close to the horizon have a number of problems. They have potentially many range ambiguities, since they pass through the region in the atmosphere where meteors are seen (75 to 110 km) at a shallow angle. Any unevenness in the ground will cause uncertainty in the gain pattern in that region, resulting in more uncertain amplitudes. The height errors will also be greater since the ranges are larger and small errors in the elevation angle will result in large errors in height. The echoes removed by this filter will not bias the sample, since the constraint is geometric and is averaged out over the course of a day.

The echoes were then tested to see if the measured decay time corresponded roughly to the height, in a manner similar to that used by Hocking *et al* (2001). The ambipolar diffusion coefficient was calculated from the decay time, and a height determined from the diffusion coefficient. If this height was within 10 km of the measured height, the echo was accepted: this is within the range of error on the decay time and in the height. If it was more than 10 km from the measured height, the echo was rejected. For ambiguous echoes, the height was calculated from the

decay time, and if only one of the possible echo geometries had a height which was close to it, the echo was accepted. If none of the heights matched or if more than one were possible, the set was rejected.

All echoes occurring at the same time and place in adjacent range bins were kept and used in the fitting procedure above. The amplitude fits were done with a third C++ program, and the echoes stored in another data file for use in the last step.

4.5 Simultaneous Echoes

The final analysis task is to find the simultaneous echoes on pairs of frequencies. While the specular geometry is the same for all three systems, echoes recorded on one system are not necessarily recorded on the others. The height ceilings on the three systems due to initial radius are very different: an echo seen on 17 MHz may be too high for detection on 38 MHz. Also, an echo which appears overdense at 17 MHz and is therefore rejected by the analysis software may be underdense at shorter wavelengths. Because of these effects, very few of the meteors will be seen simultaneously on all three systems. However, by finding the simultaneous echoes on 29 and 38 MHz and on 17 and 29 MHz, significant numbers can be collected. Since terrestrial interference on 17 MHz prevents the detection of meteors for more than half of each day, the majority of the simultaneous echoes are found on 29 and 38 MHz.

Simultaneous echoes were found with a final C++ program. Each system has a GPS receiver which recorded the time of each meteor detection. Finding meteors occurring at the same time, at the same range (within the error margin), elevation and azimuth, one will virtually guarantee that the observations are from the same meteor trail. The power and receiver calibrations for each radar were used with equation 4.3 to find corrected amplitude ratios.

Table 4.3: Numbers of underdense Geminid meteors collected on each radar frequency and of simultaneous echoes on pairs of frequencies

Year	Day	17 MHz	29 MHz	38 MHz	17/29	29/38
2001	10	143	130	105	3	50
2001	11	141	303	172	36	75
2001	12	176	596	249	62	136
2001	13	41	658	297	13	156

4.6 Results

Data were collected during the 2001 Geminid shower in December and the 2002 Quadrantid shower in January. Power levels were measured on all three systems on December 10. Reception at 17 MHz suffered from heavy interference on all the shower days, but 29 and 38 MHz operated smoothly from December 11 to December 14, and all three operated on January 3 and 4. Because of a simultaneous experiment, 8 km pulses were used during the 2001-2002 campaign. Power levels were measured before observations began and monitored on all three frequencies throughout. It had been found that the power levels from the transmitters occasionally fluctuate due to hardware failure, but the power levels stayed constant over the five days of the shower. The 17 MHz system suffered from interference on December 13, but had approximately 10 hours with low noise on the other campaign days. The number of echoes recorded on each system was reduced by each filter applied, and the final number of Geminids passing all the tests on each date is given in Table 4.3. The power levels on each system and receiver calibrations are given in Table 4.4.

The results for all days of data during the 2001 campaign are shown in Figure 4.4 and Figure 4.5. The expected ratio in the absence of initial radius effects is shown in each plot, using the power measurements and receiver calibrations for each system.

The reason for the large uncertainty in initial radius calculations is apparent from these plots. Particularly on the 17/29 MHz ratios, there is a very large scatter in

Table 4.4: Power levels and receiver calibrations on radar systems during the 2001 Geminids and 2002 Quadrantids)

	17 MHz	29 MHz	38 MHz
Power (W)	6530	6180	4680
Receiver calibration (Volts / Amplitude Unit)	13.27×10^{-10}	12.82×10^{-10}	12.61×10^{-10}

the data which is not predicted by the theory. It is plain from these results that the simple model of initial radius is inadequate, and much more work needs to be done to quantify the effects.

In addition to the large scatter on both pairs of systems, there is another population of echoes which shows no height dependence in the amplitude ratios. This population is more noticeable in the 2000 Geminid data, which was not used since power measurements were not taken during the shower and the antennas had not been calibrated (Figure 4.6). The data appears to follow two separate trends: one which shows an increase in amplitude ratio around 95 km, and the other which is constant and also shows significant scatter. The latter population is explained by overdense and transition echoes which slipped through the analysis routines, and provides a baseline to ensure the power measurements and receiver calibrations are correct.

Visual examination of some of the echoes in the suspected overdense population confirmed that most of them had overdense characteristics: in particular most of them had a constant amplitude for a brief period after their peak, before the amplitude started to decline. To remove these echoes before any analysis was done, another filter was applied. The time for the echo to fall to 95% of its maximum amplitude was determined from the raw data file for each meteor. This was compared to the time expected, given the expected decay time of the meteor, and if it was more than five times as big as the expected time the echo was classified overdense (Figures 4.7, 4.8).

When these echoes were removed, there were very few echoes with small amplitude

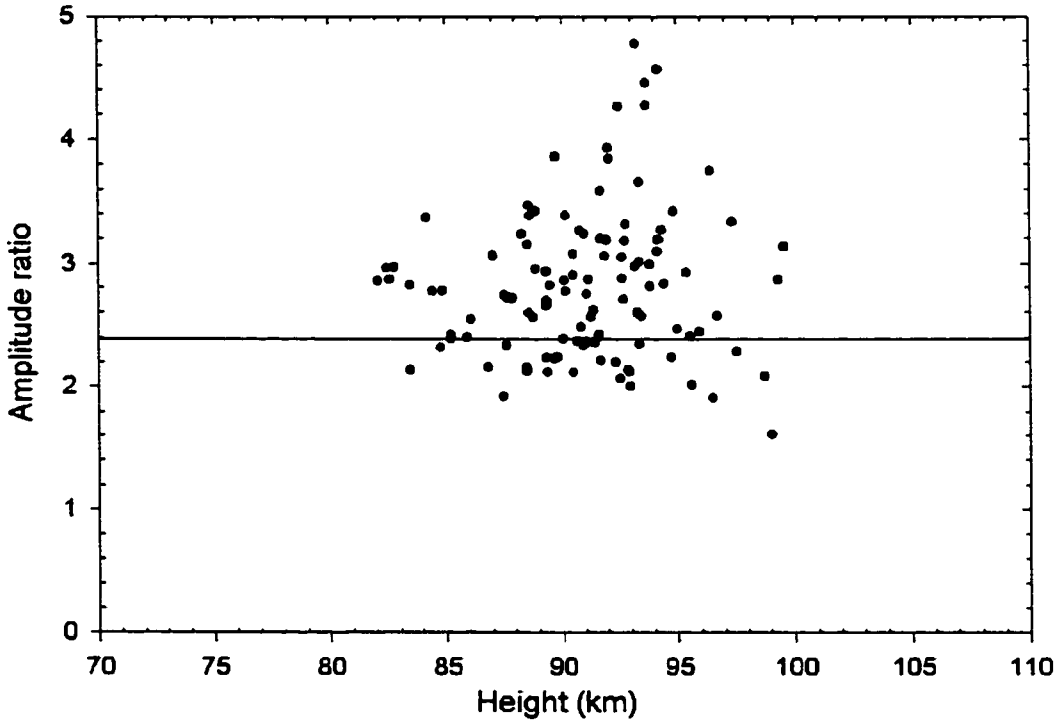

Figure 4.4: Observed amplitude ratios on 17 and 29 MHz for the 2001 Geminids against height. The horizontal line represents the expected ratio for an infinitely thin trail.

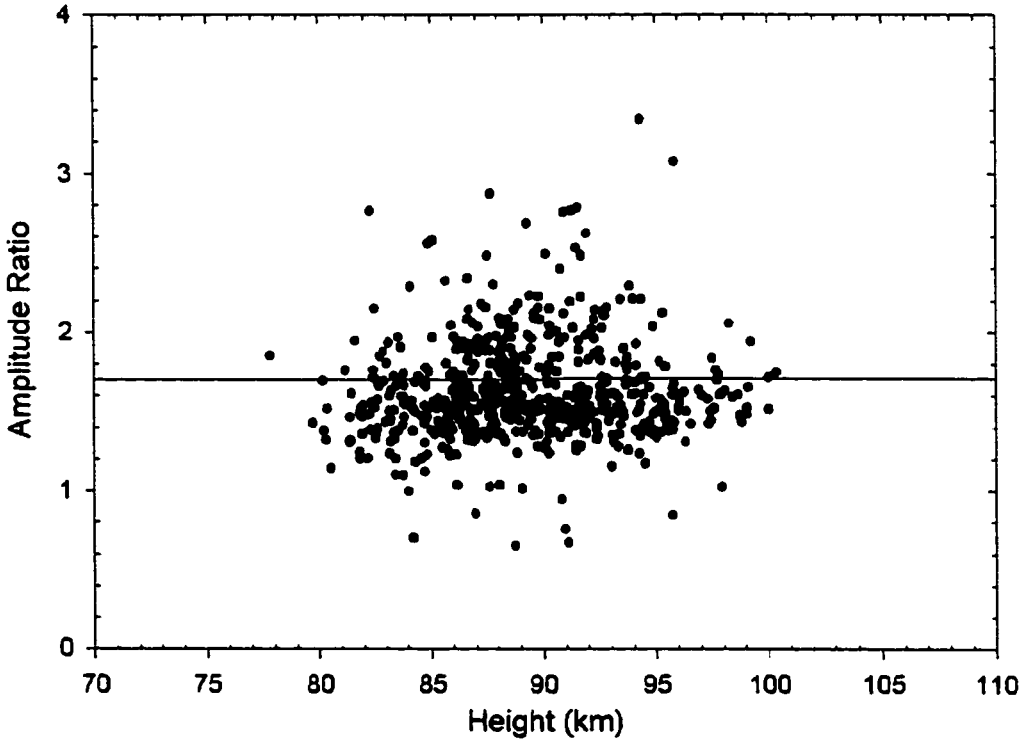

Figure 4.5: Observed amplitude ratios on 29 and 38 MHz for the 2001 Geminids against height. The horizontal line represents the expected ratio for an infinitely thin trail.

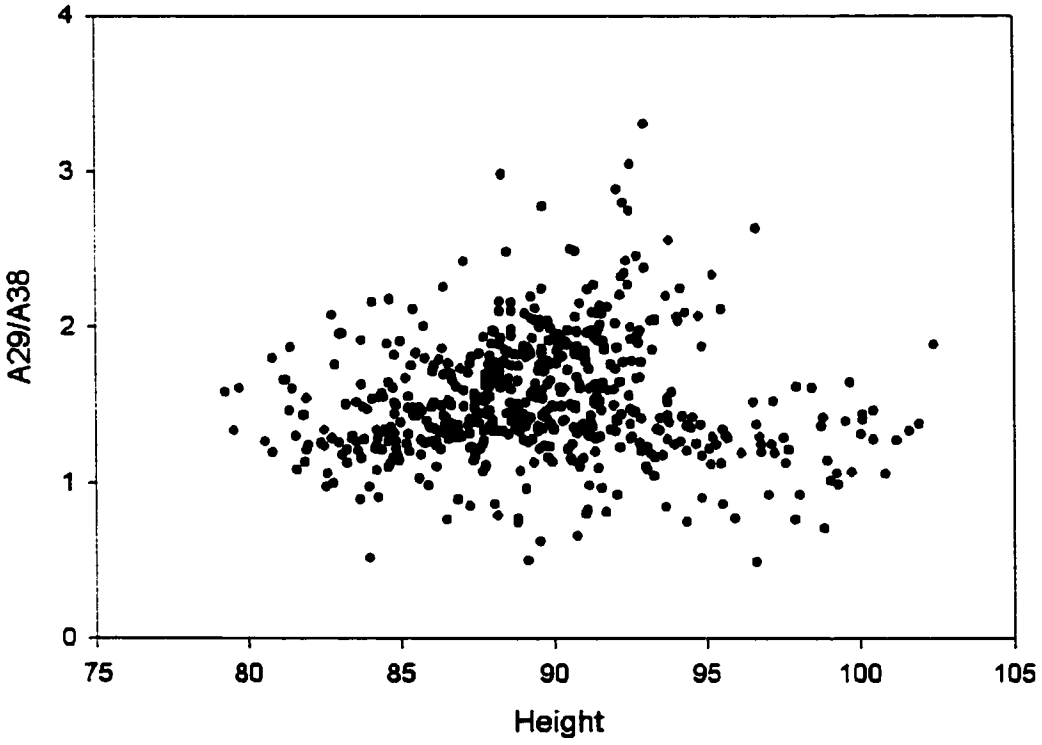

Figure 4.6: Observed amplitude ratios on 29 and 38 MHz for the 2000 Geminids against height.

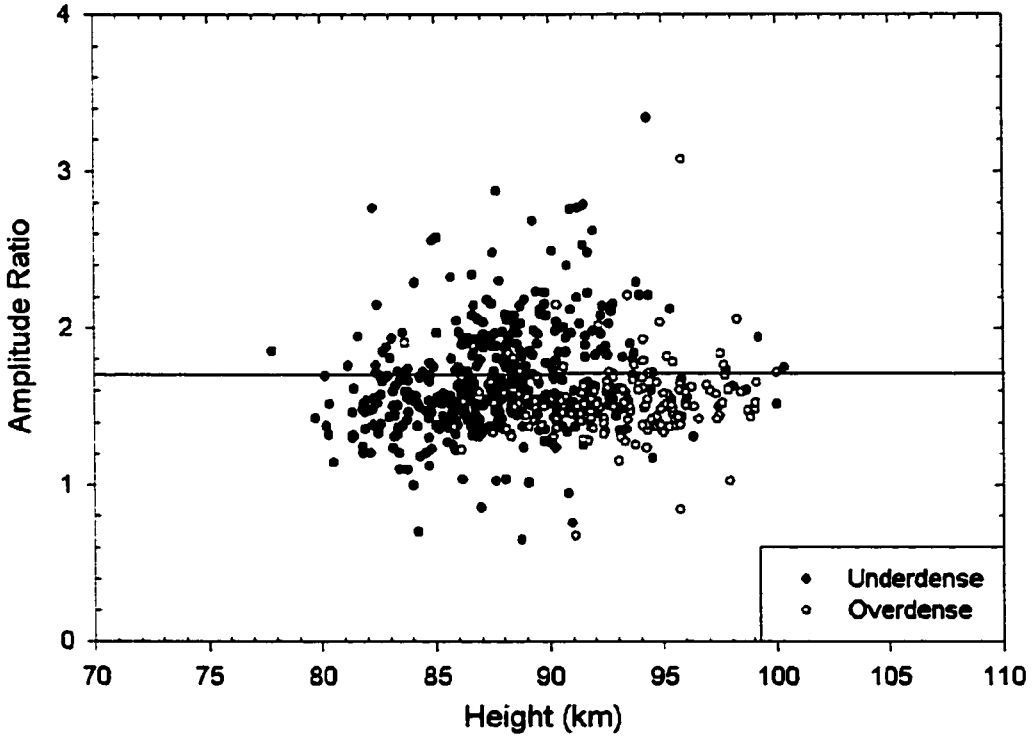

Figure 4.7: Amplitude ratios on 29 and 38 MHz with echoes identified as overdense represented by the open circles

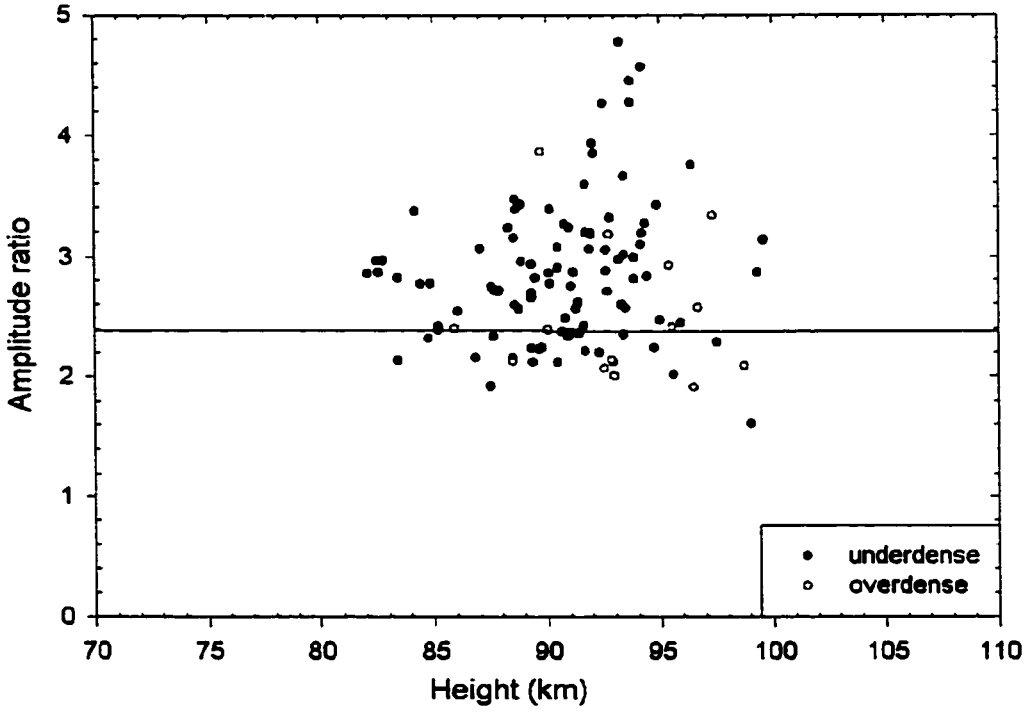

Figure 4.8: Amplitude ratios on 17 and 29 MHz with echoes identified as overdense represented by the open circles

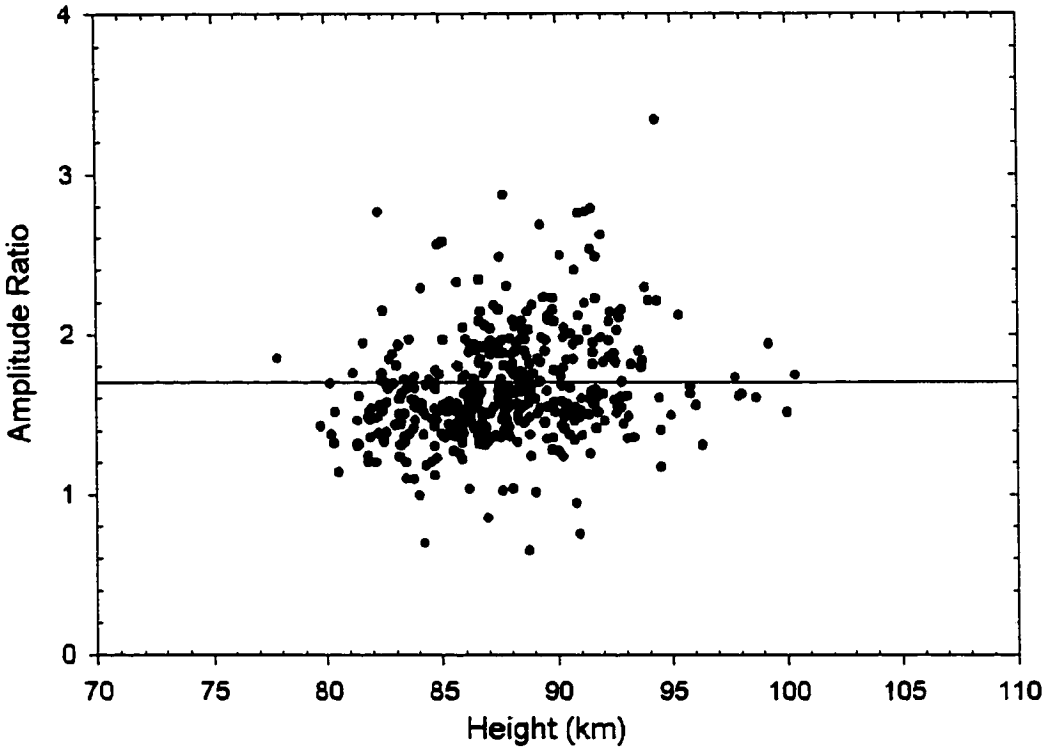

Figure 4.9: Observed amplitude ratios on 29 and 38 MHz with overdense echoes removed

ratios over 95 km (Figure 4.9). Very few overdense echoes were identified below 90 km: the overdense test is not as discriminating at lower heights since the expected decay time is longer. These echoes will cause less error in the solution than those at greater heights, however, since the difference in amplitude ratio between underdense and overdense echoes is small at low heights.

The cause of the scatter is more difficult to identify and it will be investigated in the following chapter. The cause of the scatter must be different on different wavelengths, in order to change the amplitude ratio, and different for different meteors to produce scatter. It cannot be caused, for example, by poor absolute power measurements, since that would produce a shift up or down in the diagram but would not affect the scatter. The relative powers were monitored on each frequency through the experiment, so no fluctuations took place during the measurements. Since the numbers of simultaneous echoes on 17 and 29 MHz were low, these data were used as

a check, and the model was developed using the ratios on 29 and 38 MHz.

The scatter in amplitude ratios explains the widely varying results found in other radar studies of initial radius: the function describing initial radius as a function of height will vary depending on how the average of amplitude ratio at a particular height was taken.

Chapter 5

Computer Simulation of Radar Echoes

5.1 Determination of Attenuation of Radar Echoes

Given the results of the multifrequency investigations, it is apparently impractical to try to explain the results assuming each meteor trail is generated by a single particle. There are many small effects which need to be considered, and the only practical way to do this is to simulate the data.

For this purpose, a simulation program was written which generated meteors based on known characteristics of height and velocity distributions. The received power was then calculated for each echo for three radars at 17.45, 29.85 and 38.15 MHz. The basic model used only the ordinary radar meteor equations; for the newer model, other components, including Faraday rotation, initial radius effects and fragmentation were added.

For generating random numbers, the ran0 routine from Numerical Recipes in C (Press *et al*, 1992) was used. This routine is superior to standard random number generators in most compiler packages because it can generate a large number of random values without repetition.

5.2 Basic Simulation

5.2.1 Generating echoes

Meteor trails were generated with a height h, electron line density q, azimuth ϕ and zenith angle θ. The heights were generated according to the height distribution of Jacchia, Verniani & Briggs (1965) for Geminids adjusted for the higher radar sensitivity, as a Gaussian centered on 98 km with a 7 km rms deviation. The azimuthal angle was chosen randomly between 0 and 360°. The elevation angle was calculated by first finding the maximum horizontal range of an echo at the generated height. Since meteors with elevation angles less than 20° were rejected, an echo with an angle less than this would not be observed. Otherwise, echoes should be randomly distributed in horizontal distance, so a random horizontal range was chosen. The elevation angle was then calculated with simple geometrical considerations.

The range to the echo was calculated using curved-Earth geometry, since the correction to flat Earth was found to be significant. The formula is:

$$R_0 = R_E \cos(\pi - \theta) + \left(R_E^2 \cos^2(\pi - \theta) + h^2 + 2hR_E\right)^{1/2} \tag{5.1}$$

where all variables are defined above.

The time delay between echoes was random, and the average delay between echoes was varied to match the observed variation in echo rates. The echo rate was highest at 0600 local time and at a minimum at 1800 local time. This variation in rates ensured that the Faraday rotation effects will apply to the appropriate fraction of meteors.

5.2.2 Sampling the generated meteors

The power at the receiver for each echo was then calculated. The gain patterns for the transmitting and receiving antennas on each system were read in from a text file, and the gains at the elevation and azimuth of the trail calculated. The transmitter power for each system on the date being simulated was read from a file along with the receiver calibration. It was necessary to simulate the date on which the data

was collected so that the properties of the ionosphere were correctly described by the International Reference Ionosphere. The received power was then determined using equation 2.16.

Before calculating the amplitude, the echo was tested to see if it exceeded the noise power on the system by 5 dB. The noise power for each system was calculated using the measured daily minimum and maximum noise levels and assuming that it varied sinusoidally with the elevation of Cassiopeia A (see Chapter 3).

If the echo passed this test, the amplitude was calculated using the receiver calibration and equation 2.17. The decay time was calculated using the relation of equations 3.14 and 3.15; this was done so that the generated data would pass the decay time test in the analysis routines. To simulate the effects of shaped pulse sampling, which could introduce different errors on the different frequencies, the return was spread over many range bins using the ADS fit of Chapter 4. At each range bin, the amplitude was calculated, and noise was added to each sample. If the amplitude exceeded the threshold required for detection, it was sampled and the echo was recorded in a file identical to the mp files produced with the radar. Because of this, only echoes which were 5 dB above noise at three range bins were kept. For the values in the mp file which are not used in our analysis, such as angular speed and phase error, random values were entered as placeholders so the program which read in meteor records could be used without alteration.

5.2.3 Results of basic simulation

As expected, with no initial radius effect the amplitude ratios were independent of height. Noise in the amplitudes and the need to fit a curve to find the maximum amplitude produced a small amount of scatter, but not nearly as large as that which was observed (Figure 5.1).

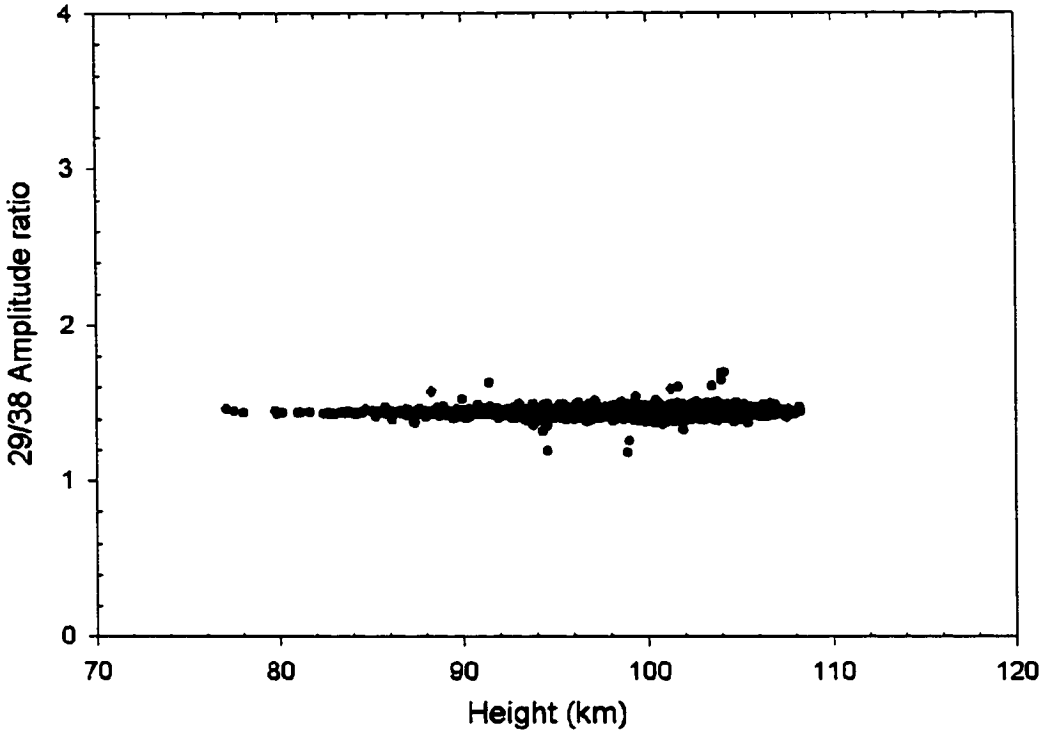

Figure 5.1: Amplitude ratios from simulation with only basic parameters

5.3 Faraday Rotation

One possible cause of scatter in meteor amplitudes is Faraday rotation, which affects electromagnetic waves travelling though a plasma in the presence of a magnetic field (see e.g. Elford & Taylor (1997)). During the day, the E-region and D-region of the ionosphere have an electron density of 3×10^9 electrons/m^3, and extend from approximately 90 to 150 km altitude. As the EM wave passes through this region, its polarization vector is rotated; on the return it is rotated by the same amount in the same direction. If it returns to the polarized antenna with a rotation of $\pi/2$, it will be invisible to the radar, and if the rotation is more or less than this the echo will be attenuated. This effect will be different at different times of day and at different areas in the sky, and it is frequency dependent.

The equation for the angle of Faraday rotation Ω is (Elford & Taylor, 1997):

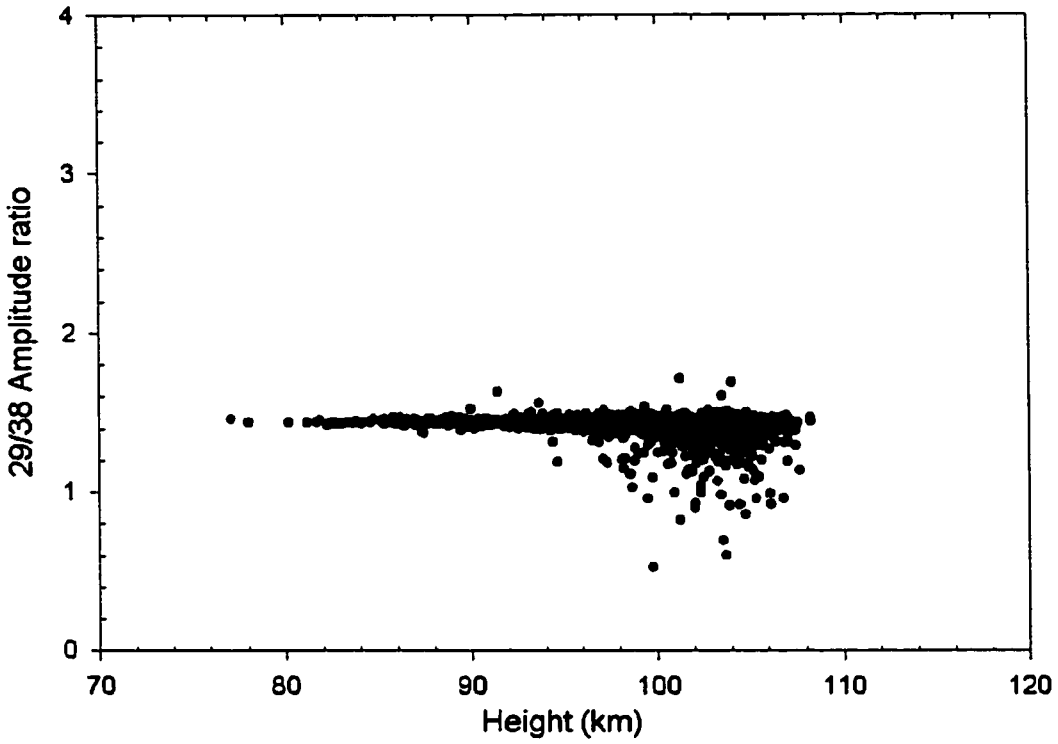

Figure 5.2: Amplitude ratios from simulation with basic parameters and Faraday rotation

$$\Omega = 2.36 \times 10^4 \frac{\vec{p} \cdot \vec{B}}{f^2} \int N_e ds \tag{5.2}$$

where $\vec{p}$ is a unit vector in the direction of travel of the EM wave, $\vec{B}$ is the Earth's magnetic field at the appropriate latitude and longitude, f is the frequency of the wave, N_e is the electron density and ds is a distance along the path of the radio wave.

The International Reference Ionosphere model (Bilitza, 2001) was used to find the density of electrons in the region from 60 to 130 km. The integral in equation 5.2 was evaluated numerically. The echo amplitude was attenuated as $\cos \Omega$.

Faraday rotation only affects echoes where the echo direction is close to the magnetic field direction, is more important on lower frequency systems and only while the E-region has a high electron density, during the day. It hardly affects 38 MHz at all, and 29 MHz is only affected at the time of maximum ionization. The effect is very significant on 17 MHz.

The result is more scatter below the line of constant amplitude ratio: since Faraday rotation affects 29 more than 38 for every echo, it will tend to produce amplitude ratios below this line (Figure 5.2).

5.4 Initial Trail Radius

Two functions are important for calculating the attenuation due to initial radius: the initial radius itself as a function of height, and the attenuated amplitude as a function of initial radius and wavelength. Based on the collisional models of trail formation presented in Chapter 2, we expect initial radius to be proportional to the mean free path in the atmosphere. We can therefore choose a number of mean free paths as the initial radius. The attenuated amplitude of the echo as a function of initial radius and wavelength is the Fourier-Bessel transform of the electron density function. Since the form of this function is unknown, a Gaussian is usually assumed, but the Jones model (Jones, 1995) predicts a distribution more like an exponential.

The initial radius was calculated for each generated meteor, based on its height and the height dependence entered. The attenuated amplitude was then determined from the Fourier-Bessel transform of the radial electron density function.

The point at which the amplitude ratios start to increase rapidly with height is governed by the number of mean free paths in the initial radius. The scatter is much larger than before: this is mainly due to errors in heights from the compounded errors in elevation and range. The scatter is still not as large as the observed data, particularly at lower heights. The Gaussian electron density distribution (Figure 5.3) produced a sharper rise in the ratio of the amplitudes with height than the exponential (Figure 5.4).

5.5 Finite Velocity Effect

The attenuation due to initial radius will be increased by the fact that the meteor takes a finite time to cross the first Fresnel zone. When the meteor reaches maximum

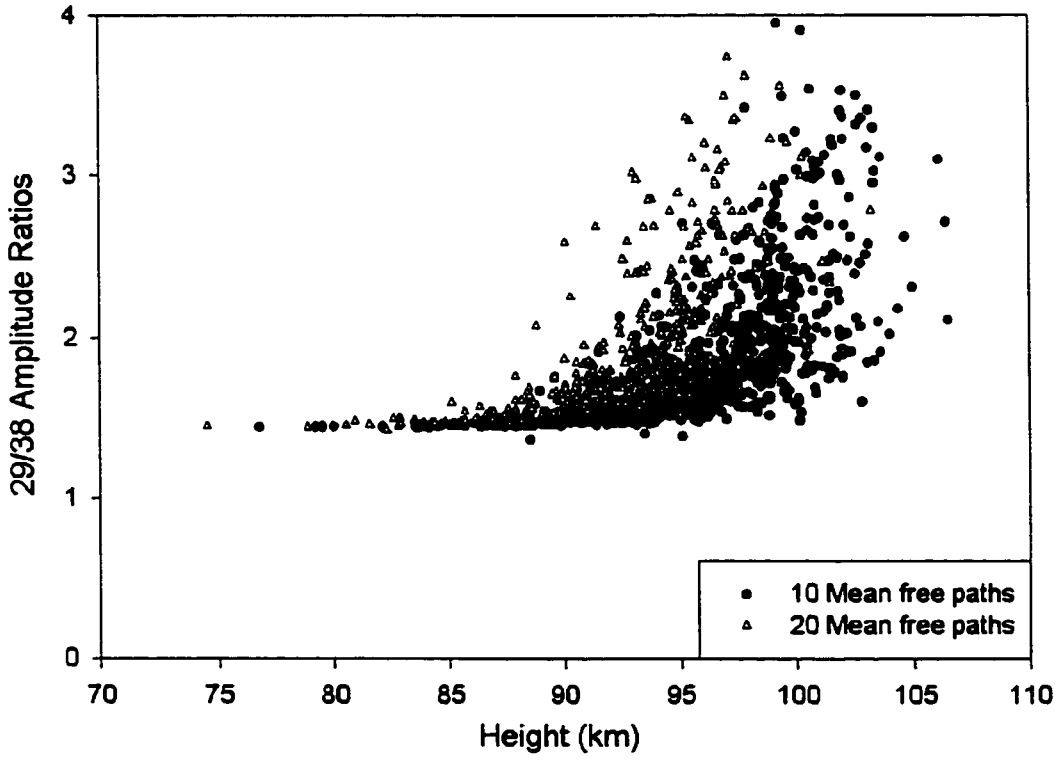

Figure 5.3: Amplitude ratios from simulation including Faraday rotation and initial radius with a Gaussian radial electron density

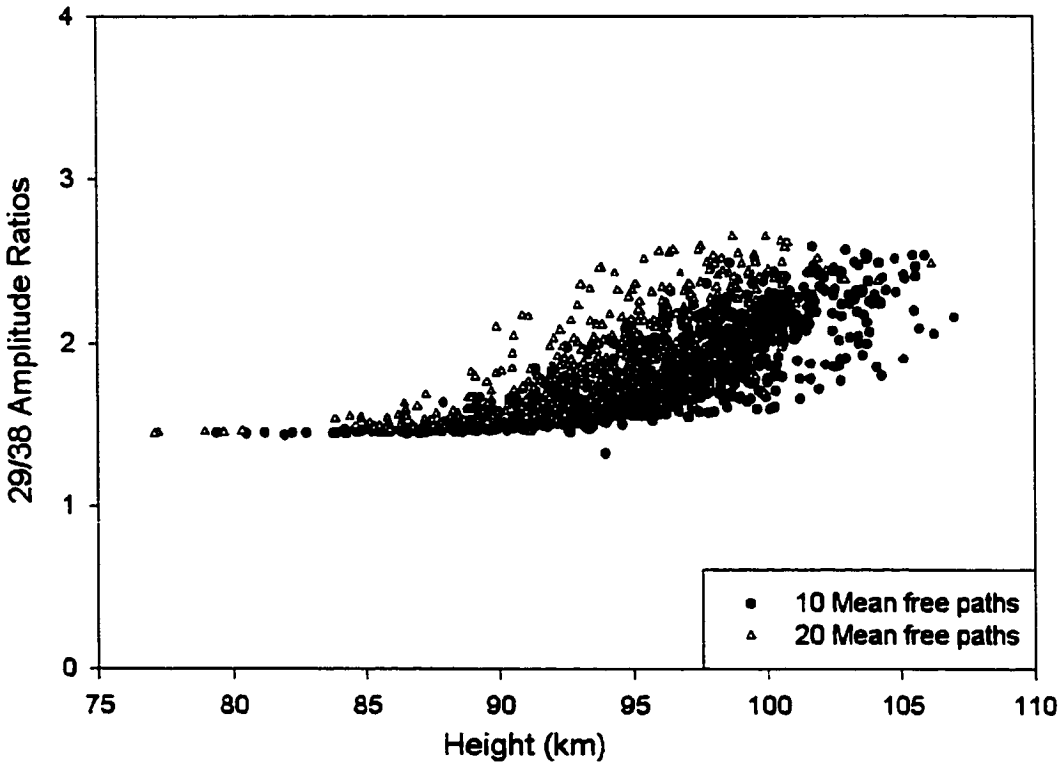

Figure 5.4: Amplitude ratios from simulation including Faraday rotation and initial radius with a exponential radial electron density

amplitude, the portion which was formed first will have expanded some distance, causing additional attenuation of the echo.

The size of the first Fresnel zone is $(2R_0\lambda)^{1/2}$, where R_0 is the range and λ the wavelength. This size is of order 1 km at meteor altitudes, for radars operating in the tens of MHz. The meteor crosses this length in $(2R_0\lambda)^{1/2} V^{-1}$ seconds. When the integration along the path is performed (Peregudov, 1958), the attenuation factor will be:

$$\alpha = \frac{[1 - \exp(-\Delta)]}{\Delta} \tag{5.3}$$

where

$$\Delta = \frac{2k^2 D (2R_0\lambda)^{1/2}}{V}. \tag{5.4}$$

This calculation is based on the assumption of a Gaussian initial electron density profile, which may not be correct. However, even for relatively slow meteors this effect was found to be small, so further corrections to it were deemed unnecessary.

5.6 Fragmentation

The evidence shows that fragmentation is present in meteors of the size detected by the radar (McCrosky, 1955; Jacchia, 1955; Campbell *et al*, 1998). If the fragmented grains have a lateral separation, reflections from different trails will interfere and cause attenuation. Since there is no reason for the fragmentation of any two meteors to be the same, even if those meteors belong to the same stream, this will cause scatter in the amplitude ratios. The scatter will apply equally to underdense and overdense meteors, since both will be made up of multiple trails.

The attenuation due to multiple trails is easy to calculate. The complex amplitude can be added from each trail: each will have a slightly different phase depending on the extra distance from the meteor trail axis. The total power is then a straightforward calculation from the sum of the reflected fields.

5.6.1 Optical determination of mass distribution index

The size distribution of the fragments can be determined, or at least narrowed down, using video observations of meteors. The light curve of the meteor will be the sum of radiation from all the fragments; by examining a large number and comparing them to theoretically generated light curves some characteristics of the grains may be determined.

To describe size distributions of particles, the mass distribution index, and the related population index, can be calculated. We assume that the masses of particles follow a power law of the form of equation 2.28:

$$dn \propto m^{-s} \tag{5.5}$$

where dn is the number of particles falling inside the mass range m to $m + dm$, and s is the mass distribution index. For any positive s, the number of particles at a given small mass will be larger than at a large mass. The higher the value of s, the greater the excess of small particles will be.

In order to obtain a large number of light curves, single station observations of sporadic meteors from the 1999 Leonid campaign in Israel were used. Since heights could not be calculated from these observations, the light curves were plotted as luminosity against time. The classical equations of meteor ablation (McKinley, 1961; Campbell *et al*, 1998) can be used to generate light curves. For some angle of entry, particle velocity and reasonable physical parameters, the light produced as a function of time or of height can be generated. It has been shown (Campbell *et al*, 1998) that a good fit to most video light curves is only possible if the meteor is assumed to be a collection of fragments ablating individually.

The unmodified classical equations of ablation are too simplistic for simulating meteor ablation. They assume that the kinetic energy received by the meteoroid from collisions with air molecules initially goes into heating the body, until the object reaches its boiling point. The energy is then used to ablate the meteor surface. While it is true that meteoroids in the size range of interest will heat essentially

uniformly, the boiling point is not very significant since the external pressure is so small. The meteoroids should instead begin to produce light long before they reach the temperature at which they would boil at standard atmospheric pressure. For this reason the equations were modified slightly from the classical formulation. The Clausius-Clapeyron equation was used to calculate the vapor pressure of the substance based on its temperature, and this was used to derive the rate of mass loss, as in Bronshten (1983).

$$\frac{dm}{dt} = \left(\frac{m}{\rho_m}\right)^{2/3} A\psi \exp(K) P_a \frac{\exp\left(\frac{-L\mu}{k_B T}\right)}{(2\pi k_B T/\mu)^{1/2}} \tag{5.6}$$

where

$$K = \frac{L\mu}{k_B T_b}. \tag{5.7}$$

Here ρ_m is the meteor density, A is the shape factor (1.2 for a sphere),ψ is the condensation coefficient (1 for metals, 0.5 for other substances (Bronshten, 1983)), P_a is the atmospheric pressure, L the heat of ablation, k_B the Boltzmann constant, T the meteor temperature, and μ the atomic mass of the substance.

The temperature equation is therefore used throughout the meteor's flight, and is modified to include the effect of energy lost with ablating meteor atoms.

$$\frac{dT}{dt} = \frac{A}{cm^{1/3}\rho_m^{2/3}} \left(\frac{\Lambda \rho_a V^3}{2} - \frac{dm}{dt} L - 4\sigma\varepsilon\left(T^4 - T_a^4\right)\right) \tag{5.8}$$

where c is specific heat, ρ_a the atmospheric density, Λ the heat transfer coefficient (usually taken as 0.5), σ is the Stefan-Boltzmann constant, ε is the emissivity, and T_a the atmospheric temperature. The first term in the bracket is the kinetic energy gained as a result of elastic collisions with air molecules; the second term is the energy lost to ablation and the third is the energy radiated by the meteoroid, assuming it is a blackbody.

The standard luminosity equation is then used to find the luminous intensity, which is proportional to the kinetic energy of the mass lost:

$$I = -\frac{1}{2}\tau_I \frac{dm}{dt} V^2. \tag{5.9}$$

To compare measured light curves to the models, we must define the shape of the light curve. One significant parameter describing a light curve is the F value, which measures the skewness of the curve, or degree to which the curve is not symmetrical. It is defined as:

$$F = \frac{t_B - t_M}{t_B - t_F} \tag{5.10}$$

where t_B is the begin time, t_F is the end time and t_M is the time of maximum luminosity. The begin and end times are obviously dependent on the limiting magnitude: F values are usually calculated a predetermined number of magnitudes below the maximum. Since most useful light curves are 3 magnitudes above noise, F values were calculated at every half magnitude down from the maximum up to three below maximum. The average of these was used as the final value. F values can range between 0 and 1. A value less than 0.5 indicates that a light curve peaks in the first half of its trajectory; greater than 0.5 indicates a curve skewed toward the later part of the trajectory. An F of 0.5 describes a curve which is perfectly symmetric.

The sporadic light curves were found to have F values which varied depending on magnitude. The brightest meteors had F values greater than 0.5, and usually close to 1. Fainter meteors had a much wider range of F values, which averaged roughly 0.5 (Figure 5.5). This is consistent with previous light curve studies (e.g. Murray *et al* (2000)) which found that faint meteors have symmetric light curves on average.

Light curves were generated using individual fragments with a range of mass distributions, and the intensities were added to produce a cumulative light curve. Mass distribution indices between 1.5 and 2.5 were used for particle masses of 10^{-6}, 10^{-7} and 10^{-8} kg. For each mass distribution and mass, a large number of light curves were produced and an average F value calculated. The mass distribution index which best fit the data was between 1.8 and 1.9 (Figure 5.6).

The fragments were generated with a mass distribution index s, close to that calculated above. Since Geminid meteoroids probably have different physical characteristics from sporadic meteoroids, some variation was allowed.

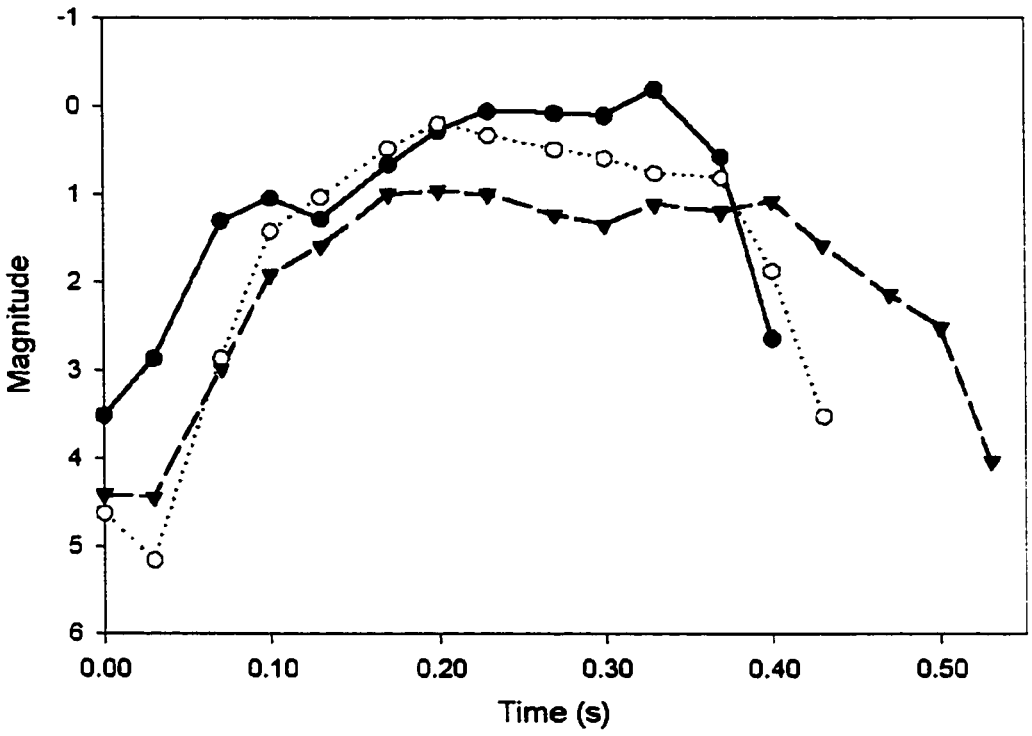

Figure 5.5: Observed sporadic light curves

5.6.2 Effects of Fragmentation

Other variables for fragmentation are the number of fragments in an individual meteor, the root mean square lateral spread of the particles, the radial distribution function and the height dependence of the fragmentation radius. The radial distribution function is completely unknown, so several possible forms were attempted: constant radial particle density, a Gaussian particle density function, a higher order exponential power, which was somewhere between the constant and Gaussian distributions, and a hollow distribution where the axial density was low, grew larger and then tapered again (Figure 2.8). The x coordinates (see Figure 5.7) of the fragments were generated randomly (the y component of the radial distance does not contribute to the phase change), and the phase of the return from each fragment was calculated. The electric fields were summed and the total returned power calculated.

The radius of fragmentation is the root mean square distance of the particles from the trail axis. It strongly influences the amount of scatter. By changing the radius

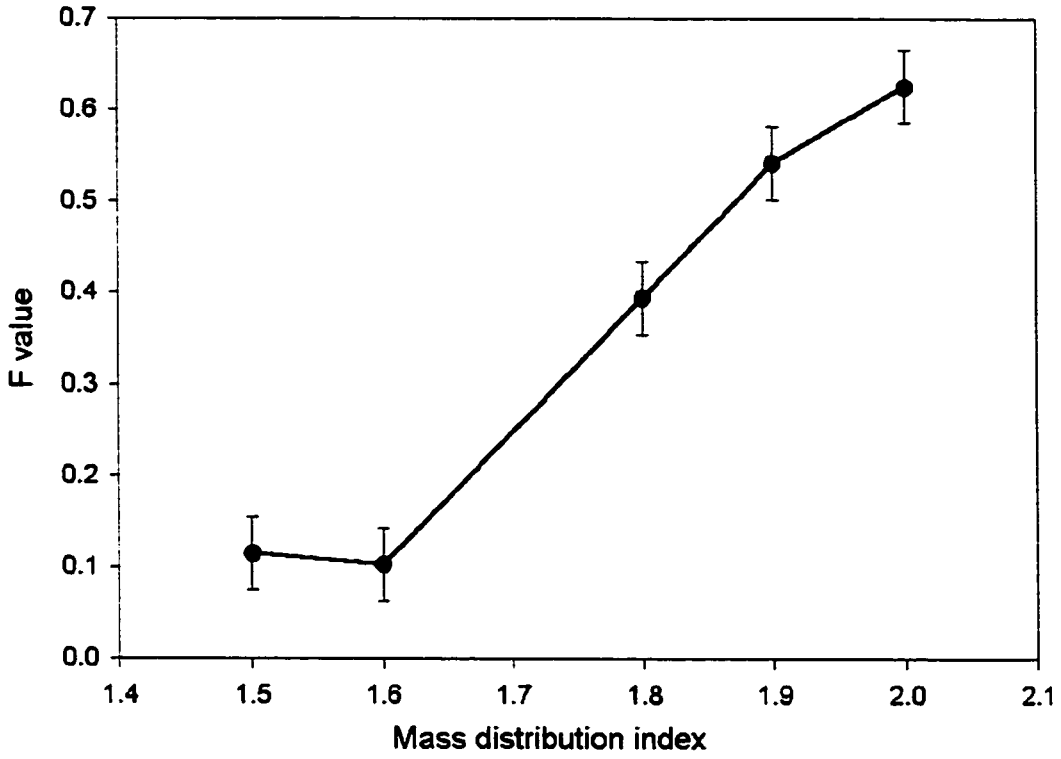

Figure 5.6: Skewness measurements for simulated sporadic light curves as a function of the mass distribution index of the fragments

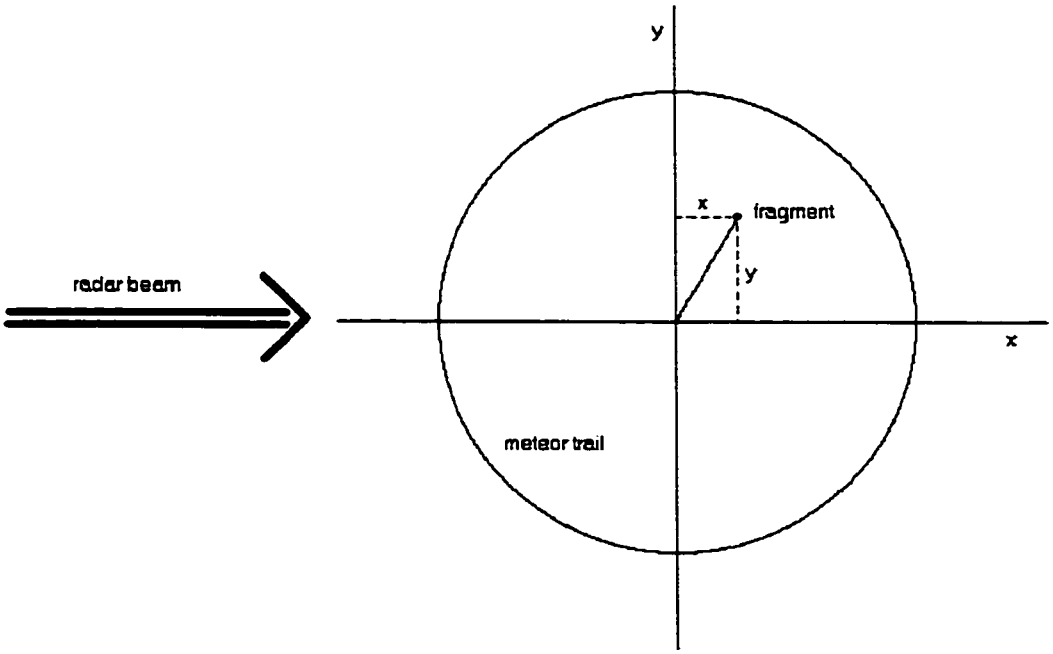

Figure 5.7: Geometry for reflection from a fragment of a meteoroid

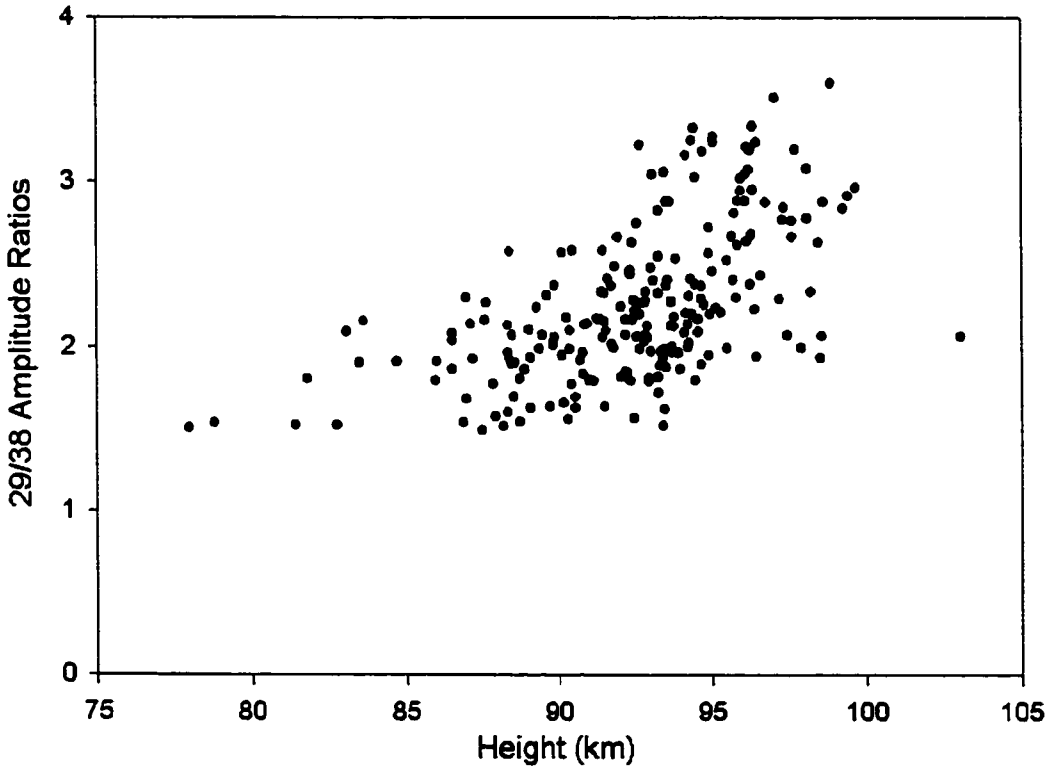

Figure 5.8: Amplitude ratios from simulation including fragmentation, with a radially constant distribution of fragments

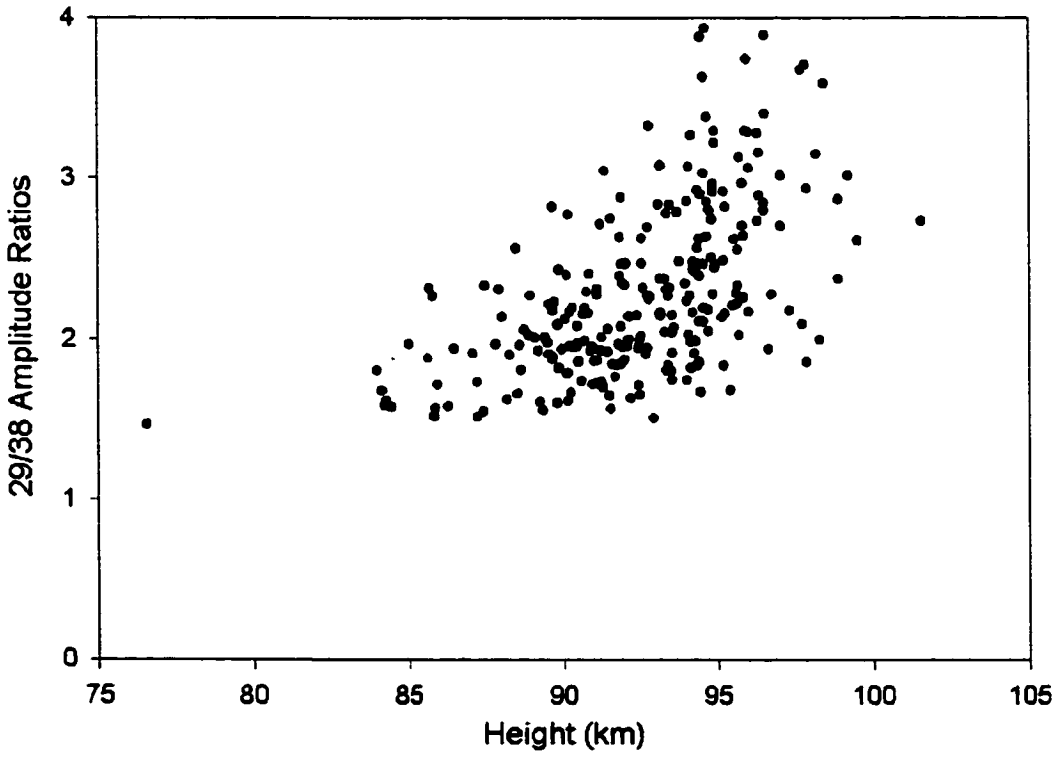

Figure 5.9: Amplitude ratios from simulation including fragmentation, with a Gaussian distribution of fragments

as a function of height, the amount of scatter at different heights can be adjusted. Results are shown for a 1 meter radius of fragmentation, constant with height, for a radially uniform (Figure 5.8) and Gaussian (Figure 5.9) distribution of fragments.

5.7 Solving for the coefficients

There are a large number of free parameters in determining the dependence of the initial radius as a function of height. The functional form of the radial electron density function for a single trail, the number of mean free paths to which the trail expands, the number and mass distribution index of the fragments and the height dependence of the radius of the fragments as a function of height may all be varied. Since the scatter in the data is so large, it will not be useful to simply fit the mean amplitude ratio as a function of height: the correct scatter must also be reproduced. The procedure will be described in the next chapter.

Chapter 6

Initial Trail Radius Results

6.1 Selecting and Testing the Model

In the previous two chapters, we obtained experimental plots of amplitude ratio against height, and developed a model to fit those observations. The task which remains is to find the set of parameters which will best fit the observations, and which can correctly predict other observations. Once the model with the least error has been found, we will use it to predict the amplitude ratios on the 17 and 29 MHz systems and the height distribution on different radar systems. If it describes the observations well, we can use the model with confidence to calculate a correction factor for radar fluxes.

6.2 Minimizing the Model Error

Since the observational data shows so much scatter, we cannot simply fit mean amplitude ratios at each height to those produced by a model. We need to find a model that describes not only the mean values, but also the scatter: for this reason we find the residual between the theoretical and observed density of points in a two dimensional grid. The data are divided into bins of 2 km height intervals and 0.25 amplitude ratio units (Figure 6.1), and the number of echoes falling in each bin is calculated. The values are normalized by dividing by the largest value. The square of the difference at

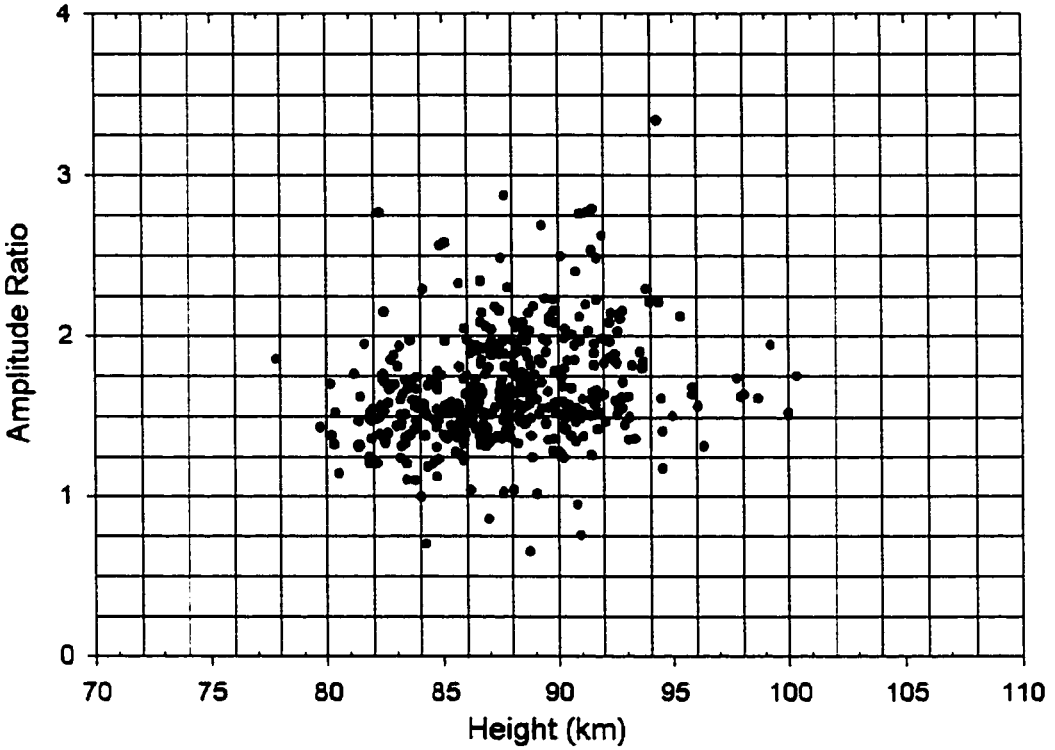

Figure 6.1: Binned data for error calculation

each point between the model and the observed data is calculated and summed over all the bins. The models are then ranked from least to most residual. This method will determine which model fits best both in terms of height distribution and mean amplitude ratio, and will take into account the scatter in both values.

6.3 Model Fitting

6.3.1 Model parameters

To find the best set of parameters of the meteor trail, we generate distributions of amplitude ratios for a large number of possible combinations and calculate the residual with the observed data for each. The parameters include all necessary information about the size and shape of individual trails, and the distribution of meteoroid fragments.

Table 6.1: Coefficients in simulation

Shape of $n_e(r)$	Exponential	Gaussian		
$r_0(h) = n$ (mfp)	10	15	20	
Shape of $n_f(r)$	Radially constant	Gaussian	Hollow	$\exp(-\|x\|^5)$
$r_f(h) =$	$0.04h - 2.3$	1.0	$-0.0375h$	$-0.0143h$
			$+4.625$	$+2.758$
s value of fragments	1.6	1.8	2.0	
Number of fragments	500	1000	2000	

The quantities to be varied are:

- Shape of the electron density function $n_e(r)$
- Height dependence of initial radius (number of mean free paths)
- Shape of radial density of fragments $n_f(r)$
- Height dependence of radius of fragmentation: Assume $r_f = Ah + B$
- s value of fragments: range from video observations
- Number of fragments

The simulation is time intensive: one simulation takes several minutes and 800 simulations take more than a day. For this reason, only three or four values in the appropriate range were chosen for each of the numerical coefficients (Table 6.1). The initial radius of the trail of a single fragment was taken to be 10, 15 or 20 times the mean free path, as implied by collisional models of the trail. For the radius of fragmentation, four linear functions with height were simulated: one had a fragmentation radius increasing with height, two with different slopes for which the radius decreased with height, and one which was constant with height. The values of the fragmentation radius for all the models were between 1 and 2 meters, as proposed by Hawkes & Jones (1978) for rotating meteoroids. The number of fragments varies

Table 6.2: Best fits

Model	$n_f(r)$ shape	$r_e(h) =$ n mfp	$n_e(r)$ shape	$r_f(h) =$	s value	N_f	residual
001312	constant	10	exponential	$-0.0143h$ $+2.76$	1.8	2000	1.813
201312	Gaussian	15	exponential	$-0.0143h$ $+2.76$	1.8	2000	1.819
321310	Hollow	20	exponential	$-0.0143h$ $+2.76$	1.8	500	1.822
201310	Gaussian	15	exponential	$-0.0143h$ $+2.76$	1.8	500	1.90
101311	Higher order	15	exponential	$-0.0143h$ $+2.76$	1.8	1000	1.93
221301	Gaussian	20	exponential	$-0.0143h$ $+2.76$	1.6	1000	2.10

with the size of individual fragments, since the whole meteor mass is fixed and the mass distribution index specified. For meteors in the radar mass range, generating more than 2000 fragments will produce a large number of particles smaller than 10^{-13} kg, which is the smallest size which evaporates and produces ionization. Smaller particles reradiate energy quickly because of their high surface area to volume ratio, and never heat to the point of ablation. There is therefore no use in generating more than 2000 particles, since the smallest particles will not contribute to the observed trail.

6.3.2 Geminid data

Every combination of the six parameters was simulated and the data binned in sections; the density of points was then determined for each of the 864 models. The residual between the simulated data and the Geminid data was calculated.

The best three models were selected by this procedure: the second and third models had residuals within 1% of the best model. All three had an exponential distribution of electrons in the trail, an s value of 1.8, and the same fragmentation radius dependence with height (Table 6.2). For comparison, the next three models are shown.

The results do not depend strongly on the shape of the fragmentation distribution,

the number of particles, or the dependence of initial radius on height. This insensitivity to the initial radius of ionization of individual fragments demonstrates that the principal effect in the radar height ceiling is fragmentation, and not the radius of individual trails. The initial radius is due more to the fragmentation of the meteoroid than to the spreading of the trail of electrons.

As a test, the three models were used to find a correction factor for the three frequencies. Each of them showed that 78% of echoes are seen on 17 MHz, 51% on 29 MHz, and 34% on 38 MHz. Since the models give the same correction factor, the differences between them are not significant and any of the three can be used to calculate fluxes.

Since the fragmentation radius is the strongest effect, an attempt was made to further refine the value. All parameters in the models were the same as the best model above, except the radius of fragmentation. The best model was found to have a radius of fragmentation $r_f = -0.01h + 2.4$. The most important parameter was the average radius of fragmentation; since the range of heights being studied is relatively small, the slope is more uncertain. Figure 6.2 shows the residuals for models with different average radii of fragmentation. Each model was simulated with a different random seed ten times; the standard error on each measurement of the residual is shown by the error bars. The best average radius is about 1.5 meters, and radii between 1.4 and 1.6 meters are possible.

This model does not necessarily apply to sporadic meteors as well: to determine if it is a good model for all meteors, more data are needed.

6.3.3 Quadrantid data

Only 56 Quadrantid echoes were gathered on 29 and 38 MHz during the 2002 Quadrantids, on January 3 and 4. The Quadrantids are expected to resemble sporadic meteors more closely than the Geminids, since their origin is more likely cometary, but with such small numbers the results of any simulation will be highly uncertain. For this reason, it was assumed that all parameters except the radius of fragmentation were identical. If the composition of Quadrantid meteoroids is significantly different

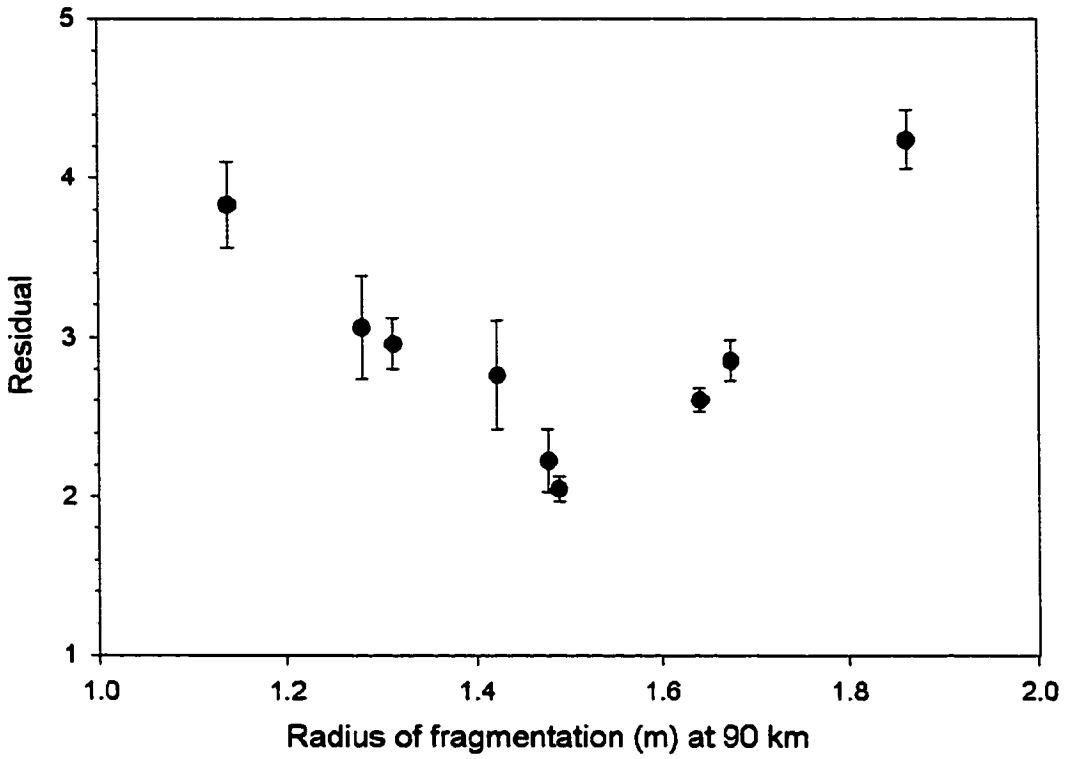

Figure 6.2: Residuals for Geminid data, as a function of radius of fragmentation

from that of Geminid meteors, it will affect this quantity more than any of the others. A fit was done varying just the slope and intercept of the radius of fragmentation as a function of height.

The scatter on the Quadrantid data was smaller than that on the Geminid data, which corresponds to a smaller radius of fragmentation. The best fit was $r_f = -0.0015h + 0.25$ (h in kilometers), giving a fragmentation radius roughly ten times smaller than that of the Geminid meteors.

6.3.4 Sporadic data

While there is a great deal of sporadic data, the conclusions reached from these data are uncertain since no account has been taken of variation of initial radius with velocity. Still, it is useful to fit some sporadic data to determine whether the correction factor calculated from Geminid data can reasonably be applied to sporadics.

Data from December 12 and 13, 2001 were used, since the individual meteor files

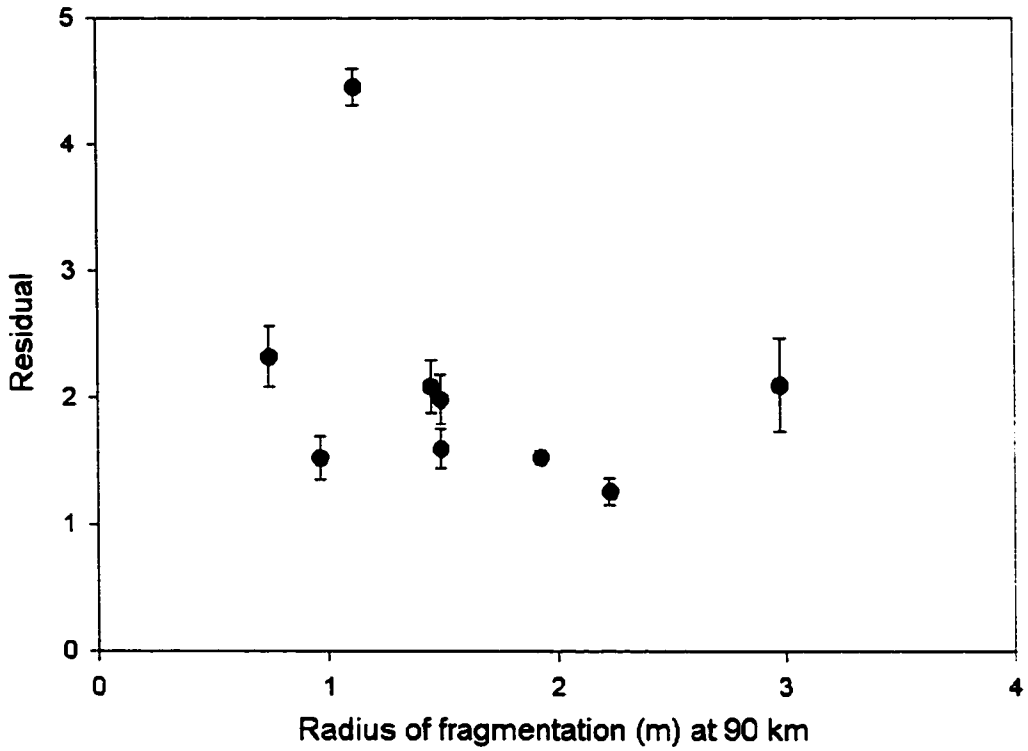

Figure 6.3: Residual between model and observed for sporadic meteor data, as a function of radius of fragmentation

were available for those days. Geminid echoes were removed and the others used with the above procedure. Simulating the data with the 864 original Geminid models, the same three were found to fit the data best, so all variables except the radius of fragmentation seem to apply equally to sporadics. The fragmentation radius was then independently simulated, as with the Geminids and Quadrantids. The best fit was $r_f = -0.005h + 3.0$, larger than even that of the Geminids. The extra scatter might be due to velocity effects, or differing fragmentation mechanisms for sporadic meteors, rather than to a physically wider distribution of fragments. A plot of residual against average radius of fragmentation shows that the uncertainty is much greater in this case (Figure 6.3). The best radius of fragmentation is approximately 2 meters, but radii between 1.25 and 2.75 m are within the error bars on the residual. Because the uncertainty is so large, the Geminid model fits as well as any we could derive for the sporadics, and we will use that model for the calculation of correction factors.

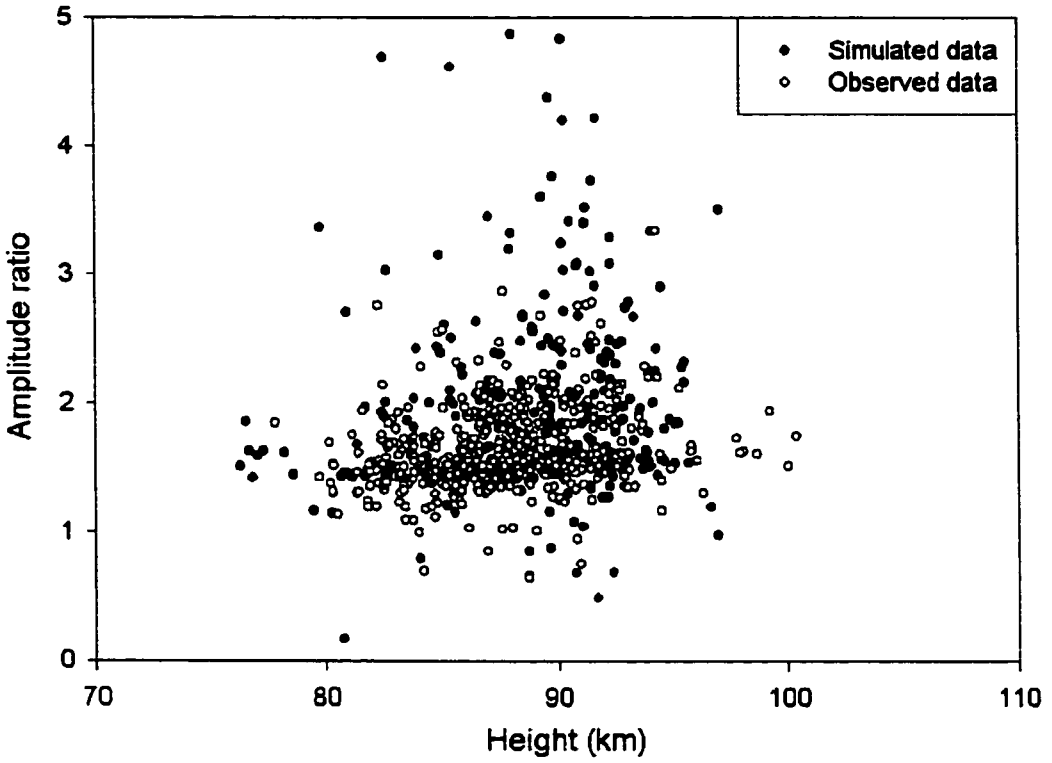

Figure 6.4: Observed and simulated Geminid amplitude ratios: 29 and 38 MHz

6.4 Testing the Model

6.4.1 Comparing with other data

As a test of the accuracy of the model which best fit the 29 and 38 MHz ratios, the model was used to predict the amplitude ratios on 17 and 29 MHz. If the model describes the physical situation reasonably well, it should work as well for different frequency pairs.

Figure 6.4 shows the results of the 29/38 MHz simulation, and Figure 6.5 shows the results for 17/29 MHz. The model-generated echoes have a very similar distribution to the observed data, with a little more scatter toward higher amplitude ratios. This may simply be due to the fact that the number of generated echoes was in both cases slightly larger than the number of observed echoes.

As a further test of the model, we compare the height distributions on the three radar systems with those predicted by the model. The model starts with photographic

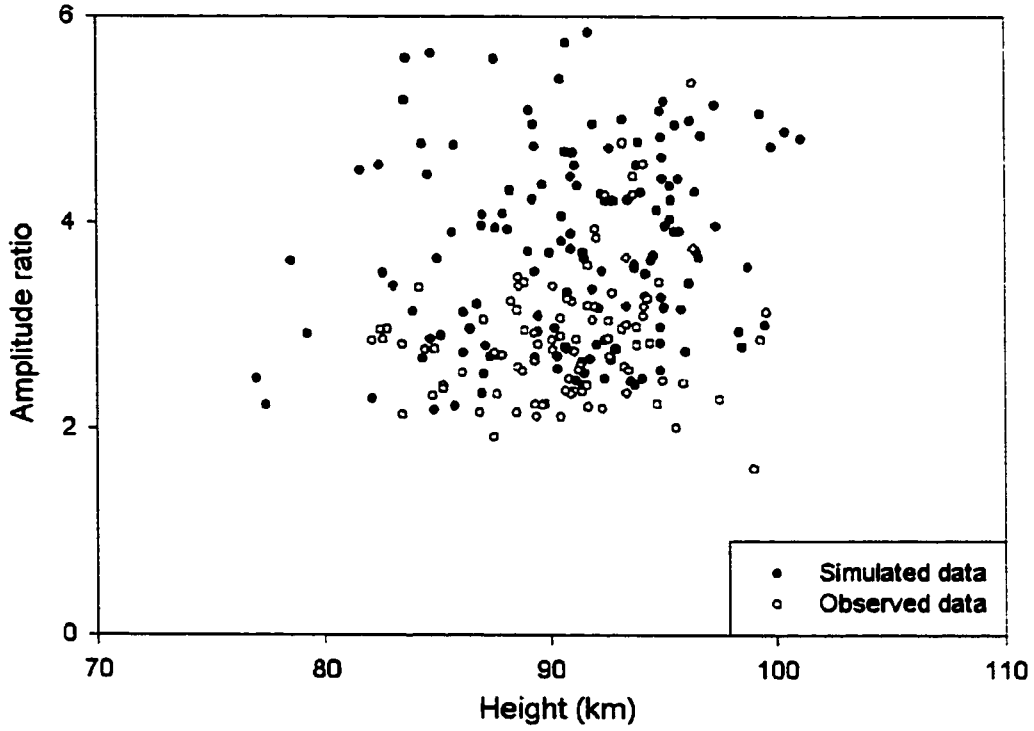

Figure 6.5: Observed and simulated Geminid amplitude ratios: 17 and 29 MHz

heights for Geminids, corrected to the radar limiting magnitude, and calculates the number theoretically observed on each system. Figures 6.6, 6.7 and 6.8 show the results. The maximum heights for all three agree closely and the shapes of the observed and modelled curves are very similar. This agreement is particularly remarkable since the individual observed height distributions were not explicitly included in the original model, and no 17 MHz data of any kind was included.

This model explains these aspects of the observations well. It is not necessarily unique: other combinations of parameters may exist which would also correctly predict the observations. However, it is clear that this model is a much better description of the initial radius problem than has been previously available, simply because it includes the effects of fragmentation. All physically likely combinations of parameters were modelled: a more thorough search of the parameter space might find other minima but the parameters would not be physically possible.

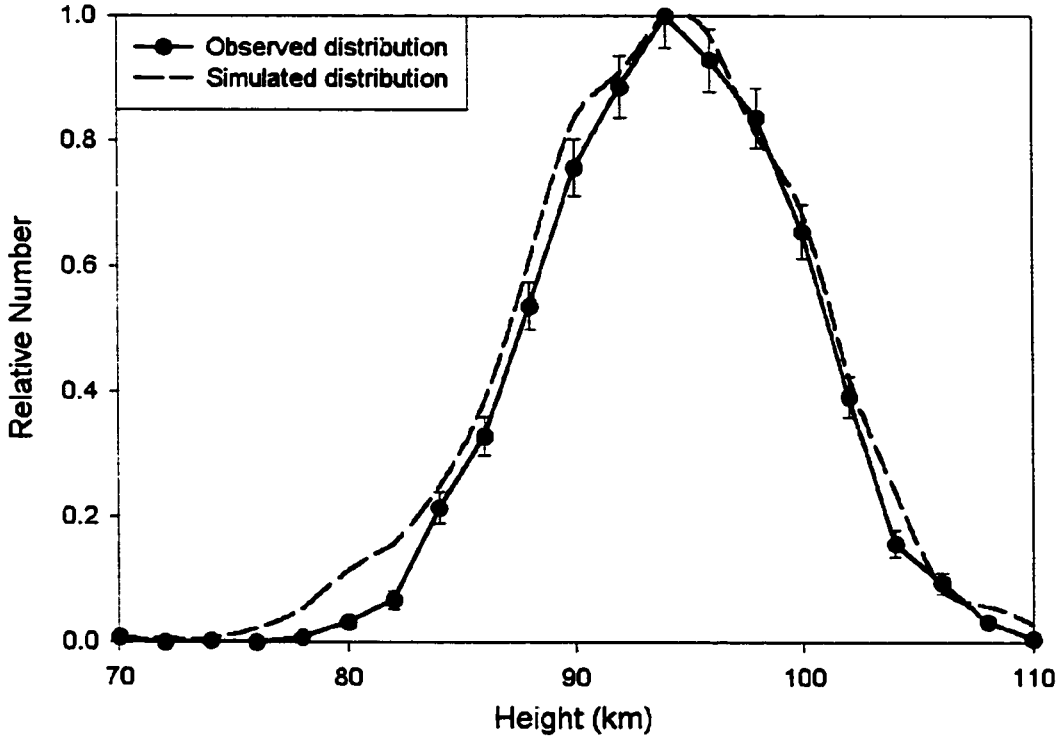

Figure 6.6: Observed and simulated Geminid height distributions: 17 MHz

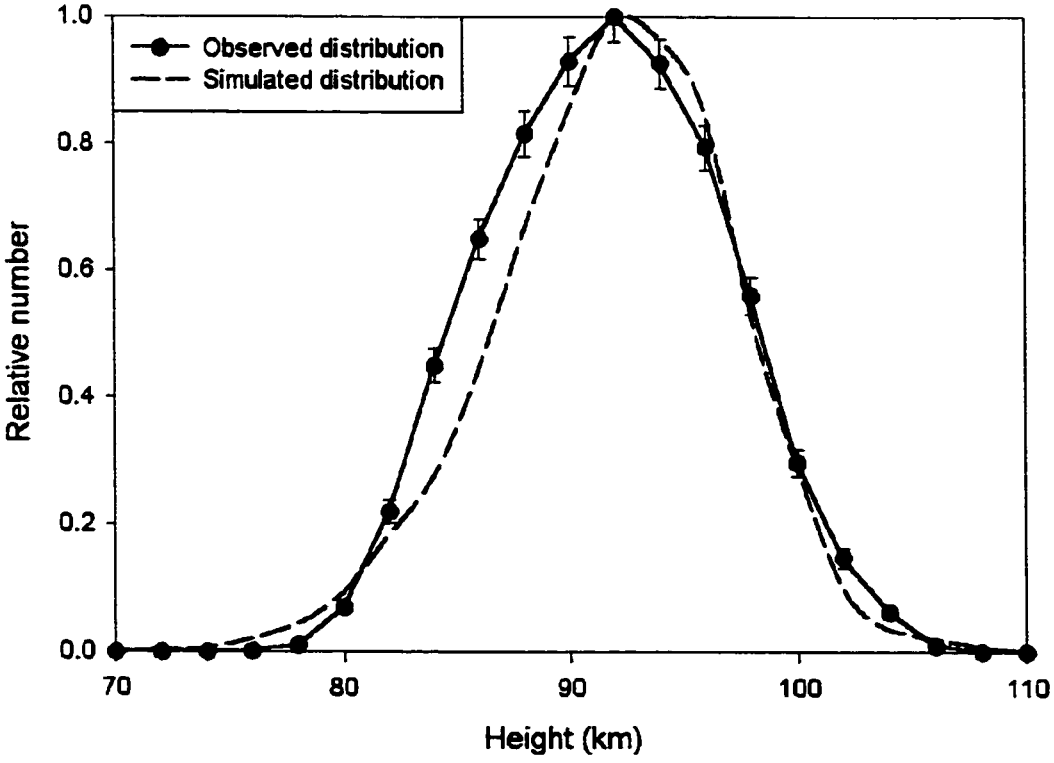

Figure 6.7: Observed and simulated Geminid height distributions: 29 MHz

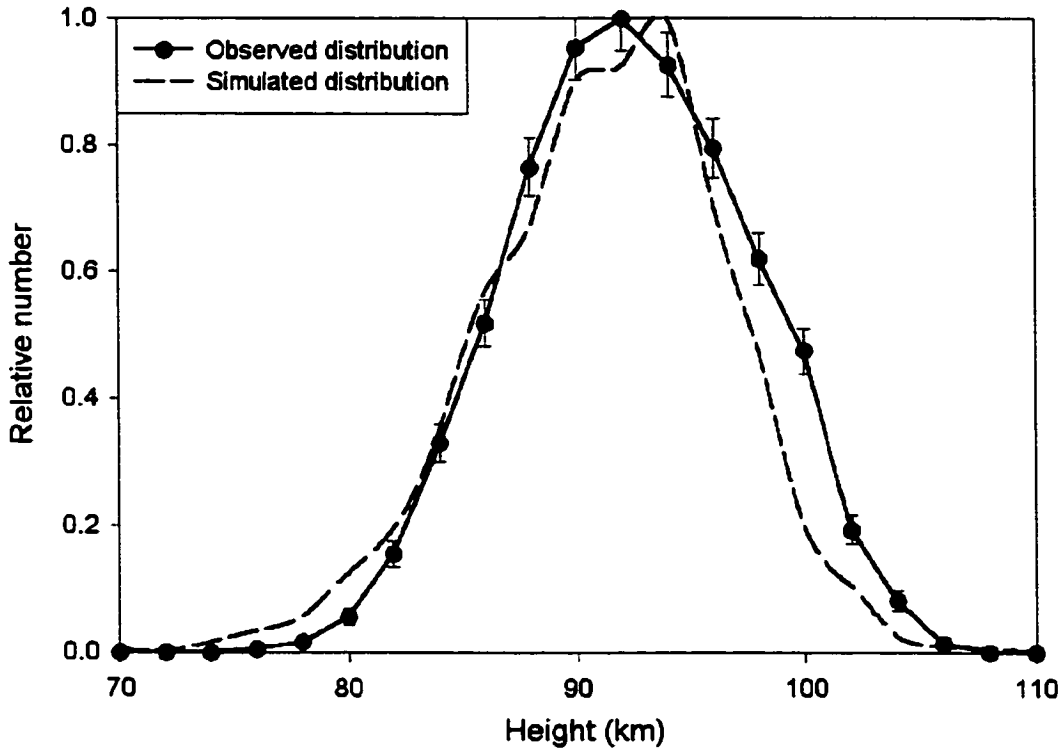

Figure 6.8: Observed and simulated Geminid height distributions: 38 MHz

6.4.2 Implications for structure of meteoroids

The fragmentation radius is of particular interest because of the insight it provides into the physical structure of meteoroids. The width of the fragmented trail is quite large, varying between 1.8 meters at 70 km to 1.2 meters at 110 km for the best model. The size of the trails implies that these faint meteors fragment high in the atmosphere, and have some initial radial velocity component, which could be caused by spinning of the meteoroid (Hawkes & Jones, 1978). Evidence of rotation of larger Geminids is given in Beech & Brown (2000), where fireball flickering is linked to rotation of the meteoroids. Since the objects considered in that study were much larger than the ones considered here, the rotation rates will not be applicable, but the fact that many large meteors display flickering is an indication that meteoroids do rotate. Meteoroids may acquire angular momentum when they separate from their parent bodies, through collisions with smaller particles (Hawkes & Jones, 1978) or by radiation pressure on non-uniform surfaces (Paddack, 1969).

There is an upper limit on the angular frequency of a meteoroid past which the internal bonds of the meteoroid material are not strong enough to hold it together. Öpik (1958) derived the formula for rotational bursting, based on the size of the meteoroid and its tensile strength:

$$\omega_{max} = \frac{1}{R}\left(\frac{S_t}{\rho}\right)^{1/2} \tag{6.1}$$

where S_t is the tensile strength. If the meteoroid spins faster than this, the outer layers will break off. The tensile strength of meteoroids is very uncertain: for a stone meteoroid the tensile strength might be 2×10^8 Nm^{-2}; for a fragile cometary meteoroid the value would be much lower, 2×10^3 Nm^{-2} (Whipple, 1963). A cometary meteoroid of mass 10^{-5} kg could not spin faster than 10^3 rad/s; a meteoroid at the radar's detection limit of about 10^{-8} kg would have to spin slower than 10^4 rad/s.

The height of fragmentation can be found simply as the height at which the fragmentation radius is zero, and the slope of the fragmentation radius function gives the radial velocity. In meters per second, the radial velocity is

$$v_r = -AV\cos z \tag{6.2}$$

where z is the zenith angle of the meteor radiant, V is the velocity and A the slope of the radius of fragmentation function. The negative sign compensates for the fact that A is negative. If we assume that the radial spread of the meteoroid fragments is due to rotation of the meteoroid, we can calculate the angular frequency. If the particle is a sphere, the angular frequency can be found:

$$\omega = \frac{v_r}{R} = v_r\left(\frac{3m}{4\pi\rho}\right)^{-1/3} \tag{6.3}$$

where R is the meteoroid radius, m its mass and ρ its density. Here the radial velocity of the particle away from the meteoroid is the tangential velocity of the particle when attached to the main body. This assumes that the axis of rotation of the meteoroid is parallel to its trajectory in the atmosphere: if it is not, the meteor trail formed by the fragments will have an ellipsoidal cross-section.

To find the angular frequency of the rotating meteoroid from the radial velocity with equation 6.3, one needs to make assumptions about the mass, density and shape of the meteoroid, none of which are well known for cometary meteoroids.

Assuming a zenith angle of 45°, the radial velocity of the Geminids is 0.24 m/s, the Quadrantids 0.04 m/s, and sporadics 0.33 m/s. This will vary among meteoroids: in particular, larger meteoroids have a smaller upper limit on radial velocity because of rotational bursting.

The error on the height of fragmentation and angular frequency can be estimated by simulating many heights and angular frequencies close to those found above. By comparing the error on the different combinations, a range may be found which could produce the observed results.

For the Geminids, the best height of fragmentation was 240 km; heights between 220 and 260 km produced results within 5% of the best results. Assuming a density of 1500 $kg \cdot m^{-3}$ and an average mass of 10^{-9} kg, the angular frequency of the Geminid meteors is 4500 rad/s, with an estimated error of 500 rad/s.

The height of fragmentation for Quadrantids was 170 km. Assuming the same physical properties as above, the average angular frequency was found to be 700 rad/s. It is expected that the Quadrantids, being less dense and presumably more fragile than the Geminids, would have a lower angular frequency, but there is too little Quadrantid data to draw any firm conclusions about their structure based on the available data.

For the sporadic group, the best height of fragmentation was 260 km, and the average angular frequency 6000 rad/s. The fact that sporadic meteors spin faster than Geminids is surprising, but given the large uncertainty in the radius of fragmentation the uncertainty in the angular frequency must also be large. The fact that sporadics are not a homogenous group makes it difficult to determine any specific quantity: a more accurate result might be derived when sporadics can be divided by velocity and radiant.

All the calculated rotation rates are under the bursting limit for meteoroids in this size range. The error in these quantities is large, particularly in the heights: if these

could be determined more accurately it might help to determine what the volatile component of the meteoroids is. This is an area which merits further research.

Rotation of meteoroids is not the only explanation for the radial velocity component of the meteoroid fragments. The fragments might also acquire energy when the volatile component in which they are embedded evaporates, carrying them off the meteoroid surface. If this mechanism is responsible, it will not change the height of fragmentation or the correction factor for radar fluxes.

6.5 Correction to Radar Fluxes

The last step is to use the model developed to find a correction factor for any wavelength at which meteors are observed. The simplest procedure to find this correction factor is to simulate meteors with a height distribution identical to that of the radiant being observed, as determined by optical methods, and record the number which have sufficient amplitude to be observed. This is compared to the number which would be observed if there were no fragmentation or initial radius effects.

This was done for several wavelengths in the meteor radar range, including the three in our system. The results were plotted, and a curve fit through them (Figure 6.9).

To alter the height distribution, we used the dependence of height of maximum luminosity on velocity of Jacchia, Verniani & Briggs (1965). They found the relation

$$\rho_{max} \propto v^{-1.7} \tag{6.4}$$

where ρ_{max} is the density of the atmosphere at maximum luminosity. The new maximum of the height distribution can be found from the atmospheric density at the new velocity:

$$\rho_{max2} = \rho_{max1}\left(\frac{v_2}{v_1}\right)^{-1.7}. \tag{6.5}$$

The new height can then be found with the scale height of the atmosphere in the height range under consideration, from the fact that $\rho \propto \exp(-h/H)$. The scale

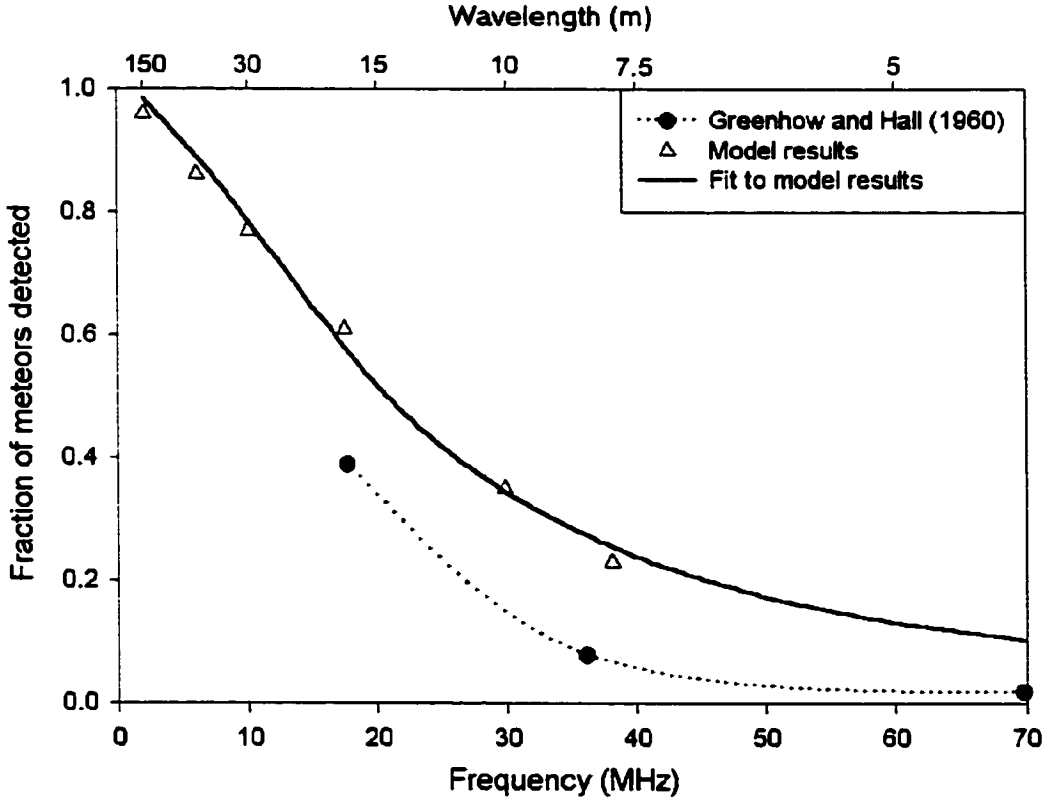

Figure 6.9: Correction factor as a function of wavelength for Greenhow & Hall (1960) and current study

height H is 5.8 km, from the US Standard Atmosphere (1976).

$$\exp\left(-\frac{h_{max2}}{H}\right) = \exp\left(-\frac{h_{max1}}{H}\right)\left(\frac{v_2}{v_1}\right)^{-1.7} \tag{6.6}$$

or

$$h_{max2} = h_{max1} + 1.7H\ln\left(\frac{v_2}{v_1}\right). \tag{6.7}$$

Similarly, one can adjust to different limiting magnitudes. Smaller meteors ablate higher than larger meteors: according to the faint video observations of Hawkes & Jones (1980) and photographic observation of larger particles (Jacchia, Verniani & Briggs, 1965), the height of maximum luminosity follows the relation

$$\rho_{max} \propto m^{1/3} \tag{6.8}$$

where m is the limiting mass. This gives a height relation of

$$h_{max2} = h_{max1} + H\ln\left[\left(\frac{m_2}{m_1}\right)^{1/3}\right] \tag{6.9}$$

or as a function of limiting magnitude:

$$h_{max2} = h_{max1} - \frac{H}{3}\ln(2.5)(M_{lim2} - M_{lim1}). \tag{6.10}$$

Putting equations 6.7 and 6.10 together, one has for the height of maximum luminosity:

$$h_{max2} = h_{max1} + 1.7H\ln\left(\frac{v_2}{v_1}\right) - \frac{H}{3}\ln(2.5)(M_{lim2} - M_{lim1}). \tag{6.11}$$

Using values from Jacchia, Verniani & Briggs (1965), this is:

$$h_{max} = 99.6 - 1.77(M_{lim} - 9) + 9.86\ln\left(\frac{v}{33.7}\right). \tag{6.12}$$

where h_{max} is in kilometers and v in kilometers per second.

Equation 6.12 can be used to calculate the height distribution for any of the sources, which can then be simulated and correction factors calculated for each frequency. A function was then found which fit the data. We also require that the

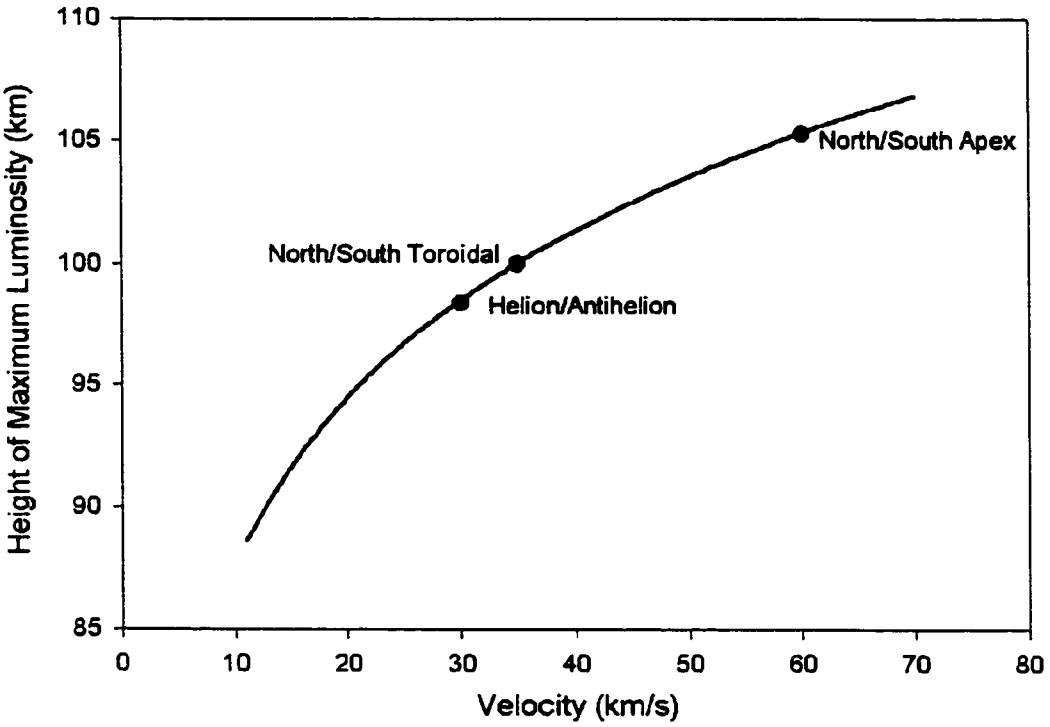

Figure 6.10: Average height of maximum luminosity as a function of meteoroid velocity

fraction observed approach unity as the wavelength becomes large, and zero as the wavelength becomes small. Similarly, the number observed should be high when the height distribution peaks at a low altitude; few echoes should be observed if the height distribution peaks at a high altitude. The function which best fit all the data and satisfied the above constraints was found to be:

$$C(h_{max}, \lambda) = \left[1 + \exp\left(\frac{h_{max}}{8.59} - \frac{\ln \lambda}{0.563} - 6.90\right)\right]^{-1} \tag{6.13}$$

where C is the fraction of meteor echoes detected by the radar.

The velocities of the sporadic sources were taken from Jones & Brown (1993), with a standard deviation of 5 km/s: the height probability for each meteor was obtained by correcting that of Jacchia, Verniani & Briggs (1965) for sporadic meteors to the correct limiting magnitude and velocity (Figure 6.10).

The correction factors for each of the sporadic sources are shown in Figure 6.11 as

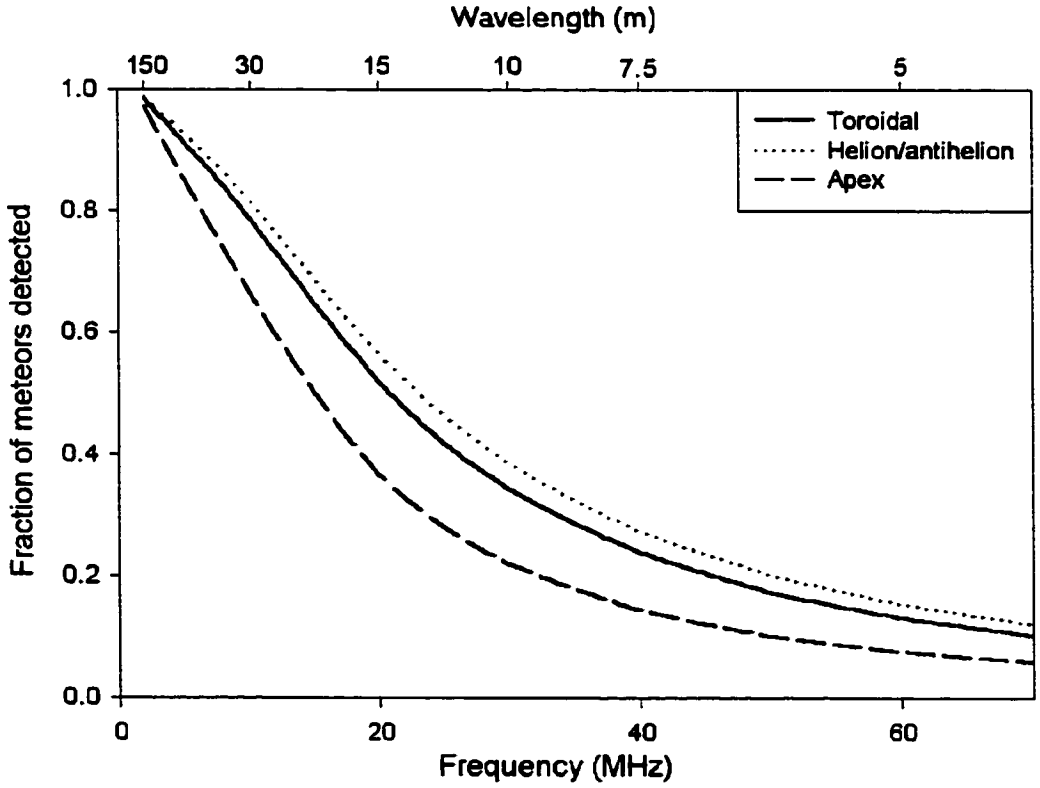

Figure 6.11: Correction factor as a function of wavelength for each of the sporadic sources

a function of radar frequency or wavelength. The apex source is the most undersampled, as expected because of its high velocity. The correction factors are significantly different from those of Greenhow & Hall (1960): for the 29 MHz system, the new correction factors are smaller by a factor of four.

These correction factors are somewhat uncertain because of the scattered sporadic measurements. They are still an improvement over previous studies since they take into account fragmentation, which is the most significant effect.

Chapter 7

Sporadic Fluxes

7.1 Generalizing the Correction Factor

The primary object of calculating the effect of initial trail radius on radar observations of meteors was to find the flux of sporadic meteors from each of the sporadic sources. Having derived the correction factor to radar observations at any frequency and for any velocity distribution, we can proceed to calculate fluxes.

The main issue we have not addressed in this study is velocity. We account only for difference in height of maximum luminosity due to velocity, and not for any effect the velocity might have on the correction factor independent of height. According to the Jones (1995) model, the initial radius at any height for a single particle should vary with the velocity, so our correction factor is optimized for meteors with an atmospheric speed of 35 km/s like the Geminids. Without analysing many more echoes from other showers or from sporadics for which velocities have been determined, it is not possible to determine the velocity dependence of the attenuation, so we shall follow Greenhow & Hall (1960) in assuming that there is no velocity dependence. The correction factor obtained here will be valid for all sporadics, since the model has been shown not to be significantly different from the sporadic one, but may be in error for particular sources.

With these caveats, we can proceed to find the sporadic fluxes from each of the sporadic sources. To calculate a flux from any source, we need the raw rate of observed

meteors, which is divided by the collecting area of the observing system. We then correct for observing effects to find the true flux.

7.2 Meteor rates

The first task is to isolate the echoes of meteors which come from particular sporadic sources. A procedure similar to that for isolating shower meteors, as described in Chapter 4, is used, but the situation is slightly more complicated. The radiant of sporadic sources is much more diffuse than shower radiants, typically having a radius of order 15° as opposed to 2° for the Geminids. Also, we wish to remove shower meteors and any meteors which do not belong to the sporadic source being investigated. Since showers often occur in the same regions as sporadic sources, removing them is not trivial; also we must have a statistical way of removing echoes which fall on the echo band of a sporadic source but come from a different radiant.

7.2.1 Removing shower meteors

The simplest way to remove shower meteors from the data is to use the inverse of the procedure described in Chapter 4. All echoes with directions within 3° of 90° of the radiant are counted as shower meteors. The difficulty in this case is that, particularly when a shower radiant overlaps the radiant of a sporadic source, many echoes due to that source will be removed at the same time. The matter is worse if the shower being removed is a weak one: by removing all echoes on its echo line we may lose more sporadic meteors than shower meteors. In general, only the strongest showers show up at all in the sporadic fluxes, and only during the times of their peak activity. Very weak showers can be counted with the sporadic background, since they may contribute only of order 10 echoes per day. What is needed is a measure of a shower's activity compared to background: some percentage of the echoes falling on the shower's echo line are then removed. For example, we may need to remove 100% of echoes falling on the Geminid radiant at the time of maximum, but only 5% of echoes from the Ursid radiant at the time of maximum.

Table 7.1: Showers removed for sporadic analysis

Shower	Day of Maximum	RA	dec	Sporadic Source	Percent Removed
Quadrantids	3	233	49	NT	100
Lyrids	111	271	34	NT	5
Eta Aquarids	125	336	0	NA	10
Arietids	159	45	23	HE	70
Zeta Perseids	164	63	26	HE	5
Beta Taurids	180	79	21	HE	5
South Delta Aquarids	211	339	-17	AH	10
North Delta Aquarids	226	344	2	AH	10
Perseids	226	48	58	NA	70
South Iota Aquarids	219	337	-12	AH	10
North Iota Aquarids	239	350	0	AH	10
Giacobinids	281	262	54	NT	5
Orionids	295	95	16	SA	70
Leonids	322	155	22	NA	70
North Taurids	310	54	21	AH	10
South Taurids	307	53	12	AH	10
Geminids	348	113	33	AH	100
Ursids	357	217	76	NT	5

Activities were determined with two programs, one of which calculated the activity in celestial coordinates (right ascension and declination) and the other in heliocentric coordinates (solar longitude and latitude). Both use the method of Jones (1993). Showers show up strongly in celestial coordinates when the resolution is set to 3° (Figure 7.2); sporadic sources are clear in heliocentric coordinates with a resolution of 15° (Figure 7.3). For each possible radiant, every echo was tested to see if it fell at 90° from the radiant. To correct for echoes which belong to other radiants, every echo is given a weight according to a function:

$$f(x) = \left(1 - \left(\frac{x}{x_0}\right)^2\right) \exp\left(-\frac{1}{2}\left(\frac{x}{x_0}\right)^2\right) \tag{7.1}$$

where x is the dot product of the vector to the echo and the radiant vector and x_0 is the resolution (Figure 7.1) (Jones, 1993).

Echoes at 90° from the radiant are weighted close to 1, and those within the resolution have a positive weight. Echoes farther than the 15° resolution from perpendicular to the radiant are given a negative weight. Any source with a width greater than the resolution will be removed entirely, while any source with a smaller width

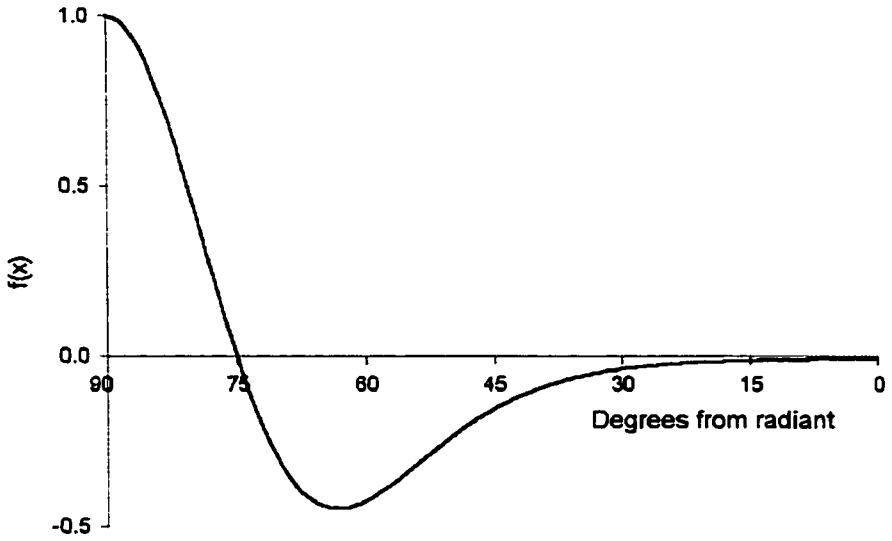

Figure 7.1: Weighting function applied to echoes at 15° resolution

will show strongly. Any uniform background will be removed from the sources, since the integrated area under the weighting function is zero.

Maps were constructed of shower activity to determine the number of echoes to be removed. The strongest showers were removed entirely on their peak day. For all showers, the number removed depended on how close to the peak the observations were taken: the width of each shower was found from examination of the data and the percent removed was scaled accordingly (Table 7.1).

The maps are in the form of Mollner-Weidener plots, which can be easily converted from right ascension and declination to chart coordinates and back. The plots of sporadic sources are in heliocentric coordinates with the sun at (0,0). The line of 0 latitude corresponds to the plane of the ecliptic, and the apex of the Earth's motion is at (0,270), in the center of the plot. The resolution of the plots is 15°. Showers show up very clearly on the peak days (Figure 7.4); when shower meteors are removed the background is much clearer (Figure 7.5).

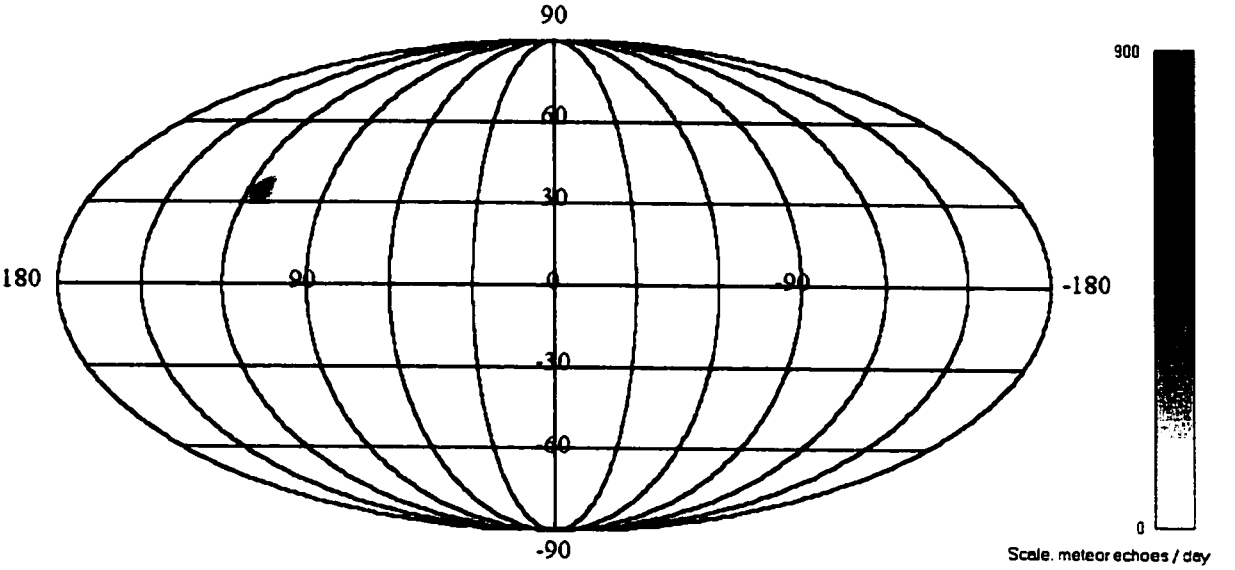

Figure 7.2: Celestial map of activity to 3° resolution December 13, 2000. Note the Geminid radiant at 113, +33

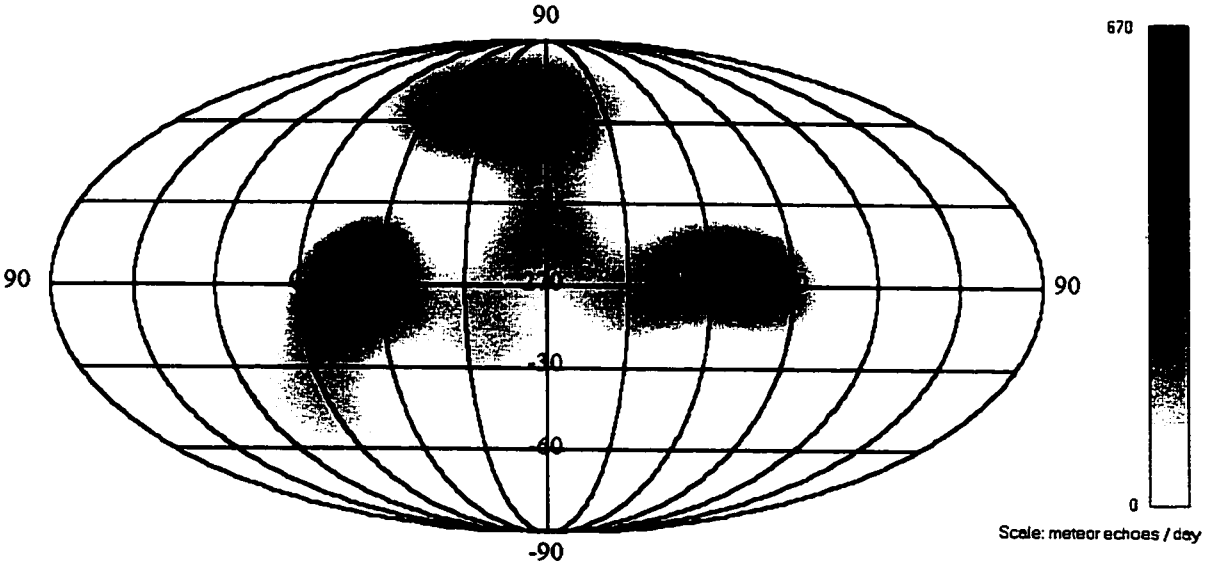

Figure 7.3: Heliocentric plot of activity to 15° resolution April 16, 2000: no significant shower activity.

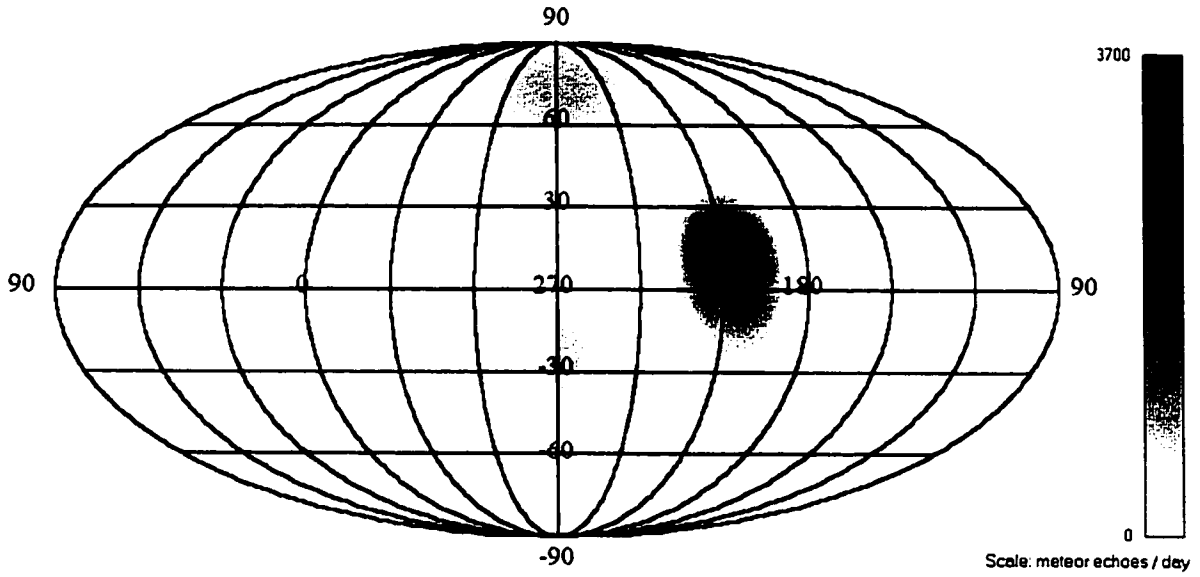

Figure 7.4: Heliocentric plot of activity to 15° resolution December 13, 2000.

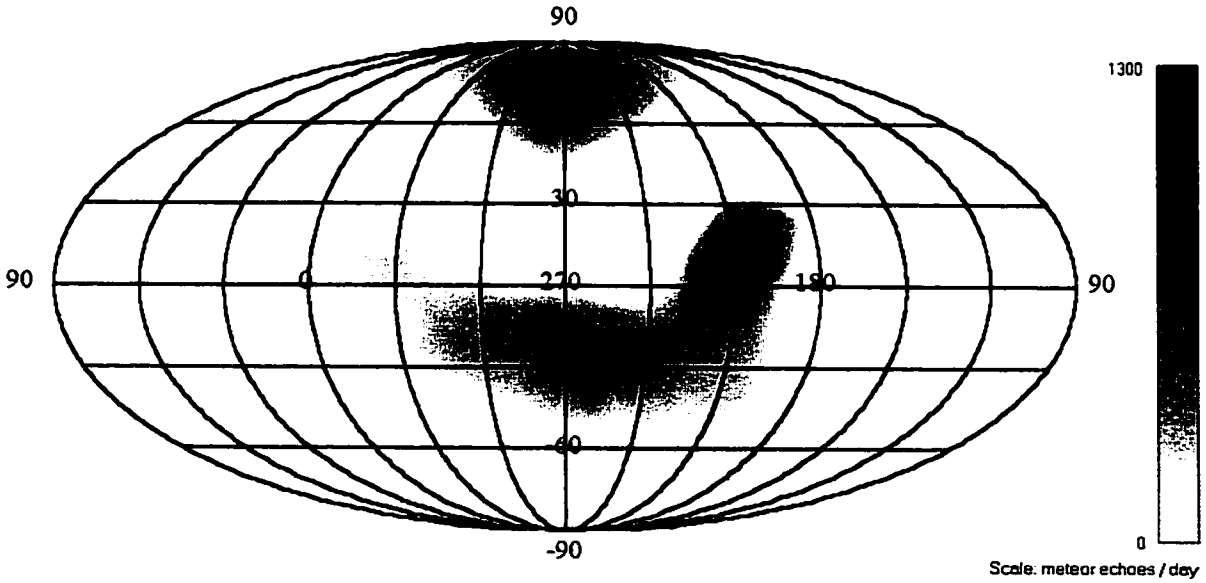

Figure 7.5: Heliocentric plot of activity to 15° resolution December 13, 2000, with Geminids removed.

7.2.2 Determining Rates of Sporadic Sources

Once the shower meteors have been removed, the number of meteors coming each day from each of the sporadic sources can be calculated. Before performing the analysis, we remove all echoes which are ambiguous and those with zenith angles larger than 70°, which will have large uncertainties in geometry.

7.3 Collecting Area of Radar

Dividing the rate of meteors by the collecting area will give the uncorrected flux. The collecting area of the radar is the physical area of sky over which meteors from a particular radiant can be seen: we add corrections to this to account for the difference in sensitivity over this area and for the elevation of the radiant.

If meteors occurred at only one height, echoes from a single radiant would occur on a plane normal to the radiant. Since meteors ablate at a range of heights, this is actually an echo strip. To find the area, one must calculate the width and useful length of this strip. We also add a scaling factor to account for variation in sensitivity of the radar over the area.

The width of the strip depends on the vertical distance dh covered by an average meteor. This quantity depends on the mass distribution index: a larger index will mean more small meteoroids, which will make the average trail length shorter. The value of dh can be found with optical observations of meteors: from Flemming *et al* (1993) we obtain dh as a function of s:

$$dh = \frac{7.88s^3 + 56.2s^2 - 164s + 105}{12.2(s-1)^3}. \tag{7.2}$$

The width w is then

$$w = dh \csc \chi \tag{7.3}$$

where χ is the zenith angle of the radiant (Figure 7.6).

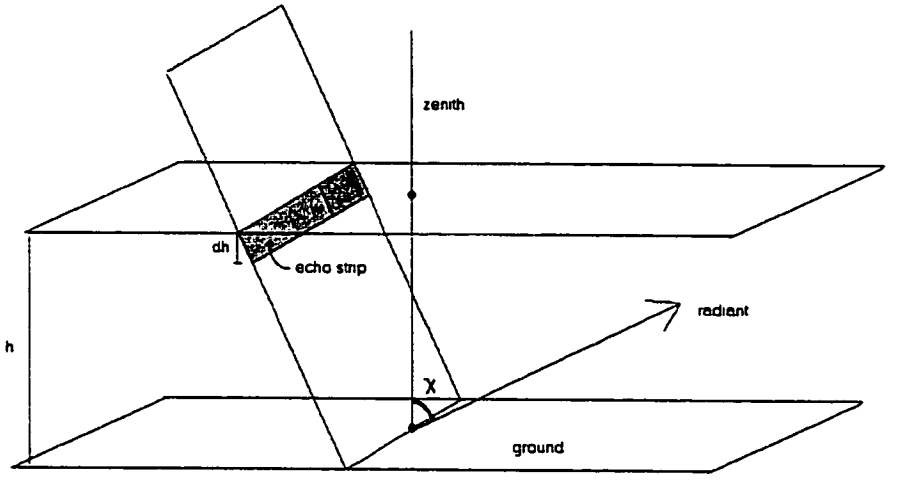

Figure 7.6: Segment of collecting area for a radiant

The length of the strip will extend in two directions from the minimum range out to a range of 300km: at larger ranges than this the zenith angle will be greater than 70° and the echoes are rejected from the analysis. The number of echoes which can be seen at a particular part of the echo strip depends on the limiting line density, q_{lim}:

$$N \propto {q_{lim}}^{1-s} \tag{7.4}$$

where we have used the mass distribution equation 5.5 and the fact that $q \propto m$. The minimum detectable amplitude is the same everywhere in the radar beam, but the limiting electron line density will vary as (from equation 2.16):

$$q_{lim} = \frac{A_{lim}}{sens} \tag{7.5}$$

where

$$sens = K \left(\frac{G_R G_T}{{R_0}^3} \right)^{3/2} \tag{7.6}$$

where K is a constant which depends on the transmitter power and system wavelength, but is constant over the radar beam.

The number of echoes visible depends on the sensitivity as:

$$N \propto sens^{s-1} \tag{7.7}$$

since the limiting electron line density is inversely proportional to the sensitivity.

To obtain a weighting factor, we divide the number of echoes visible at a given area by the number visible at the region of maximum sensitivity on the echo line:

$$F = \frac{N}{N_m} = \frac{sens^{s-1}}{sens_m{}^{s-1}} \tag{7.8}$$

where the subscript m refers to the quantity at maximum sensitivity. The weighting factor is therefore

$$F = \left[\left(\frac{G_R G_T}{R_0{}^3} \right)^{1/2} \left(\frac{R_{0m}{}^3}{G_{Rm} G_{Tm}} \right)^{1/2} \right]^{s-1} . \tag{7.9}$$

The weighted length of the echo strip is:

$$l = \int F dk, \tag{7.10}$$

where dk is a distance element along the echo surface.

There is one more correction to apply to the collecting area for the zenith angle of the radiant, χ. If the radiant is low, the meteors have a grazing incidence; they will have longer paths and therefore a lower electron line density. The number correction is as $(\sec \chi)^{s-1}$.

The weighted collecting area for a particular radiant is then:

$$\Phi = w \int F dk \, (\sec \chi)^{s-1} . \tag{7.11}$$

The collecting area can be integrated over a whole day to correct daily rates.

7.4 Other Correction Factors

The rate of meteors over one day, divided by the integrated collecting area over that day, gives us a preliminary flux of meteors per unit time and area. This flux must

Table 7.2: Source diffuseness correction factors

Source	Width (degrees)	Correction factor
Helion & Antihelion	17	0.638
North & South Apex	21	0.280
North & South Toroidal	17.5	0.577

be corrected for other observing factors, including the diffuseness of the radiant, the limiting sensitivity and the initial radius and fragmentation factor.

7.4.1 Diffuseness of source

Since the sporadic sources are not point radiants, the rate measured at the peak of the location of the sporadic source is not the true rate. To find the factor by which the measured rate was reduced, simulations of diffuse radiants were constructed for radiants of different widths. The rates measured for these simulated radiants were compared to the generated number of meteors.

The widths of each source were taken from Jones & Brown (1993). Two thousand meteors were generated from the appropriate heliocentric coordinates and the source strength measured in the same way as the observed data. Table 7.2 gives the results.

7.4.2 Initial radius

The correction factor for initial radius which we calculated is useful for radars with a limiting sensitivity of $+9^M$, and meteors with a velocity of 35km/s. We have obtained a correction for each of the sporadic sources by adjusting the height distribution according the mean velocity of the source. No attempt was made to correct for variations in initial raidus with velocity other than this.

The sensitivity of the radar depends on the transmitter power. We can obtain a more accurate correction by recalculating the coefficient if the power of the radar changes. This happened a number of times in 2000 and 2001 because of equipment failures. The correction factor can be altered according to equation 6.13.

7.4.3 Correction for limiting sensitivity

The flux we have calculated to this point is a real flux, to the limiting magnitude of the system. To compare it with other results, we wish to change it to the flux at a limiting magnitude of $+6.5^M$, corresponding to a limiting mass of 2.5×10^{-6} kg, or 2.5 mg.

When dealing with magnitudes, we use the population index r, which is related to the mass distribution index as (McKinley, 1961):

$$s = 1 + 2.5 \log r. \tag{7.12}$$

The number of meteors seen at a particular magnitude goes as

$$N_M = r^M \tag{7.13}$$

so the ratio of the number of meteors seen at a limiting magnitude of +6.5 to the number seen at another limiting magnitude is

$$\frac{N_{6.5}}{N_M} = r^{6.5-M}. \tag{7.14}$$

Putting this in terms of the mass distribution index, we have

$$N_{6.5} = N_M 10^{(6.5-M)(s-1)/2.5} \tag{7.15}$$

This gives the correction factor for flux observations at any magnitude M.

7.5 Results

The fluxes for each of the five sporadic sources was calculated for all available data in 1999, 2000 and 2001. The flux, in meteoroids $km^{-2}day^{-1}$, was calculated for every day for which data was taken, and is shown in Figures 7.7 through 7.11.

The helion and antihelion sources have a similar variation to that found by Poole (1997) (Figure 1.3). The antihelion source shows a maximum in the summer months.

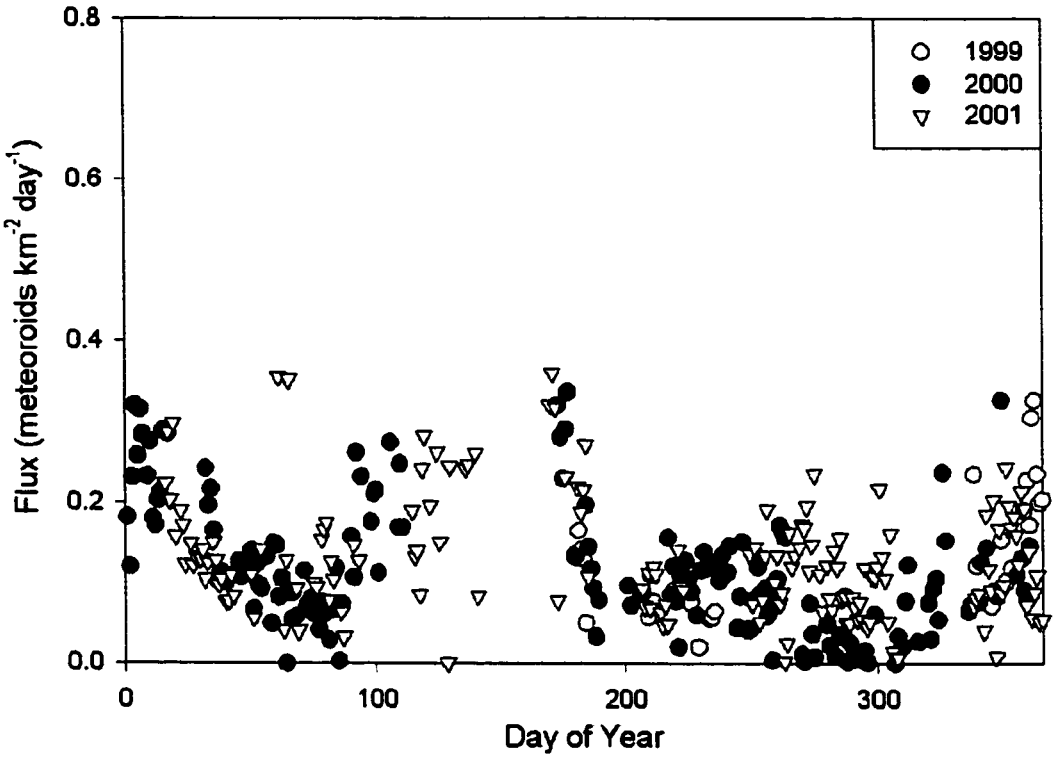

Figure 7.7: Helion flux at 29 MHz

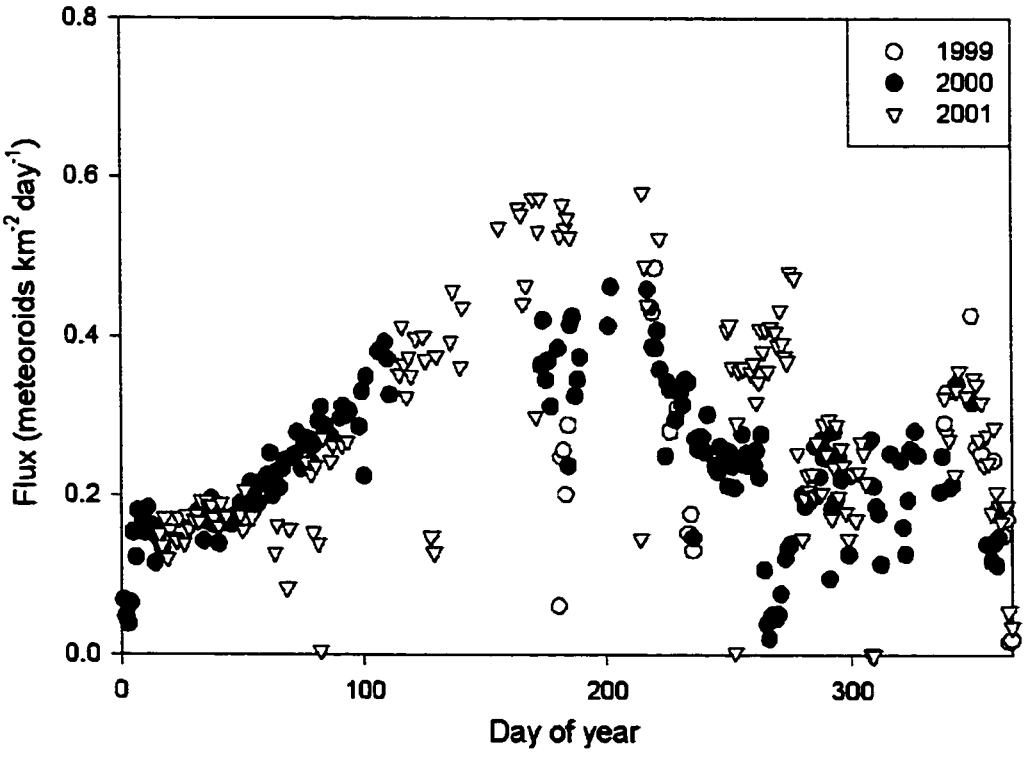

Figure 7.8: Antihelion flux at 29 MHz

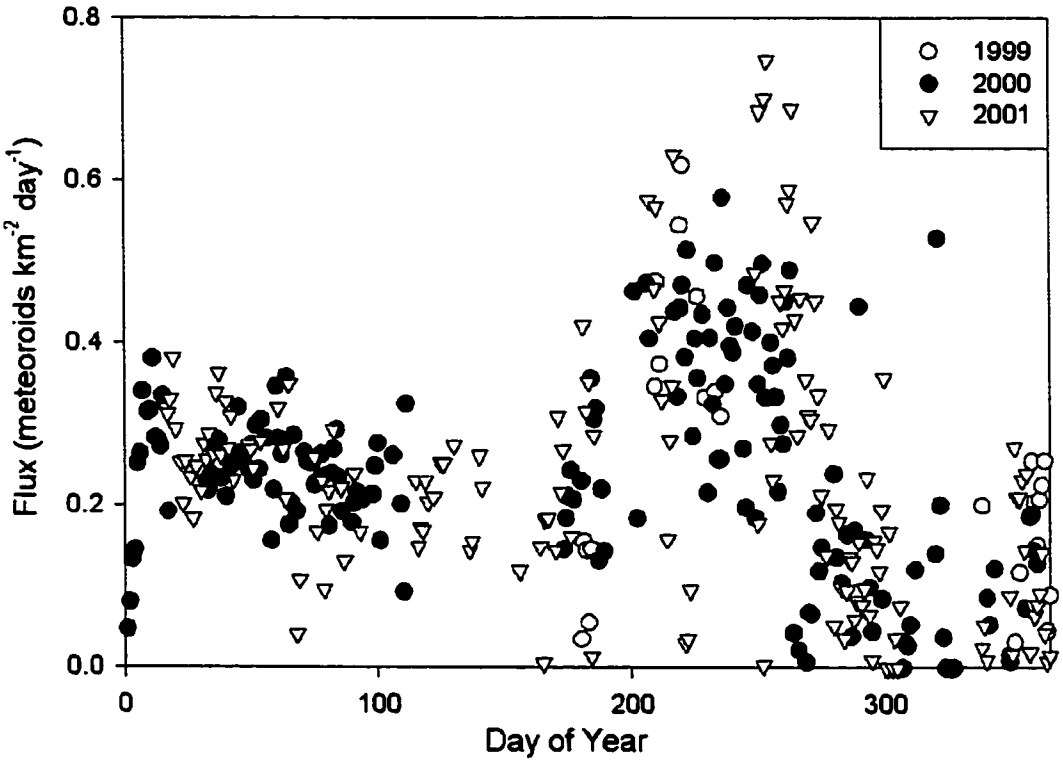

Figure 7.9: North apex flux at 29 MHz

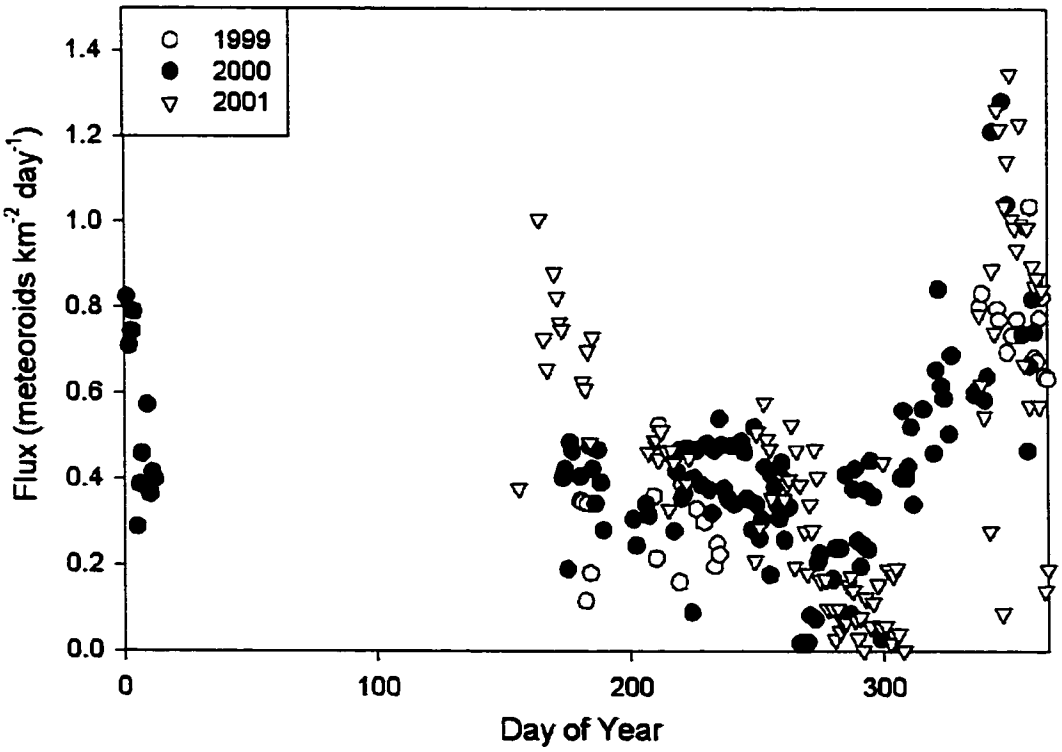

Figure 7.10: South apex flux at 29 MHz

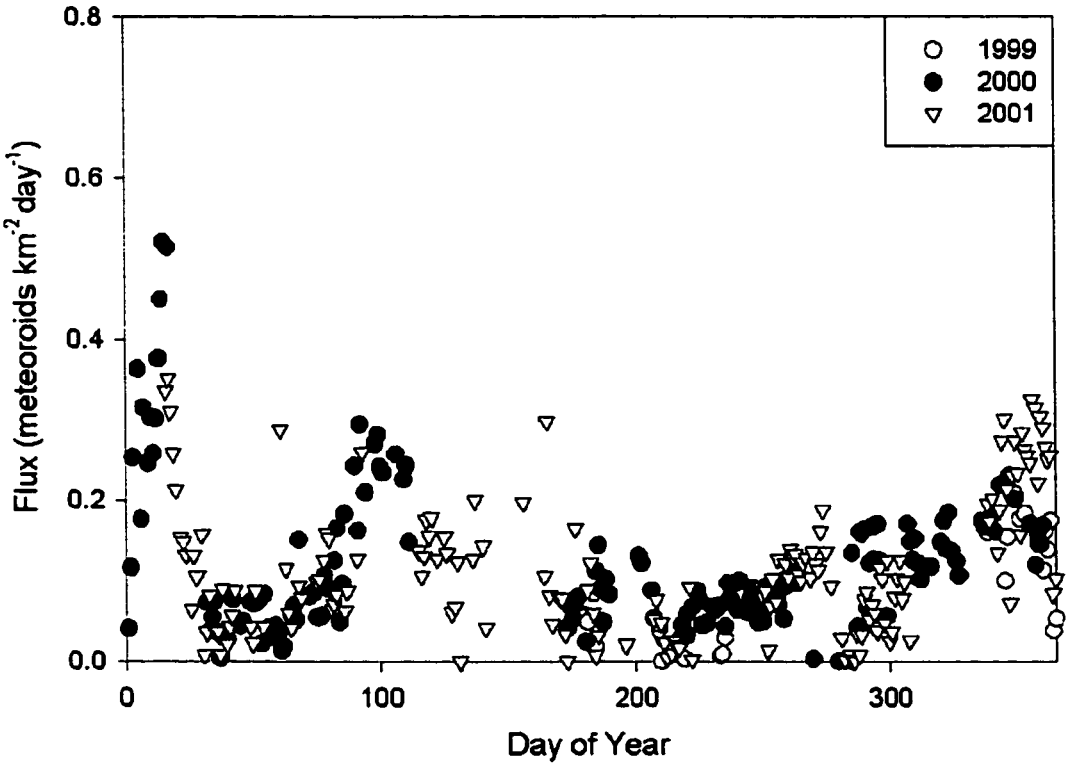

Figure 7.11: North toroidal flux at 29 MHz

The helion source variation is not as clear, but the data are consistent with a maximum in first four months of the year.

The north apex source does not appear to vary by a large amount throughout the year, though it is strongest in August and September and weakest in the last three months of the year. The south apex source is too low to be observed at the latitude of Tavistock for the first half of the year, so it is difficult to draw any conclusions about the variation of this source. Both apex sources have high fluxes compared to the helion and antihelion sources: this is in part due to the greater uncertainty because of the large correction factor. The south apex source also suffers from a small collecting area because of its low altitude: the error on the fluxes is even greater for this source.

The north toroidal source, in addition to showing a significant annual variation with a peak at the beginning of the year, shows a noticeable drop in the first few weeks of the year. This is not an equipment failure, since it occurs both in 2000 and

2001. The cause does not appear to be a matter of geometry, since both the elevation of the source and the gain pattern of the radar are accounted for in the calculation. There seems to be a real lack of Earth-intersecting orbits from the toroidal source in February.

The total flux from the five sources, averaged over the course of a year, is 0.97 $\pm$ 0.03 meteoroids $km^{-2}day^{-1}$ to a limiting mass of 2.5×10^{-6} kg for the year 2000, and 1.00 $\pm$ 0.04 meteoroids $km^{-2}day^{-1}$ to a limiting mass of 2.5×10^{-6} kg for the year 2001. This compares to the value of 0.21 meteoroids $km^{-2}day^{-1}$ to a limiting mass of 10^{-6} kg from combined results of spacecraft-borne dust detector measurements, radar and optical observations of meteors (Ceplecha *et al*, 1998; Grün *et al*, 1985). The fact that these results, even without refining the velocity effect, agree to within a factor of 5 with measurements independent of the initial radius factor is encouraging.

7.6 Discussion

7.6.1 Results of current study

The most significant result of this study of the initial radius effect is that it is fragmentation, and not the spread of electrons in a single trail, which is principally responsible for the attenuation observed on all radar systems. Previous correction factors based on the assumption that the initial radius of single trails is responsible for the attenuation are therefore inaccurate.

A model has been developed which explains the observations on the Tavistock three-frequency radar, both in terms of the magnitude of and scatter in amplitude ratios and in terms of the height distributions on all systems. This model is the best of all physically likely models. The model was developed with observation of Geminid meteors to avoid any effects of velocity, as a first approximation: it was shown that the model fits observations of sporadic meteors as well.

Equation 6.13 is currently the best estimate of the correction factor describing the fraction of meteors observable on radar systems of any wavelength and limiting

magnitude, for any velocity of meteoroid. Between 20 and 40% of the total number of meteors are visible on the 29 MHz system, depending on the velocity of the meteoroids being studied.

The derived correction factors were used to calculate the flux of meteoroids striking the Earth from each of the five sporadic sources visible in the Northern Hemisphere from observations with the Tavistock radar at 29 MHz. The total flux agrees with other studies to within a factor of five. Annual variations in the helion and antihelion sources agree with previous studies of change in activity.

7.6.2 Future work

The present study has presented a number of answers to longstanding problems in radar observations of meteors: it also suggests possibilities for future work in this area. The correction factor obtained here could be refined using a large number of observations of sporadic meteors for which accurate velocities have been measured and for which the source is unambiguous. This would allow the inclusion of velocity effects not taken into account in the current study and would improve the fit to each individual source. Other showers could also be observed and corrections could be calculated for them. Obtaining even larger numbers of echoes on 17 MHz would allow these data to be included in a refined model, which would raise the observable height range and would give a more accurate measure of how the radius of fragmentation changes with height. From such observations it might be possible to gain a more accurate measure of the rate at which the meteor fragments spread, which would lead to insights to their structure.

High resolution studies of meteors, some of which are currently under way (Hawkes, 2002), may provide an accurate measure of the width of the luminous portion of the meteor trail, which could be compared to the width deduced here. High resolution light curve studies might also provide more evidence as to the nature of the fragments.

The annual variation of the sporadic sources suggests anisotropies in the distribution of orbits around the Earth's orbit. Modelling could be done of the sporadic background and some measure of the number of parent comets required to produce

the observed irregularities could be obtained. Southern Hemisphere observations of the south toroidal source would be particularly interesting, to see if that source shows the same distinct change in strength over the course of a year as the north toroidal source. The measures of the annual variations of Northern Hemisphere sources will be improved with the new power monitoring system recently installed on the radar systems: continuous tracking of the transmitter power will make daily flux measurements more accurate.

Bibliography

Baggaley W. J. (1970) "The determination of the initial radii of meteor trains". *Monthly Notices Roy. Astron. Soc.* **147**, 231–243.

Baggaley W. J. (1980) "Measurements of the velocity dependence of the initial radii of meteor trains". *Bull. Astron. Inst. Czech.* **31**, 308–311.

Baggaley W. J. (1981) "Single wavelength measurements of the initial radii of radio meteor ionization columns". *Bull. Astron. Inst. Czech.* **32**, 345–349.

Baggaley W. J. and G. W. Fisher (1980) "Measurements of the initial radii of the ionization columns of bright meteors". *Planet. Space Sci.* **28**, 575–580.

Bayrachenko I. V. (1963) "Measurement of the initial radii of ionized meteor trails from simultaneous observation of radio meteors on two wavelengths". *Geomagn. & Aeron.* **5**, 353–356.

Beech, M. and P. G. Brown. (2000) "Fireball flickering: the case for indirect measurement of meteoroid rotation rates". *Planet. Space Sci.* **48**, 925–932.

Bilitza, D. "International Reference Ionosphere 2000", *Radio Science* **36**, 261–275.

Bronshten V. A., 1983, *The Physics of Meteoritic Phenomena.* Reidel, Dordrecht.

Brown, P and J. Jones. (1995) "A determination of the strengths of sporadic meteor sources". *Earth, Moon, Planets* **62**, 62–68.

Brown, P., W. K. Hocking, J. Jones and J. Rendtel. (1998) "Observations of the Geminids and Quadrantids using a stratosphere-troposphere radar". *Monthly Notices Roy. Astron. Soc.* **295**, 847–859.

Campbell, M. D., R. L. Hawkes, D. D. Babcock. (1998) "Light curves of shower meteors: implications for physical structure". *Meteoroids 1998* 363–366.

Campbell, M. D., P. G. Brown, A. G. LeBlanc, R. L. Hawkes, J. Jones, S. P. Worden, R. R. Correl. (2000) "Image-intensified video results from the 1998 Leonid shower: I. Atmospheric trajectories and physical structure". *Meteorit. & Planetary Sci.* **35**, 1259–1267.

Ceplecha, Z., J. Borovička, W. G. Elford, D. O. Revelle, R. L. Hawkes, V. Porubčan, and M. Šimek. (1998) "Meteor Phenomena and bodies". *Space Sci. Rev.*, **84**, 327–471.

Cook, A. F., Hawkins, G. S. and F. M. Stienon. (1962) "Meteor trail widths". *Astron. J.*, **67**, 158–291.

Davies, J. G. and J. C. Gill. (1960) "Radio echo measurements of the orbits of faint sporadic meteors". *Monthly Notices Roy. Astron. Soc.* **121**, 437–462.

Delov, I. A. (1976) "Method for determining the diffusion coefficient and the initial radius from overdense meteor trails". *Geomagn. & Aeron.*, **15**, 774–775.

Denning, W. F. (1886) "Distribution of meteor streams". *Monthly Notices Roy. Astron. Soc.*, **47**, 35–39.

Dokuchaev, V. P. (1960) "Formation of an ionized meteor trail". *Sov. Astron.* **4**, 106–109.

Dyrud, L., M. Oppenheim, S. Close, S. Hunt, A. vom Endt and K. McMillon. (2002, in press) "Meteor trail evolution: Comparison between ALTAIR radar observations and plasma simulations". *Meteoroids 2001.*

Elford, W. G. and G. S. Hawkins. (1964) "Meteor echo rates and the flux of sporadic meteors". *Smithsonian. Astrophys. Observatory research report no. 9.*

Elford, W. G. and D. I. Steel. (1988) "The height distribution of radio meteors — Observations at 6 MHz". *J. Atmospheric Terrest. Phys.*, **50**, 811–818.

Elford, W. G. and A. D. Taylor. (1997) "Measurement of Faraday rotation of radar meteor echoes for the modelling of electron densities in the lower ionosphere". *J. Atmospheric Terrest. Phys.*, **59**, 1021–1024.

Fisher, A. A., R. L. Hawkes, I. S. Murray, M. D. Campbell and A. G. LeBlanc. (2000) "Are meteoroids really dustballs?". *Planet. Space Sci.* **48**, 911–920.

Flemming, D. E. B., R. L. Hawkes, and J. Jones. (1993) "Light curves of faint television meteors". *Meteoroids and their Parent Bodies*, eds. J. Štohl and I. P. Williams, 261.

Greenhow J. S., and J. E. Hall (1960) "The importance of initial trail radius on the apparent height and number distributions of meteor echoes". *Monthly Notices Roy. Astron. Soc.* **121**, 183–196.

Grün, E., H. A. Fechtig, and R. H. Giese. (1985) "Collisional Balance of the meteoric complex". *Icarus*, **62**, 244–272.

Grusha, G. V. (1991) "Modeling the formation of the initial radius of a meteor trail". *Solar Sys. Rev.* **25**, 58–62.

Hawkes, R. L. (1993) *Meteoroids and their Parent Bodies*, eds. J. Štohl and I. P. Williams, 227.

Hawkes, R. L. (2002, in press) "High resolution meteor light curve investigations". *Meteoroids 2001.*

Hawkes R. L., and J. Jones. (1975) "A quantitative model for the ablation of dustball meteors". *Monthly Notices Roy. Astron. Soc.* **173**, 339–356.

Hawkes R. L., and J. Jones. (1978) "The effect of rotation on the initial radius of meteor trains". *Monthly Notices Roy. Astron. Soc.* **185**, 727–734.

Hawkes, R. L. and J. Jones. (1980) "Two station television meteor studies". *Solid Particles in the Solar System; I. Halliday and B. A. McIntosh (eds.)* 117–120.

Hawkins, G. S. (1956) "A radio echo survey of sporadic meteor radiants". *Monthly Notices Roy. Astron. Soc.* **116**, 92–104.

Hawkins, G. S. (1956) "Variation in the occurrence rate of meteors". *Astron. J.* **61**, 386–391.

Hawkins, G. S. (1963) "The initial diameter of meteor trails". *Smithsonian Contr. Astrophys.* **7**, 23–26.

Hawkins, G. S. and J. P. M. Prentice. (1957) "Visual determination of the radiant distribution of sporadic meteors". *Astron. J.* **62**, 234–240.

Hawkins, G. S. and F. L. Whipple. (1958) "The width of meteor trails". *Astron. J.* **63**, 283–291.

Hocking, W. K., B. Fuller and B. Vandepeer. (2001) "Real-time determination of meteor-related parameters utilizing modern digital technology". *J. Atmospheric Sol. Terrest. Phys.* **63**, 155–169.

Hocking, W. K., T. Thayaparan and J. Jones. (1997) "Meteor decay times and their use in determining a diagnostic mesospheric temperature-pressure parameter: Methodology and 1 year of data". *Geophys. Res. Let.* **24**, 2977.

Hoffmeister, C. (1929) "On the heliocentric velocity of meteors". *Astrophys. J.* **69**, 159–167.

Hoffmeister, C. (1948) *Meteörstrome* Verlag Werden und Werken Weimar, Leipzig.

Hughes, D. W. (1978) "Meteors". In *Cosmic Dust*, Wiley-Interscience, 123–185.

Jacchia, L. G. (1955) "The physical theory of meteors: VIII Fragmentation as cause of the faint-meteor anomaly". *Astrophys. J.* **121**, 521–527.

Jacchia, L. G., F. Verniani and R. E. Briggs. (1965) "An analysis of the atmospheric trajectories of 413 precisely reduced photographic meteors". Smithsonian Astrophysical Observatory Special Report 175.

Jones, J. (1977) "Meteor radiant distribution using spherical harmonic analysis". *Bull. Astron. Inst. Czech.*, **28**, 272–277.

Jones, J. (1983) "Radar observations of the Orionid meteor shower". *Monthly Notices Roy. Astron. Soc.*, **204**, 765–776.

Jones, J. (1993) Presented at Asteroids, Comets and Meteors 1993. Abstract published in proceedings.

Jones, J. and J. D. Morton. (1977) "The determination of meteor stream radiants from single station observations". *Bull. Astron. Inst. Czech.*, **28**, 267–272.

Jones, J. and P. Brown. (1993) "Sporadic meteor radiant distributions: orbital survey results". *Monthly Notices Roy. Astron. Soc.*, **265**, 524–532.

Jones, J., P. Brown, A. R. Webster and K. Ellis. (1994) "A forward-scatter determination of the radiant distribution of sporadic meteors". *Planet. Space Sci.* **42**, 127–134.

Jones, J., A. R. Webster and W. K. Hocking. (1998) "An improved interferometer design for use with meteor radars". *Radio Sci.*, **33**, 55–65.

Jones, W. (1991) "Theory of diffusion of meteor trains in the geomagnetic field". *Planet. Space Sci.* **39**, 1283–1288.

Jones W. (1995) "Theory of the initial radius of meteor trains". *Monthly Notices Roy. Astron. Soc.* **275**, 812–818.

Jones, W. (1997) "Theoretical and observational determinations of the ionization coefficient of meteors". *Monthly Notices Roy. Astron. Soc.*, **288**, 995–1003.

Jones, W. and J. Jones. (1990) "Ionic diffusion in meteor trains". *J. Atmospheric Terrest. Phys.* **52**, 185–191.

Kaiser, T. R. (1961) "The determination of the incident flux of radio-meteors: II. Sporadic meteors". *Monthly Notices Roy. Astron. Soc.* **123**, 265–271.

Kaiser, T. R. (1968) "Diffusion of meteor trains in the geomagnetic field". *IAU Symposium* **33**, 161–168.

Kaiser, T. R., W. M. Pickering and C. D. Watkins. (1969) "Ambipolar diffusion and motion of ion clouds in the earth's magnetic field". *Planet. Space Sci.* **17**, 519–552.

Kashcheyev, B.L. and V. N. Lebedinets. (1963) "The initial radius of ionized meteor trails". *Smithsonian Contr. Astrophys.* **7**, 19–22.

Keay, C. S. L., (1963) "The distribution of meteors around the Earth's orbit". *J. Atmospheric Terrest. Phys.*, **25**, 507.

Lindblad, B. (1956) "Combined visual and radar observations of Perseid meteors". *Medd. från Lunds Astron. Obs., no 189.*

Lovell, A. C. B. (1954) *Meteor Astronomy.* Clarendon Press, Oxford.

Manning L. A., (1958) "The Initial Radius of Meteoric Ionisation Trails." *J. Geophys. Res.* **63**, 181–196.

Massey, H. S. W. and D. W. Sida. (1955) "Collision processes in meteor trains". *Phil. Mag.*, **46**, 190–198.

McCrosky, R. E. (1955) "Fragmentation of faint meteors". *Astron. J.* **60**, 170.

McCrosky, R. E. (1958) "The meteor wake". *Astron. J.* **63**, 97–106.

McKinley D. W. R. (1961) *Meteor Science and Engineering.* McGraw-Hill.

Millman, P.M. and D. W. R. McKinley. (1956) "Meteor echo durations and visual magnitudes". *Canad. J. Phys.*, **34**, 50–61.

Morton, J. D. and J. Jones. (1982) "A method for imaging radio meteor radiant distributions". *Monthly Notices Roy. Astron. Soc.*, **198**, 737–746.

Moysya, R. I. (1969) "Statistical characteristics of the initial radii of ionized meteor trails". *Geomagn. & Aeron.* **9**, 95–99.

Murray I. S., M. Beech, M. J. Taylor, P. Jenniskens, R. L. Hawkes. (2000) "Evidence for transverse spread in Leonid meteors". *Earth, Moon, Planets* **82–83**, 351–367.

Olivier, C. P. (1925) *Meteors.* Williams and Wilkins Company, Baltimore.

Olsson-Steel, D. I. and W. G. Elford. (1986) "Are there many more small meteors than hitherto detected?" *Proc. Astron. Soc. Aust.*, **6**, 436–439.

Olsson-Steel, D. I. and W. G. Elford. (1987) "The height distribution of radio meteors — Observations at 2 MHz". *J. Atmospheric Terrest. Phys.* **49**, 243–258.

Öpik, E. J. (1958) *Physics of Meteor Flight in the Atmosphere.* Interscience Publishers Inc.

Oppenheim, M. M., A. F. vom Endt and L. P. Dyrud. (2000) "Electrodynamics of meteor trail evolution in the equatorial E-region ionosphere". *Geophys. Res. Let.* **27**, 3173–3176.

Paddack, S. J. (1969) "Rotational bursting of small celestial bodies: Effects of radiation pressure". *J. Geophys. Res.*, **74**, 4379–4381.

Peregudov, F. I. (1958) "On the effect of meteor velocities on the hour number in radio-echo detection of meteors". *Sov. Astron*, **2**, 833–838.

Pickering, W. M. and D. W. Windle. (1970) "The diffusion of meteor trains". *Planet. Space Sci.* **18**, 1153–1161.

Poole, L. M. G. (1997) "The structure and variability of the helion and antihelion sporadic meteor sources". *Monthly Notices Roy. Astron. Soc.*, **290**, 245–259.

Portnyagin, Yu. I. and V. S. Tokhtas'yev. (1974) "Effective diffusion cross section of meteor atoms and ions in the atmosphere for an extended region of interaction energies". *Geomagn. & Aeron.* **14**, 67–71.

Press, W. H., S. A. Teukolsky, W. T. Vetterling and B. P. Flannery. (1992) *Numerical Recipes in C, 2nd ed.* Cambridge University Press.

Sekanina, Z. (1976) "Statistical Model of Meteor Streams. IV: A study of radio streams from the synoptic year". *Icarus* **27**, 265–321.

Steel, D. I. and W. G. Elford. (1991) "The height distribution of radio meteors — Comparison of observations at different frequencies on the basis of standard echo theory". *J. Atmospheric Terrest. Phys.* **53**, 409–417.

Štohl, J. (1967) "On two problems of sporadic meteor activity". *Smithsonian Contr. Astrophys.*, **11**, 115–117.

Štohl, J. (1968) "Seasonal variation in the radiant distribution of meteors" *IAU Symp.* **33** Physics and Dynamics of Meteors. 298–303.

Thomas, R. M., P. S. Whitham and W. G. Elford. (1986) "Frequency Dependence of Radar Meteor Echo Rates". *Proc. Astron. Soc. Aust.*, **6**, 303–306.

Triskova, L. (1968) "A note on the sporadic meteor radiant distribution". *IAU Symp.* **33** Physics and Dynamics of Meteors. 304–307.

Weiss, A. A. and J. W. Smith. (1960) "A southern hemisphere survey of the radiants of sporadic meteors". *Monthly Notices Roy. Astron. Soc.* **121**, 5–16.

Whipple, F. L. (1963) "Meteoritic Erosion in Space". *Smithsonian Contr. Astrophys.*, **7**, 239–248.